

LINKS BETWEEN MICROSTRUCTURE, EROSION, AND ELECTRON
EMISSION BEHAVIOR IN POLYCRYSTALLINE
BORON-BASED MATERIALS

by

THOMAS SCOTT BURTON

GREGORY B. THOMPSON, COMMITTEE CHAIR
RICHARD BRANAM
ROBIN D. FOLEY
W. JUD READY
JULIAN J. RIMOLI
MITCHELL L. R. WALKER
MARK L. WEAVER

A DISSERTATION

Submitted in partial fulfillment of the requirements
for the degree of Doctor of Philosophy
in the Department of Metallurgical and Materials Engineering
in the Graduate School of
The University of Alabama

TUSCALOOSA, ALABAMA

2016

Copyright Thomas Burton 2016
ALL RIGHTS RESERVED

ABSTRACT

Hall effect thrusters (HETs) are an important technology underpinning the effort to develop high impulse electric propulsion devices. The research here has addressed boron based materials that are used in these devices – namely the protective chamber wall for protecting the magnetic circuit components and the cathode that injects electrons into the plasma.

The microstructural features of a post-operated chamber wall were examined and found to have three characteristic erosion features after extended plasma exposure. Conical protrusions are believed to be a result of sputter erosion whereas micro-cracking and loss of BN grains is contributed to residuals stresses created by anisotropic thermal expansion of BN within the composite ceramic.

To study the effect of these topological features, particularly the protrusions, had on secondary electron emission; a series of mechanical attrition features on the length scale of microns were created in an analogue graphite material. It was found that there was an overall reduction in emission from smooth to roughened surfaces; however, a rougher surface does not necessarily yield the lowest emission. A characteristic length scale was observed where surface feature size relative to roughness appears to regulate the emission.

In addition, a series of large scale topology grooves (on the order of millimeters) were created to simulate larger length erosion features noted in extended plasma exposed materials. The effect of these features on the plasma sheath floating wall potential was measured for a BN surface. As the grooves depth increased, the floating wall potential necessary to collapse the plasma sheath

increased. A detailed plasma simulation revealed that trapping of electrons occurs near the entrance of the grooves which was used to explain the plasma sheath phenomenon.

Finally, lanthanum hexaboride (LaB_6), was fabricated as a coating using vacuum plasma spraying to determine its feasibility as a replacement for bulk cathode configurations. Excess boron was added to LaB_6 powders prior to spraying and was found to improve the densification of the coating. However, the work function of these coatings was near ~ 4.3 eV, this is higher than other processes and is contributed to the incorporation of impurities in the coating.

DEDICATION

This dissertation is dedicated to my grandparents Bill and Marie Campbell, and Chuck and Mary-Ester Burton. If not for the appreciation of hard work and academics they instilled in my parents and their financial support, I simply would not have made it this far.

LIST OF ABBREVIATIONS AND SYMBOLS

2θ	Two Theta
AR	Aspect Ratio
$AX05$	Grade of 99.9% pure boron nitride
B	Boron
BSE	Back-Scattered Electrons
BN	Boron Nitride
E_0	Primary Electron Incident Energy
EDM	Electro Discharge Machining
EDS	Energy Dispersive x-ray Spectroscopy
E_F	Fermi Energy Level
E_L	Photon Energy of Lamp Source
E_{SE}	Energy of the Onset of Secondary Emission
eV	Electron Volts
GR	Groove Ratio
hBN	Hexagon Boron Nitride
HE	High Erosion
HET	Hall Effect Thruster
i_n	Current of Re-Collected Electrons
i_p	Current of Primary Beam Electrons

i_{SE}	Current of Secondary Electrons
i_B	Current of Primary Electrons
k_α	K-Alpha
L	Length Scale of the System
LaB_6	Lanthanum Hexaboride
LE	Low Erosion
$M26$	Composite Ceramic of 40wt.% Silica & 60wt.% BN
m_e	Mass of Electron
ME	Mild Erosion
N	Number of Points in the Image
n_B	Number of Incident Electrons
N_d	Number of Particles in a Debye Sphere
n_e	Electron Number Density
n_i	Ion Number Density
n_n	Neutral Number Density
n_p	Overall Number Density of the Plasma
n_{SE}	Number of Secondary Electrons
$PEEM$	Photo Emission Electron Microscopy
PVB	Polyvinyl Butyral resin
q_α	Charge of Plasma Particle Species
RMS	Root Mean Square
S_α	Average Surface Roughness
SE	Secondary Electrons

<i>SEM</i>	Scanning Electron Microscopy
<i>SEY</i>	Secondary Electron Yield
<i>SiC</i>	Silicon Carbide
S_q	Root Mean Square Roughness
<i>(S)TEM</i>	(Scanning) Transmission Electron Microscopy
T_e	Electron Temperature
<i>UPS</i>	Ultraviolet Photoelectron Spectroscopy
<i>VPS</i>	Vacuum Plasma Spray
<i>XPS</i>	X-ray Photo Spectroscopy
<i>XRD</i>	X-Ray Diffraction
Z	Atomic Number
Z	Feature Height
Z_{avg}	Average Height of Feature
Z_i	Height of Individual Feature
α	Temperature of Plasma Particle Species
δ	Secondary Electron Yield Coefficient
ϵ_0	Permittivity of Free Space
κ_B	Boltzmann Constant
λ_d	Debye Length
ν_c	Gaseous Collisional Timescale
Φ	Work Function
ω_{pe}	Electron Plasma Frequency

ACKNOWLEDGEMENTS

There are far more people to thank than there is space for this section, as nearly everyone who has crossed my path has offered either words of support or whatever assistance they could provide. My years here at The University of Alabama have often been stressful, filled with failed experiments and nonsensical ideas that left me confused and depressed. Many times my research seemed like it would never bear fruit, leaving me feeling like I failed all those who had supported me. But in the end I was successful, science and discovery is a long and winding road, never as clean or easy as we hope it will be.

My family has always been a constant pillar of support throughout my career; their encouragement in the form of texts, calls, and presents kept my spirits up and reminded me why I am here. My parents, Tom and Alison Burton, insisted that we video chat once a week and that I take time out to collect my thoughts. They would pepper in tough questions on what I wanted from my career, side-by-side with the latest gossip and pictures from my extended family, always keeping me hopeful and aware of the world outside my work. My sisters, Sarah and Amy, would send me pictures of my little nieces and forgive my missing of birthdays and holidays. My girlfriend, Sara Steele, listened to my constant frustrations and promised that I would one day be done; I did not always believe her, but I am glad that I did eventually. I certainly wouldn't have made it this far without those closest to me, and for that I am eternally gratefully.

My advisor Dr. Gregory Thompson is the one who made my graduate work possible in the first place. I am not sure what he saw in me, an inexperienced senior in materials engineering

working check-in at a small conference. On recommendation of a friend and current student he took me under his wing, and stood by me during the successes and the failures. His focus was always on working hard and his cheerful attitude kept my spirits up even when results were not forthcoming. I am very thankful you decided to trust in me all those years ago.

I'd like to thank all the other graduate students and post-docs who made my time here so much more pleasant with their comradery, misery made for great company: Chase Smith, Nick de Leon, Suzanne Kornegay, Brett Hunter, Todd Butler, Katherine Vinson, Tyler Kaub, Florian Vogel, Xuyang Zhou, Qianying Guo, Dallin Barton, Monica Kapoor, Jelani Hardwick, Anne Coppa, Li Wan, Justin Brons, Bradford Schulz, Chad Hornbuckle, and Billie Wang. To the CAF staff, who made sure all of the equipment was up and running as often as possible, and put up with our constant parade of needs and complaints: Rob Holler, Johnny Goodwin, and Rich Martens. Lastly, thank you to Jan Creitz, Kim Walker, and Susan Noble for their friendship and patience.

There were many technical professionals and other researchers whose experience and knowledge I have relied heavily upon during my graduate career. Over many conference calls, conversations, meetings, and visits to each other's laboratories the ideas and details behind our joint research was built upon. If not for their continual support my research would not have been nearly as complete or comprehensive: Dr. Mark Weaver, Dr. Luke Brewer, and Dr. Mark Barkey of The University of Alabama; Dr. Daniel Butts of Plasma Processes LLC; Dr. Alan Joly of the Pacific Northwest National Laboratory; Dr. Steven Fairchild and Dr. Tyson Back of the Air Force Research Laboratory; Dr. Mitchell Walker, Dr. Julian Rimoli, Dr. Jud Ready, Dr. Samuel Langendorf, and Dr. Aaron Schinder of The Georgia Institute of Technology; Dr. Michael Keidar and Dr. Irina Schweigert of The George Washington University. In addition, each member of my

dissertation committee, many of them listed above as well as Dr. Robin Foley and Dr. Richard Branam, for their time and patience in bringing my graduate research to a professional conclusion.

Finally without the financial support of the Air Force Office for Scientific Research (AFOSR) under grant FA9550-11-1-0160, my research would never have happened in the first place. I appreciate their support of this research effort.

CONTENTS

ABSTRACT.....	ii
DEDICATION.....	iv
LIST OF ABBREVIATIONS AND SYMBOLS.....	v
ACKNOWLEDGEMENTS.....	viii
LIST OF TABLES.....	xv
LIST OF FIGURES.....	xvi
STRUCTURE OF DISSERTATION.....	1
CONTRIBUTION TO RESEARCH.....	3
CHAPTER 1 INTRODUCTION.....	4
1.1 – BACKGROUND AND MOTIVATION.....	4
1.2 – CHAMBER WALL MATERIALS AND EROSION MECHANISMS.....	8
1.3 – PLASMAS AND THEIR PROPERTIES.....	13
1.4 – PLASMA SHEATH PHYSICS.....	16
1.5 – ELECTRON EMISSION IN MATERIALS.....	19
1.6 – LANTHANUM HEXABORIDE PROCESSING FOR CATHODE APPLICATIONS.....	21
1.7 – SUMMARY.....	23
1.8 – REFERENCES.....	24
CHAPTER 2 EXPERIMENTAL METHODS.....	29

2.1 – MATERIAL ACQUISITIONS AND INTENT.....	29
2.2 – METALLOGRAPHIC PREPARATION AND HANDLING OF MATERIALS....	30
2.3 – MICROSTRUCTURAL AND CHEMICAL CHARACTERIZATION.....	32
2.4 – PLASMA SHEATH MEASUREMENTS.....	33
2.5 – SECONDARY ELECTRON EMISSION MEASUREMENTS.....	33
2.6 – ULTRAVIOLET PHOTOELECTRON SPECTROSCOPY.....	35
2.7 – VACUUM PLASMA SPRAYING PARAMETERS.....	35
2.8 – OPTICAL PROFILOMETRY.....	36
2.9 – REFERENCES.....	37
CHAPTER 3 PLASMA INDUCED EROSION ON CERAMIC WALL STRUCTURES IN HALL EFFECT THRUSTERS.....	38
3.1 – ABSTRACT.....	38
3.2 – INTRODUCTION.....	38
3.3 – EXPERIMENTAL SETUP.....	41
3.4 – RESULTS.....	42
3.5 – DISCUSSION.....	47
3.6 – CONCLUSIONS.....	53
3.7 – REFERENCES.....	55
CHAPTER 4 INFLUENCE OF SURFACE ROUGHNESS ON ELECTRON EMISSION FROM GRAPHITE AND A GRAPHITE-COATED HALL EFFECT THRUSTER CHAMBER WALL.....	58
4.1 – ABSTRACT.....	58
4.2 – INTRODUCTION.....	59
4.3 – EXPERIMENTAL SETUP.....	64
4.4 – RESULTS AND DISCUSSION.....	66

4.4.1 – GRAPHITE SAMPLES AND TOPOLOGY DRIVEN REDUCTION IN EMISSION.....	66
4.4.2 – ANALYSIS OF GRAPHITE COATED HET WALL SAMPLES.....	72
4.5 – CONCLUSIONS.....	75
4.6 – REFERENCES.....	76
CHAPTER 5 EFFECT OF DEBYE-SCALE SURFACE FEATURES ON SPACE CHARGE SATURATION OF PLASMA SHEATHS.....	80
5.1 – ABSTRACT.....	80
5.2 – INTRODUCTION.....	81
5.3 – EXPERIMENTAL SETUP.....	83
5.3.1 – PLASMA DEVICE.....	83
5.3.2 –WALL MATERIAL SAMPLES.....	85
5.3.3 – DIAGNOSTICS.....	85
5.3.4 – COMPUTATIONAL METHODS.....	86
5.3.5 – OPTICAL MODEL FOR SECONDARY ELECTRON TRAPPING.....	86
5.3.6 – KINETIC MODEL FOR APPROXIMATIONS OF REDUCED SEE	89
5.4 – RESULTS AND DISCUSSION.....	91
5.5 – CONCLUSIONS.....	95
5.6 – REFERENCES.....	96
CHAPTER 6 INFLUENCE OF BORON ADDITIONS TO LAB₆'S WORK FUNCTION AND MICROSTRUCTURE IN VACUUM PLASMA SPRAYED COATINGS.....	99
6.1 – ABSTRACT.....	99
6.2 – INTRODUCTION.....	99
6.3 – EXPERIMENTAL SETUP.....	101
6.4 – RESULTS AND DISCUSSION.....	103

6.5 – CONCLUSIONS.....	109
6.6 – REFERENCES.....	110
CHAPTER 7 CONCLUSIONS AND FUTURE WORK.....	114
7.1 – EXTENDED PLASMA EROSION OF A M26 HET CHAMBER WALL.....	114
7.2 – INFLUENCE OF ROUGHNESS ON SEY FROM GRAPHITE SURFACE TOPOLOGIES.....	115
7.3 – INFLUENCE OF MILLIMETER SCALE GROOVES ON PLASMA SHEATH COLLAPSE VOLTAGE.....	116
7.4 – CHARACTERIZATION OF VACUUM PLASMA SPRAYED LAB ₆ COATINGS.....	117
APPENDIX.....	118
A.1 – THERMAL CYCLING OF BORON NITRIDE AND M26.....	118
A.2 – MATLAB PROGRAM FOR PARTITIONING OF OPTICAL PROFILOMETRY DATA.....	121

LIST OF TABLES

1.1 – Physical Properties of hBN, M26, and graphite.....	10
3.1 – Elastic constants for BN.....	50
3.2 – Thermal expansion coefficients for BN.....	50
4.1 – Selected physical constants of hexagonal BN, M26, and Isostatic Graphite.....	62
6.1 – Particle size distribution of the powder mixtures prior to vacuum plasma spraying.....	104
6.2 – Particle size distribution of all the as-deposited coatings.....	106
6.3 – Values for the work function of each VPS coating.....	109

LIST OF FIGURES

1.1 – Schematic cutaway view of the STP-100ML.....	5
1.2 – In-Situ photograph of a BPT-4000 HET	7
1.3 – Diagram of the crystal structure of hexagonal BN.....	9
1.4 – Potential profile of a typical Child-Langmuir plasma sheath.....	17
1.5 – Schematic of the energy distribution of the electrons emitted from a target.....	20
1.6 – The Boron-Lanthanum binary phase diagram.....	22
2.1 – Diagram of the important components of the plasma sheath measurement tool.....	33
2.2 – Secondary electron emission yield measurement tool.....	34
2.3 – Schematic of generalized vacuum plasma spray process.....	36
3.1 – Schematic of the HET and categorized regions of erosion.....	43
3.2 – XRD spectra for the three eroded regions in the M26 composite.....	43
3.3 – SEM secondary electron micrograph showing three distinct regions of erosion.....	45
3.4 – Scanning TEM micrograph of a foil.....	46
3.5 – X-ray photoelectron spectroscopy data.....	47
3.6 – SEM micrograph and finite element model of microstructure.....	52
4.1 – Composite of micrographs and optical profilometry maps of graphite samples.....	67
4.2 – Graph of the secondary electron yield coefficient of the graphite samples.....	68
4.3 – Roughness as a function of reduced binned areas.....	70
4.4 – The SE micrograph and the optical profilometry map of HET wall samples.....	73

4.5 – Graph of secondary electron coefficient of HET wall samples.....	73
5.1 – Schematic and photos of Hall Effect Thrusters.....	81
5.2 – Diagram of plasma cell and diagnostics.....	84
5.3 – hBN disks with machined grooves.....	85
5.4 – Geometric grooves variables and results of the optical trapping model.....	88
5.5 – Plots of the floating wall potential verses discharge voltage.....	92
5.6 - The distributions resulting from the PIC-MCC modeling.....	95
6.1 – XRD scans and SEM micrographs of the mixed powers prior to VPS.....	104
6.2 – X-Ray Diffraction scans and SEM micrographs of the VPS coatings after spraying.....	105
6.3 – Cross-sectional SEM imagery of each VPS coating.....	108
6.4 – UPS scans of each VPS coating.....	109
A.1 – Back Scattered Electron micrograph with the red crack length measurement lines.....	119
A.2 – Histograms of crack number and length.....	120

STRUCTURE OF DISSERTATION

The structure of this dissertation follows The University of Alabama guidelines for a ‘research paper’ dissertation structure. The dissertation contains seven chapters and one appendix section. The first chapter introduces the science behind Hall effect thrusters as well as the fundamentals of plasma physics and associated erosion mechanisms and electron emission behavior in materials exposed to plasmas. In addition, the key material properties of the boron nitride, the composite ceramic of boron nitride and silica, as well as lanthanum hexaboride are discussed. From this background literature review, the motivation for the scientific study is given.

Chapter 2 includes the details of the processing and characterization techniques that are explained in additional detail to compliment the abbreviated descriptions used in each of the subsequent paper chapters.

Chapter 3 is focused on characterization of the surface features of an eroded Hall effect thruster chamber wall. The individual microstructural features of the eroded surface are discussed and mechanisms that resulted in their formation are presented.

Chapter 4 aims to elucidate the effect that surface roughness on plasma stability through the quantifying secondary electron emission from varied topologies. Graphite was used as an analogue material to boron nitride, as they share a similar crystal structure and deformation behavior. Graphite alleviated surface charging issues experienced with boron nitride during the measurements under a primary electron beam.

Chapter 5 discusses the effect of large scale topology features, such as grooving, on plasma sheath stability. A series of different grooves were fabricated into boron nitride and the floating wall potential measured while in a low density plasma. The findings are explained in terms of a plasma based models.

Chapter 6 addresses the fabrication of lanthanum hexaboride as a coating. This material is a common cathode material in plasma based systems. The coatings were deposited by vacuum plasma spraying with the microstructures and work function of the varied processed coatings characterized.

Chapter 7 provides a summary of the research that concludes the findings of the dissertation and provides suggestions for future work.

The appendix contains a series of micro-cracking experiments in BN and M26 ceramics. The data base of crack density and sizes are used to support future study investigations. This was intended to provide additional characterization of the surface emission. The MATLAB© code used to partition the roughness data (from Chapter 4) is also given.

CONTRIBUTION TO RESEARCH

This dissertation has studied the effect of erosion in a series of ceramic based materials and systems. The results of which revealed underlying erosion mechanisms through the examination of surface features found on an eroded ceramic chamber wall of a Hall effect thruster. How such surface features modify the secondary electron emission properties, a behavior which is critical to understanding near-wall plasma sheath stability, was analyzed using systematically controlled topologies that mimicked similar morphologies found in the eroded surfaces. The findings revealed a characteristic length scale between emission and roughness; the roughest surface does not necessarily result in the lowest emission. Lastly, LaB_6 as a vacuum plasma sprayed cathode coating was fabricated and characterized as a possible replacement for external pressed powder cathodes. The addition of excess boron was found to densify the coating; however, the coatings had work functions (~ 4.3 eV) of that other processes suggesting contamination is still problematic in this method of fabrication. The collective results have garnered new insights into how material microstructure regulates material-plasma sheath interactions and in particular the need to quantify the topology of materials in electron emission studies.

CHAPTER 1

INTRODUCTION

1.1 – BACKGROUND AND MOTIVATION

In the past decade, there is been a growing public interest in space travel and a renewed space race. With the emergence of public-private partnerships like those between NASA and SpaceX, it has become clear that we will soon see a large expansion in access to space technologies than ever before. Because of this, there has never been a greater need to develop more efficient forms of propulsion to power this new space age. The methods to propel spacecraft all work on the basic principle of creating thrust by accelerating and expelling mass. Chemical rockets are able to obtain large levels of thrust by ejecting a very large mass of propellant quickly which enables the necessary high thrust to overcome gravity and achieve orbit. However the actual velocity of the exhaust in such chemical rockets is low, making them inefficient and thus causing them to consume propellant at a staggering rate.

In an effort to increase the efficiency of propulsion systems, systems with higher exhaust velocities is needed. This has resulted in the development of electric based propulsion. Electric propulsion systems trade off the high thrust found in chemical propellants for a significant reduction in the propellant needed for a given application [1]. Of these electric based systems, Hall effect thrusters (HETs) are attractive electric propulsion candidates for geosynchronous station-keeping and similar low-thrust space-based propulsion applications [2], [3]. HETs are capable of greater ion current density than gridded ion thrusters because of the quasi-neutrality of

the plasma used as the propulsion source [4]. They operate in a lower specific impulse regime which yields a greater thrust-to-power ratio [5]. And recent qualification life testing of the Aerojet 4.5-kW BPT-4000 HET has shown that HETs can achieve operational lifetimes of over 10,000 hours, which is comparable to the lifespan of 30,000 hours found by NASA during their Extended Life Test of a 2.3kW NSTAR ion thruster [6], [7]. Figure 1.1 details the critical component parts of a HET device, which included the focal points of this research: the protective channel/chamber wall and electron emitting hollow cathode.

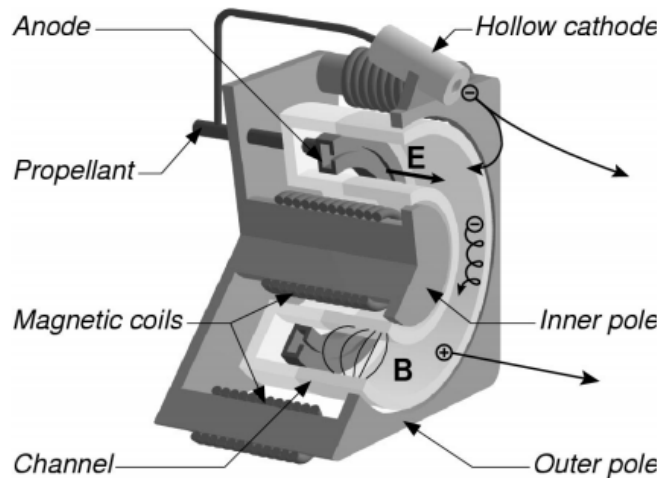


Figure 1.1 - Schematic cutaway view of the STP-100ML detailing the location of important components, the direction of the magnetic (**B**) and electric fields (**E**), and the flow of electrons and ions [8].

The HET consists of a magnetic system, comprised of the inner and outer pole, which confines a plasma, and an anode at the rear of the chamber that acts as the propellant injector. The cathode serves as the electron injector to create and sustain the plasma. The propellant gas – typically xenon or krypton gases - leaves the anode gas distributor and enters the channel whereupon the plasma discharge will occur. When the gas leaves the anode, it is in a neutral state and travels down the channel until it reaches the radial magnetic field created by the inner and outer magnetic poles shown in Figure 1.1 as “**B**”. At this stage, electrons injected by the cathode

are trapped by the magnetic field and ionize the propellant gas which is then accelerated by the electric field, “**E**” in Figure 1.1. This small potential drop, only a few millimeters wide, is sufficient to cause the plasma to leave the channel at a high velocity giving the intended propulsion.

The flow of plasma over the chamber walls creates erosion by the impact of high energy ions and electrons into its surface. This creates localized heating as well as sputtering from the surface. The chamber wall is typically in insulating ceramic and must serve as a protective surface between the plasma and the magnetic coils that confines the plasma for propulsion. Given sufficient exposure, macroscopic eroded features will develop, as shown in Figure 1.2 which developed a sinusoidal eroded pattern in a 4.5kW BPT-4000 HET after 10,400 hours of Xe plasma use. In addition to the cathode provided electrons, electron emission from the chamber wall itself will contribute to the stability of the local plasma sheath that forms over the surface. As the wall topology and chemistry evolves the emission of electrons from the wall, that regulates this sheath, will change. Creating a dynamic interaction between the plasma and the wall material it is eroding. This erosion has been identified as a key variable in limiting the functionality of these devices [5], [7]–[10].

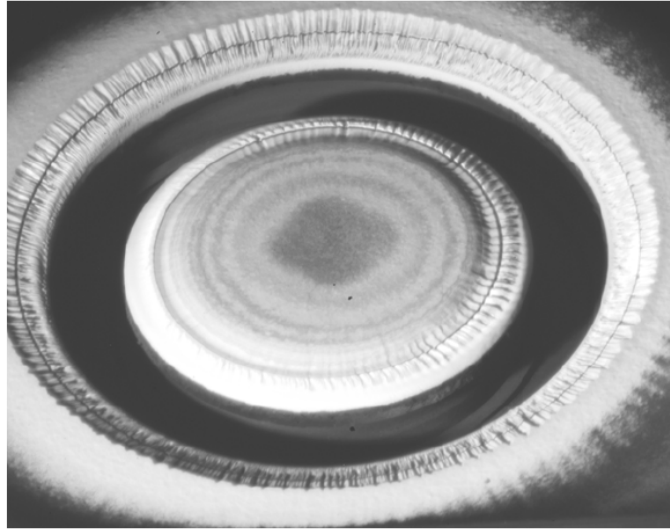


Figure 1.2 - In-Situ photograph of a BPT-4000 HET after 10,400 hours of operation [7].

As the chamber wall erodes, the surface topology is altered by the formation of ledges, kinks and other similar microstructural features [7], [11]. Depending on the length scale of the erosion pattern, such morphologies can concentrate electric fields thereby locally influencing the field emission and secondary electron emission (SEE) profiles [12]. Such features tend to be at the microscopic scale. The emission from these surfaces then dynamically influences the plasma equilibrium boundary conditions [5], [9] which then effects how the plasma erodes the surface itself, creating a very complex behavior.

The erosion and plasma equilibrium will also be influenced by larger lengths scale features. As can be seen in Figure 1.2, the erosion pattern creates variations on the macroscopic scale. Such grooving will vary the electron emission density between the grooves and thereby undulate the plasma flow. Quantifying the plasma stability on these eroded lengths scales is also equally important. Furthermore, if the ceramic wall is a composite material, each phase will erode/sputter at different rates, with the relative surface emission behavior varying. Gascon *et al.* have reported that the discharge current from a surface will be a function of material type [8].

It is clear that erosion behavior and its dynamic influence on plasma stability will vary as a function of length scales and material types. Understanding these erosion mechanisms within the microstructure and their effect on the surface electron emission behavior will lend new insights into the stability of plasmas over their surfaces. This dissertation aims to provide this characterization by addressing the mechanisms of erosion in a boride based ceramic as well as the microscopic and macroscopic erosion topologies effect on electron emission in boride or related model materials.

With these studies, the dissertation will also address a cathode material which also is intimately involved in electron emission from its surface. The cathode provides the electrons that initiate the plasma as described above and is a critical component to thruster designs. To date, these materials are typically machined from bulk monoliths of high thermionic emission materials, such as LaB₆ [13]. Since emission is a surface dependent property, this research explored an alternative processing method by vacuum plasma spraying coatings of LaB₆. Through this additive manufacturing route, increased flexibility in the geometry and substrates of cathodes that can be achieved. To date, the feasibility of these materials being coated by this processing method has not been extensively reported.

1.2 - CHAMBER WALL MATERIALS AND EROSION MECHANISMS

The HET chamber walls are typically made from either boron nitride (BN), a composite made of boron nitride with silica (referred to as Combat M26), and alumina [14]. Of these, the BN based walls have been the most successful in providing a balance between intrinsic electron emission, electrical resistivity, and good thermal shock resistance. BN has a hexagonal crystal structure ($P6_3/mmc$), shown in Figure 1.3, and like that of graphite has strong in plane bonds and weak secondary bonds between the basal planes. These weak bonds provides both graphite and

BN (also referred to as white graphite) excellent dry lubricating properties as the atomic basal plane sheets easily shear off under loading [15]. The similarity of graphite to BN, while having a higher electrical conductivity, will be a critical property in future experiments where it can serve as a model system since both deform (erode) in a similar manner. BN is also known to be chemically resistant and has a high melting temperature of $\sim 3000\text{ }^{\circ}\text{C}$ [16].

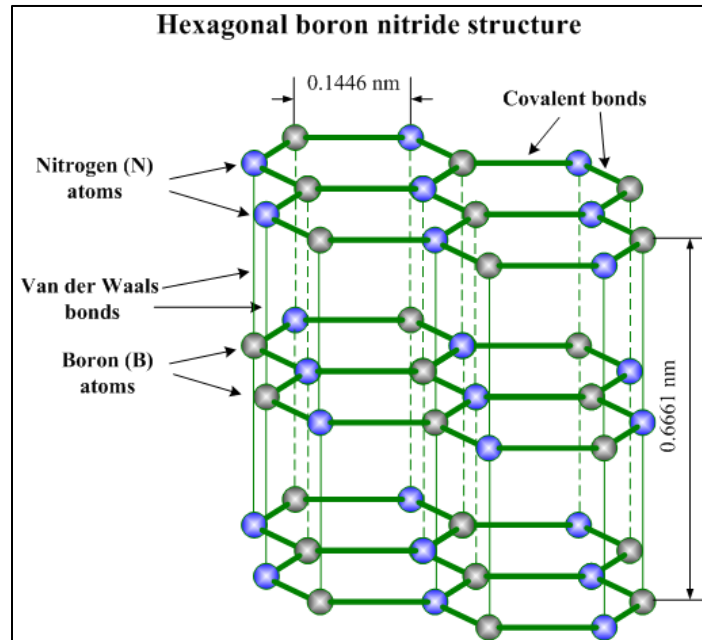


Figure 1.3 - Diagram of the crystal structure of hexagonal BN and its constituent atoms and bonding [17].

In the composite variations, amorphous silica has been used as a binder material to help improve the structural stability of the BN monoliths. It has low heat conductivity, very low thermal expansion, and is corrosive and hydration resistant [18]. The physical properties of both pure BN and the composite ceramic M26 containing both BN and silica, as given by the manufacturer Saint-Gobain ceramic materials, are found in Table 1.1 along with the similar properties for graphite.

Table 1.1 - Physical properties of hexagonal BN and the composite M26 ceramic material as indicated from the manufacturer's technical documentation [19], along with the related properties of isostatic graphite [20].

Typical Property	Units	AX05		M26		Isostatic Graphite	
Grade Name		AX05		M26		Isostatic Graphite	
Constituents		Boron Nitride(BN)		60wt.% BN	40wt.% SiO2	Graphite	
Phase		Hexagonal		Hexagonal	Amorphous	Hexagonal	
Unit Cell Volume	Å ³	35.9				35.3	
Lattice Parameters	Å	a = 2.50	c = 6.64			a = 2.46	c = 6.71
Property Directionality		Parallel	Perpendicular	Parallel	Perpendicular	Parallel	Perpendicular
Flexural Strength	MPa	22	21	62	34	38	33
Young's Modulus	Gpa	17	71				
RT Compression	MPa	25				90	66
Hardness-Knoop	Kg/mm ²	4				18	
Thermal Conductivity	W/mK	78	130	11	29	160	
Coeff. of Thermal Expansion							
@25-400°C'		-2.3	-0.7	3	0.4	3.2 - 5.7	
@400-800°C'		-2.5	1.1	2.5	0.1		
@800-1200°C'		1.6	0.4	3	0.1		
Specific Heat@25°C	J/gK	0.81		0.77			
Max. Temp - Oxidizing/Inert	°C	850/2000		1000		350/3000	
Dielectric Const. @1MHz		4	4	4.5	3.8		
Dielectric Strength	KV/mm	79		66			
RT Resistivity	Ωcm	>10 ¹³	>10 ¹⁴	>10 ¹³	>10 ¹⁴	3*10 ⁻⁵	

Since these chamber walls are subjected to a plasma environment, the secondary electron emission characteristics are essential. The physics of secondary electron emission related to plasmas will be discussed in detail in section 1.4, but in short, these are low energy electrons emitted from the surface of a material (typically with an energy < 50 eV [21]). Such electrons play a critical role in regulating the plasma sheath over the material. The secondary electron yield will be described in detail in section 1.5, but for BN and M26 these values have been found to be ~ 1.3 and 1, respectively, at a primary electron energy of 50 eV [14]. For comparison, Au, a highly conductive material, has an emission value of 0.94 at a primary electron energy of 2000 eV [22]. The high secondary electron emission of BN and silica are desirable traits in that they help to reduce the electron temperature in a stationary plasma thruster [23] which has been shown to increase HET efficiency [8].

With BN based materials identified as ideal chamber walls, their microstructural stability under ion-based erosion has been an area of active investigation [6]–[9], [24]–[31]. The identified mechanisms of erosion in these materials have included sputtering by the plasma ions bombarding the surface, thermal stresses, and ion implantation into wall material. These processes are believed to initiate crack failures created from the localized strain generated by the implanted ion species. In some cases, these implanted ions are believed to migrate to the grain boundaries, weakening them, from which intergranular cracking can become more prevalent. Though these mechanisms are generally accepted, some controversy still exists, in which mechanism is the most dominant.

In the work of Zidar and Rovey [32], a M26 chamber wall was found to have a higher amount of BN after 2000 hrs of erosion. This suggested that sputtering was likely the dominant mechanism of erosion since the binding energy of BN is nearly twice that of silica [33].

Conversely Garnier *et al.* [29], [30] and Pellerin *et al.* [25] using a similar BN-silica composite, each observed a retention of silica on the eroded surface. If sputtering was the dominate mechanism of material removal, then these results did not trend with well with the binding energies of the species in the composite. It should be noted however, that Zidar and Rovey measured surface chemistry using energy dispersive x-ray spectroscopy, a technique that has difficulty measuring low atomic number elements. More recent analysis by Yim *et al.* improves upon past assumptions of previous work which relied solely on ion scattering collisions, as ions scattered from the plasma flow and impinged on the walls. They improved on models that calculate erosion rate by including hydrodynamic flow to the plasma, it was found that near surface effects like electron balance and conductivity play in an even more important role than previously expected [34]. Other work by Schinder *et al.* have applied detailed simulations of the heterogeneous material microstructure as it undergoes erosion from the proposed sputtering conditions found in HETs. They were able to accurately recreated some of the surface features that have been found on HET chamber walls, and have estimated an average ion incidence angle of $\sim 30^\circ$ to the chamber wall surface [10].

Coupled with these experimental studies, other researchers have developed quasi-empirical models to predict HET service lifetimes and performance based on erosion rates [25], [27]–[29]. However, these models have not focused on the material underpinnings of these erosion features. These known features include topology variation (roughness), variations in the composition of the surface with erosion [29], [32], and large-length scale features such as those seen in Figure 1.2 [6]. Clearly these types of surface topology and chemical variations will create differences in electron surface emission and a variation in plasma stability over the course of the

device lifetime. Arguably, these gaps are a result of insufficient microstructural characterization of the erosion behavior and/or how those eroded surface itself influences the electron emission.

1.3 - PLASMAS AND THEIR PROPERTIES

With the various materials surveyed, the dissertation will now provide a review of the physics of plasmas. Since the research will involve and characterize the plasmas over a variety of materials surfaces, the proceeding section is aimed at highlighting the major features and properties of plasmas. The reader is referred to references [35]–[37] for further discussions. For a material to meet the criteria of being a plasma, it must satisfy the following three main criteria:

1. The physical length scale of the system (L) must be much larger than the electron

Debye length (λ_d):

$$\frac{L}{\lambda_d} \gg 1 \quad (\text{Eq. 1.1})$$

2. There must be a large number of charged particles (N_d) within a Debye sphere (a sphere with radius equal to the electron Debye length):

$$N_d = n_e \frac{4}{3} \pi \lambda_d^3 \gg 1 \quad (\text{Eq. 1.2})$$

3. There must be enough charged particles that the electron plasma frequency (ω_{pe}) is faster than the gaseous collisional timescale (ν_c):

$$\frac{\omega_{pe}}{\nu_c} \gg 1 \quad (\text{Eq. 1.3})$$

As can be seen by the above equations, to properly understand a plasma, it is important to define a number of properties for both the individual particles within the plasma as well as the plasma system as a whole. On the most basic level, the number densities of each particle species must be defined – this includes the ion number density (n_i), the electron number density (n_e), and the neutral number density (n_n). These compose the overall number density of the plasma (n_p),

the units of which are the number per square meter (m^{-3}). Since the particles are so small as compared to the unit volume, many plasmas will fall in the plasma density range of 10^{10} - 10^{20} (m^{-3}). In addition to density, the energetic state or temperature of the particles in the plasma, particularly the electrons, is also qualified. The values for electron temperature (T_e) are often much higher than those found in other systems – because they have low mass and ease to accelerate in an applied field. Typically these temperatures are defined in electron volts (eV) and range between 10^{-3} (very low density plasmas) - 10^5 eV (high density plasmas like in fusion reactions). The temperature conversion of which is $1 \text{ eV} = \sim 11600 \text{ K}$. A plasma can maintain these extreme electron temperatures because the energy transfer between the relatively small mass electrons and relatively large mass ions/neutrals is extremely slow.

Two of the most important bulk properties of plasmas are the Debye length (λ_D) and the plasma frequency (ω), each of which correspond to the “distance” and “speed” over which the plasma can respond to perturbations such as magnetic fields or physical surfaces. These two properties incorporate the above individual particle properties into the larger communal behavior of the plasma. From, which they provide a descriptor in the plasma criteria discussed earlier.

The Debye length is named after chemist Peter Debye who pioneered the study of its effect on ionic chemical solutions [38]. The origin of this characteristic length is derived from a process referred to as Debye shielding. In this processes, a strongly negative charge is introduced into the plasma field which attracts positively charged carriers (such as ions) to it while also repelling negatively charged carriers (electrons). From a longer length perspective, this charge interaction in the bulk plasma creates a negative bias of charge that is surrounded by a balance of positive charge in the form of a sphere. In this way, the positive charge carriers have shielded the

bulk of the plasma from the disturbance of the negative charge. The size of this Debye shielding layer is governed by a distance defined called the Debye length and is defined as:

$$\lambda_D = \sqrt{\epsilon_0 \kappa_B \sum_{\alpha=1}^{N_\alpha} \left(\frac{T_\alpha}{q_\alpha^2 n_\alpha} \right)} \quad (\text{Eq. 1.4})$$

where (ϵ_0) (permittivity of free space) and (κ_B) (Boltzmann constant) are fundamental constants, and the remainder is the summation of the each particle species' (α) temperature normalized by its charge (q_α) and density.

In a majority of scenarios, the Debye length is dominated by the size of the effect from the electrons in the plasma, so Eq. 1.4 can be reduced to the electron Debye length:

$$\lambda_d = \sqrt{\frac{\epsilon_0 \kappa_B T_e}{e^2 n_e}} \quad (\text{Eq. 1.5})$$

here the temperate, charge, and density of each component has been replaced with the respective values for electrons.

Next, one must consider the frequency at which the species move. This is referred to as the plasma frequency and is defined most strongly by the species which moves the fastest in the plasma. The fastest moving species will be the electrons because of their low mass and high temperature. To define the plasma frequency, one must consider a volume of ions, which is taken as stationary point charges of $+e$ while an equal volume electrons will move back and forth around these stationary point charges. As these ions are point charges, the electrons (being so much smaller than the ions) will simply pass by them without collision. This creates an overshoot scenario and where the electrons are then attracted back towards the ions. This electronic oscillatory motion defines the electron plasma frequency (ω_{pe}):

$$\omega_{pe} = \sqrt{\frac{n_e e^2}{m_e \epsilon_0}} \quad (\text{Eq. 1.6})$$

where (m_e) is the mass of the electron.

With the major individual properties of a plasma defined, the criteria of a plasma are revisited. Criterion #1 simply requires that the physical length scale (L) be sufficiently larger, but can otherwise apply to any given density or temperature. Criterion #2 scales directly with electron temperature but inversely with electron number density, so a plasma system must contain a sufficient electron temperature to regularly bring the electrons into close proximity for them to interact electrostatically. Lastly, criterion #3 requires that the plasma frequency scale based on the electron number density, while the collision frequency scales with the neutral density. Therefore a plasma must have a large enough population of electrons, in proportion to neutrals, to have its behavior governed electrically instead of collisionally. Further discussion and derivation of the criteria and equations above can be found in the following references: [35], [36], [39], [40]. With these criteria and the appropriate terms and properties defined, we can now address the plasma sheath.

1.4 - PLASMA SHEATH PHYSICS

With respect to the research here, the plasma sheath is critical in that it forms at the physical boundary between the confined plasma and the surrounding environment, which for our research is the chamber wall. The Debye shielding effect occurs at this boundary. As the physical length scale of the sheath is on the order of the Debye length scale, the sheath does not meet criteria #1 for being defined as a plasma. However, it contains plasma-like features and is a transitional space between the clearly defined plasma state and clearly defined non-plasma state (*i.e.* chamber wall). Sheaths will, in general, form in nearly any plasma system when the plasma comes in contact with an external wall or surface, as it forms in order to enforce the wall's electrical neutrality. Consequently, the sheath will not satisfy the plasma criteria of being quasi-

neutral, which is to say that the net charge of a given plasma volume is zero or that the given plasma volume is electrically neutral on average.

Within a typical sheath, a profile of the electrostatic potentials will develop and are schematically shown in Figure 1.5(a). From this figure, one can see that ions will be accelerated down the potential gradient to the regions of lower potential; conversely, electrons are accelerated up the gradient towards regions of high potential. This phenomena is analogous to the boundary layer formation in viscous fluid flow of fluid mechanics [41]. Viscous forces are insignificant over the bulk of the fluid flow, except at a critical layer near the wall where they dominate to enforce the boundary condition of the wall where the fluid can have no velocity relative to the wall. For the case of the plasma sheath, quasi-neutrality dictates that electrostatic forces are insignificant over the bulk except at the wall, where the plasma can have no charge relative to the bulk.

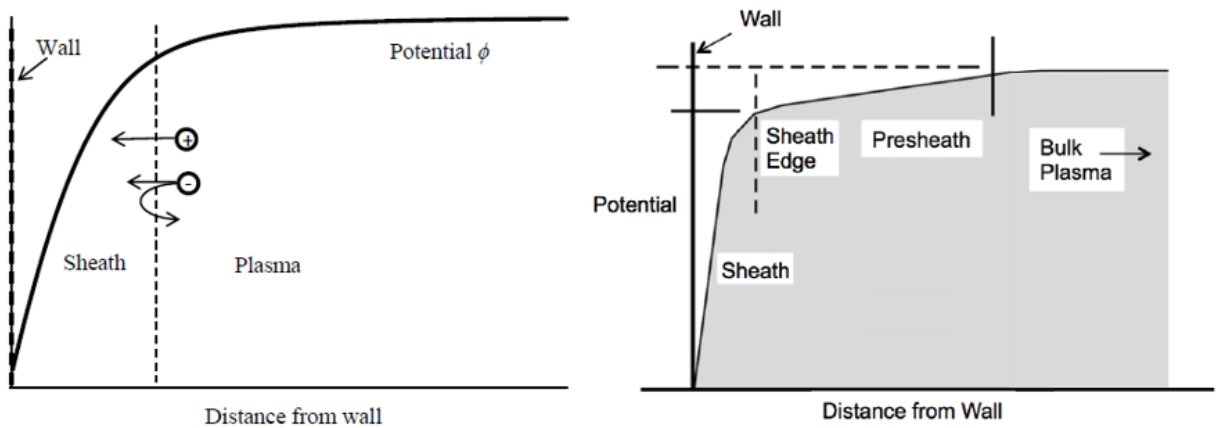


Figure 1.4 - (a) Potential profile of a typical Child-Langmuir plasma sheath. (b) Potential profile including presheath region described by Bohm. Figure Credits: [40]

The first derivation of the fundamental equations governing the properties and formation of plasma sheaths was completed by Child in 1911[42] and later finished by Langmuir. Because of their pioneering work, plasma sheaths are often referred to as Child-Langmuir sheaths and

have been very good in capturing the physics of the sheaths. The reader is referred to references [36], [40], [43] for more details.

One of the short-comings of the Child-Langmuir sheath is that it does not include the effect of plasma electrons. Hence these sheaths best describe systems with very few electrons, which would be the case for a plasma sheath near a low emission surface, such as a ceramic wall like BN. Low plasma electron conditions occur when the sheath voltage is largely negative with respect to the plasma potential. Another assumption of the Child-Langmuir sheath is that ions enter the sheath with zero velocity at a point of zero electric field strength. This assumption was overcome by Bohm [44] who incorporated it and created the Bohm criterion, which defines the speed ions must reach at the edge of the sheath [45]. The energy needed to accelerate ions to this speed results from the potential drop that leads up to the sheath, referred to as the “pre-sheath”, which allows for the degree of quasi-neutrality to gradually decrease facilitating a smooth transition between pre-sheath and sheath itself [35], [41], [43], [46], [47]. This is illustrated in Figure 1.5(b)

The boundary condition of the plasma sheath is caused from typically either an electrode or the bounding wall of the plasma discharge chamber. In the case of the electrode, the wall potential is enforced externally because the electrode is at ground. However for a bounding wall, like a chamber wall in a HET, it is electrically isolated which causes it to “float” to the potential which equalizes the positive and negative charge fluxes into the wall. This is commonly referred to as a “floating wall.” When the charge fluxes at a wall are balanced, a zero net current flow is achieved at the wall. For this particular boundary condition of zero net current, the wall is then referred to as the “floating wall potential”. For an electrically insulating material, the current is unable to flow which can then enforce other potentials that are not the than the floating potential.

Experimental measurements using a variety of techniques have provided accurate measurements of the sheath potential structure, such as, ion density profiles and ion velocity profiles [48]–[53] to understand its structure and its reference to a floating wall potential.

1.5 - ELECTRON EMISSION IN MATERIALS

As electron emission will be critical in establishing the equilibrium of the plasma near the wall, which by default creates the floating wall potential, an understanding of the emission characteristics of materials is needed. Electron emission in materials is a well-studied subject, as it has wide applications in many fields. As noted above, emission can be thermionic, which is where heat is sufficient to allow electrons to escape the surface. In other cases, impact of ions, other electrons, and photons (the photo-electric effect) can cause electron emission. For the purpose of this review, and with respect to plasmas sheaths, we are most concerned with the energy of the emitted electron rather than the details of its emission mechanism.

Secondary electron emission (SEE) are those electrons with energies less than 50 eV. These electrons are sensitive to surface topology and are often used for that purpose in scanning electron microscopy (SEM) characterization. The energy of these, as well as any other emitted electrons, are a function of the primary incident energy, E_0 , which creates them. For an SEM, this primary energy would be the acceleration of the electrons from a source, such as a field emission gun, whereupon these electrons strike the surface creating new electrons that are emitted. In a plasma, the primary energy source to create emitted electrons would be the charged species in the plasma that accelerates through the plasma sheath and strike the wall. In general, the energy distribution for all these emitted electrons will measure over a range from 0 to E_0 , as shown graphically in Figure 1.6(a). This curve is largely dominated by higher energy electrons, referred to as backscattered electrons and denoted as I and II, and originate from elastic scattering. These can be emitted electrons from the surface or reflected electrons of the primary

source, if the primary source is an electron beam as in a SEM. These electrons will scale with the atomic number, Z , of the material. Backscattered electrons (BSE) are higher energy electrons than those typically found in plasmas used in HET, as these electrons rarely have energies > 20 eV.

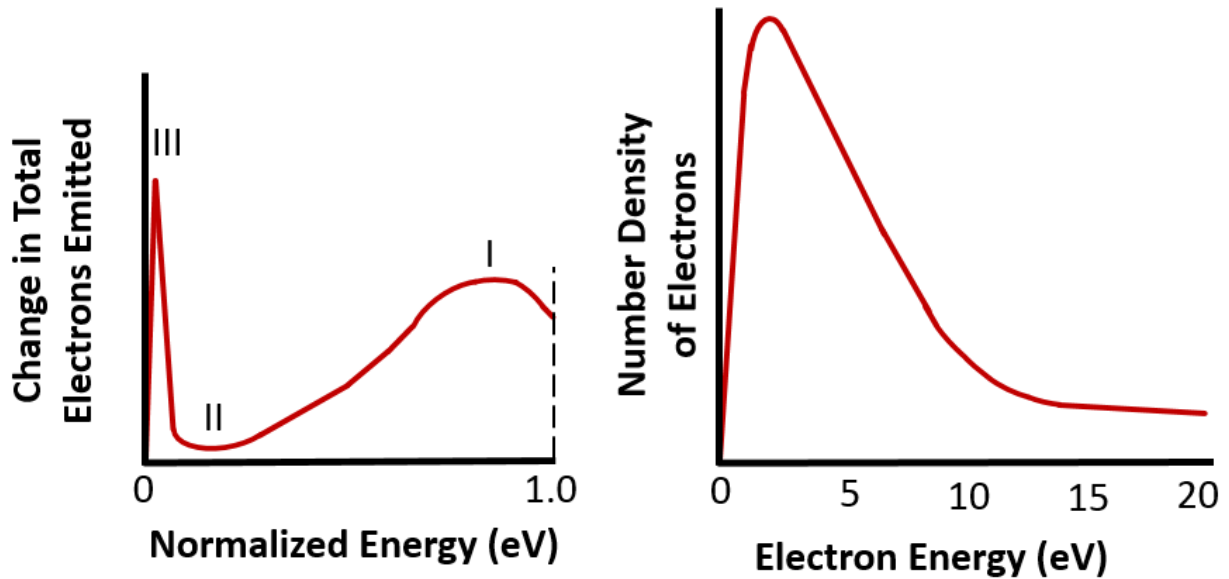


Figure 1.5 - (a) Schematic of the energy distribution of the electrons emitted from a target, highlighting regions dominated by backscattered electrons (I/II) and the secondary electrons (III). The width of region III is exaggerated. (b) Secondary electron energy distribution as measured by experiment. Figure credit [21].

The electrons, denoted as III in Figure 1.7, are the secondary electrons. As can be seen in this graph, the number of these electrons emitted are much larger than the contribution from backscattered electrons for a given energy value. This increase in electron emission is a result of secondary electrons being loosely bound outer shell electrons which receive sufficient energy during inelastic scattering to be ejected from the atom. The ejected electrons, which are now technically referred to as secondary electrons, will propagate through the material with some reaching the surface and escaping. Based on their low energy, only those electrons very near the surface (< 3 nm) are able to achieve this ejection. Though backscattered electrons could also be within this category, in terms of energy, they have been found to be negligible. In Figure 1.7(b),

the highest density of secondary electrons occurs at < 10 eV. Incident species that create secondary electrons typically arrive with much higher energies than this value. The large difference in energy between these incident source and the emitted electrons indicates that very little energy transfer occurs. Consequently, the secondary electrons that are observed have very low energy upon escaping. Finally, the total number of secondary electrons emitted, n_{SE} , normalized by the number of incident electrons, n_B , is termed the secondary electron yield coefficient, δ , and is defined by:

$$\delta = \left(\frac{n_{SE}}{n_B} \right) = \left(\frac{i_{SE}}{i_B} \right) \quad (\text{Eq. 1.7})$$

where i_{SE} and i_B are the corresponding secondary and beam currents.

1.6 - LANTHANUM HEXABORIDE PROCESSING FOR CATHODE APPLICATIONS

Unlike the chamber wall, where one wants to maximize electron emission, the cathode aims at generating a large flux of electrons to initiate and maintain the plasma. LaB_6 has been one of the most commonly used materials to achieve this behavior because of its relatively low work function (~ 2.4 eV) from which thermionic emission, at temperatures between 1500 °C and 1700 °C, can occur for extended times. It is resistant to oxidation and corrosion in acidic environments and also boasts high hardness and reasonable thermal and electrical conductivity [13], [54], [55].

LaB_6 is a cubic phase ($Pm\bar{3}m$) with a relatively narrow range of sub-stoichiometry. Figure 1.5 is the phase diagram for La-B. Other phases of lanthanum-boride, such as LaB_4 and LaB_9 , are line compounds. When LaB_6 is produced, it yields a bright purple-violet color.

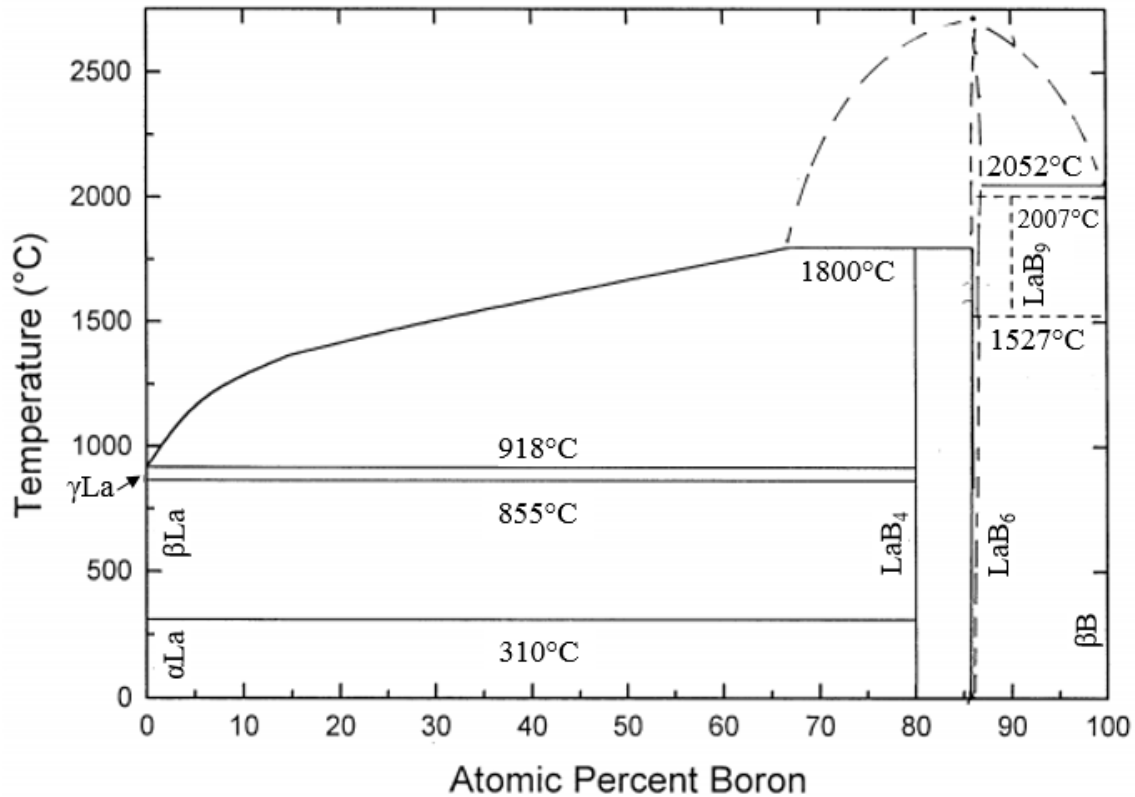


Figure 1.6 - The Boron-Lanthanum phase diagram [56].

Since thermionic emission is a surface based phenomenon, the surface orientation and composition of LaB₆ is critical. For example, the <100> orientation of has been shown to yield the maximum electron emission density [57]. Impurities on the surface or a change in stoichiometry of the surface, will also influence the emission characteristics. In the case of impurities, as they evaporate off of the surface, the intrinsic evaporation and emission of LaB₆ can be recovered making this material fairly robust [58], [59]. However, if stoichiometry is lost, the electron emission would reduce regardless of the purity of the surface [60].

LaB₆ is traditionally fabricated by a bulk sintering method and then machined into the desired shape [13]. Being with electron emission being a surface based property, the fabrication of LaB₆ may afford the development of other means of fabrication, such as coatings. Prior research on processing LaB₆ as a coating examine it typically through a chemical vapor deposition or physical vapor deposition [40]. In these methods less material is needed but whose

complex fabrication is limited by line of sight deposition. This dissertation analyzed an alternative coating/bulk processing route – vacuum plasma spraying (VPS). VPS combines both coating and bulk monolith processes in an additive fashion [61]. In this way, specific shapes can be built up to the minimum required geometry which could result in less machine time and/or less subtractive material loss. To date, the feasibility of LaB₆ deposition via VPS has not been readily explored.

1.7 - SUMMARY

This chapter has provided a general overview of materials with respect to plasma interactions. Specifically the use for HETs has been discussed because of their technical importance. Upon extended plasma exposure, the materials which are used to protect the magnetic system erodes creating changes in composition and topology. It is hypothesized that these changes will result in a dynamic interaction with the plasma and how it continues to erode the material. Based on current literature BN based materials are the primary ceramics used as a protective wall materials. However, very little is known, about the surface features created by the erosion processes and how they change the plasma sheath properties. This sheath – wall interaction will be regulated by the emission of electrons from the surface of the wall. This dissertation will then explore how BN based wall materials erode and how those topologies, as function of length scale, influence the secondary electron emission that will regulate the plasma sheath.

Besides these BN based materials, the dissertation will explore the possibility of LaB₆ fabrication. LaB₆ is a common cathode material in HETs and other plasma based devices. Since electron emission is a surface propriety, the development of coatings would provide a reduction of material costs and flexibility in design.

1.8 - REFERENCES

- [1] A. Aanesland, A. Meige, and P. Chabert, "Electric propulsion using ion-ion plasmas," *Journal of Physics: Conference Series*, vol. 162, p. 12009, Apr. 2009.
- [2] D. C. Byers and J. W. Dankanich, "Geosynchronous-earth-orbit communication satellite deliveries with integrated electric propulsion," *Journal of Propulsion and Power*, vol. 24, no. 6, pp. 1369–1375, 2008.
- [3] D. L. Brown, B. E. Beal, and J. M. Haas, "Air force research laboratory high power electric propulsion technology development," DTIC Document, 2009.
- [4] V. V. Zhurin, H. R. Kaufman, and R. S. Robinson, "Physics of closed drift thrusters," *Plasma Sources Science and Technology*, vol. 8, no. 1, p. R1, 1999.
- [5] D. Y. Oh, T. Randolph, S. Kimbrel, and M. Martinez-Sanchez, "End-to-End Optimization of Chemical-Electric Orbit-Raising Missions," *Journal of Spacecraft and Rockets*, vol. 41, no. 5, pp. 831–839, Sep. 2004.
- [6] R. R. Hofer, I. G. Mikellides, I. Katz, and D. M. Goebel, "BPT-4000 Hall thruster discharge chamber erosion model comparison with qualification life test data," in *30th International Electric Propulsion Conference*, 2007, pp. 17–20.
- [7] K. De Grys, A. Mathers, B. Welander, and V. Khayms, "Demonstration of 10,400 Hours of Operation on 4.5 kW Qualification Model Hall Thruster," presented at the *46th AIAA/ASME/SAE/ASEE Joint Propulsion Conference & Exhibit*, Nashville, TN, 2010, vol. 6698, pp. 1–10.
- [8] N. Gascon, M. Dudeck, and S. Barral, "Wall material effects in stationary plasma thrusters. I. Parametric studies of an SPT-100," *Physics of Plasmas*, vol. 10, no. 10, p. 4123, 2003.
- [9] S. Barral, K. Makowski, Z. Peradzyński, N. Gascon, and M. Dudeck, "Wall material effects in stationary plasma thrusters. II. Near-wall and in-wall conductivity," *Physics of Plasmas*, vol. 10, no. 10, p. 4137, 2003.
- [10] A. M. Schinder, M. Walker, and J. J. Rimoli, "Three-Dimensional Model for Erosion of a Hall-Effect Thruster Discharge Channel Wall," *Journal of Propulsion and Power*, vol. 30, no. 5, pp. 1373–1382, May 2014.
- [11] T. Burton, A. M. Schinder, G. Capuano, J. J. Rimoli, M. L. Walker, and G. B. Thompson, "Plasma-Induced Erosion on Ceramic Wall Structures in Hall-Effect Thrusters," *Journal of Propulsion and Power*, vol. 30, no. 3, pp. 690–695, Mar. 2014.
- [12] H. Seiler, "Secondary electron emission in the scanning electron microscope," *Journal of Applied Physics*, vol. 54, no. 11, p. R1, 1983.

- [13] D. M. Goebel, R. M. Watkins, and K. K. Jameson, "LaB₆ hollow cathodes for ion and hall thrusters," *Journal of Propulsion and Power*, vol. 23, no. 3, pp. 552–558, 2007.
- [14] P. Dawson, "Secondary electron emission yields of some ceramics," *Journal of Applied Physics*, vol. 37, no. 9, pp. 3644–3645, 1966.
- [15] A. Lipp, K. A. Schwetz, and K. Hunold, "Hexagonal boron nitride: fabrication, properties and applications," *Journal of the European Ceramic Society*, vol. 5, no. 1, pp. 3–9, 1989.
- [16] K. Taylor, "Hot pressed boron nitride," *Industrial & Engineering Chemistry*, vol. 47, no. 12, pp. 2506–2509, 1955.
- [17] P. Giraud, "Study of the Electronic Structure of hexagonal Boron Nitride on Metals Substrates," Universidad del Pais Vasco, San Sebastian, Spain, 2012.
- [18] R. Brückner, "Properties and structure of vitreous silica. I," *Journal of Non-Crystalline Solids*, vol. 5, no. 2, pp. 123–175, 1970.
- [19] "COMBAT Boron Nitride Solids," in Saint-Gobain Ceramic Materials, 2011. [Online]. Available: <http://www.bn.saint-gobain.com/uploadedFiles/SGbn/Documents/Solids/Combat-Solids-DS1.pdf>. Accessed: Oct. 02, 2016
- [20] H. O. Pierson, *Handbook of Carbon, Graphite, Diamonds and Fullerenes: Processing, Properties and Applications*. William Andrew, 2012.
- [21] J. I. Goldstein *et al.*, *Scanning Electron Microscopy and X-Ray Analysis*, 3rd Edition. New York, NY: Springer Science+Buisness Media, LLC, 2003.
- [22] Y. Lin and D. C. Joy, "A new examination of secondary electron yield data," *Surface and Interface Analysis*, vol. 37, no. 11, pp. 895–900, 2005.
- [23] J. M. Haas and A. D. Gallimore, "Internal plasma potential profiles in a laboratory-model Hall thruster," *Physics of Plasmas (1994-present)*, vol. 8, no. 2, pp. 652–660, 2001.
- [24] I. Mikellides, I. Katz, R. Hofer, and D. Goebel, "Design of a laboratory Hall thruster with magnetically shielded channel walls, phase III: Comparison of theory with experiment," *AIAA Paper*, vol. 3789, 2012.
- [25] N. Pellerin *et al.*, "Ageing of ceramics in a Hall Effect Plasma thruster," in *20th International Symposium on Plasma Chemistry (ISPC)*, 2011.
- [26] A. P. Yalin, B. Rubin, S. R. Domingue, Z. Glueckert, and J. D. Williams, "Differential sputter yields of boron nitride, quartz, and kapton due to low energy Xe bombardment," *AIAA Paper*, vol. 5314, p. 2007, 2007.
- [27] M. Gamero-Castano and I. Katz, *Estimation of Hall Thruster Erosion Using HPHall*. Pasadena, CA: Jet Propulsion Laboratory, National Aeronautics and Space Administration, 2005.

- [28] V. Kim, V. Kozlov, A. Semenov, and I. Shkarban, "Investigation of the Boron Nitride based Ceramics Sputtering Yield Under it's Bombardment by Xe and Kr ions," in *International Electric Propulsion Conference, IEPC-01-073, Pasadena, Ca*, 2001.
- [29] Y. Garnier, V. Viel, J. Roussel, D. Pagnon, L. Mange, and M. Touzeau, "Investigation of xenon ion sputtering of one ceramic material used in SPT discharge chamber," in *26th International Electric Propulsion Conference*, 1999, pp. 512–517.
- [30] Y. Garnier, V. Viel, J.-F. Roussel, and J. Bernard, "Low-energy xenon ion sputtering of ceramics investigated for stationary plasma thrusters," *Journal of Vacuum Science & Technology A: Vacuum, Surfaces, and Films*, vol. 17, no. 6, p. 3246, 1999.
- [31] J. Zhang, "Sputtering investigation of boron nitride with secondary ion and secondary neutral mass spectrometry," *Journal of Vacuum Science & Technology A: Vacuum, Surfaces, and Films*, vol. 15, no. 2, p. 243, Mar. 1997.
- [32] D. G. Zidar and J. L. Rovey, "Hall-effect thruster channel surface properties investigation," *Journal of Propulsion and Power*, vol. 28, no. 2, pp. 334–343, 2012.
- [33] M. Chen, C. Rohrbach, A. Neuffer, K.-L. Barth, and A. Lunk, "Simulation of boron nitride sputtering process and its comparison with experimental data," *IEEE Transactions on Plasma Science*, vol. 26, no. 6, pp. 1713–1717, 1998.
- [34] J. T. Yim, M. Keidar, and I. D. Boyd, "An evaluation of sources of erosion in Hall thrusters," *AIAA Paper*, vol. 3530, p. 2005, 2005.
- [35] D. M. Goebel and I. Katz, *Fundamentals of Electric Propulsion: Ion and Hall Thrusters*, vol. 1. John Wiley & Sons, 2008.
- [36] G. Hobbs and J. Wesson, "Heat flow through a Langmuir sheath in the presence of electron emission," *Plasma Physics*, vol. 9, no. 1, pp. 85–87, 1967.
- [37] A. Morozov and V. Savel'Ev, "Theory of the near-wall conductivity," *Plasma Physics Reports*, vol. 27, no. 7, pp. 570–575, 2001.
- [38] P. Debye and E. Hückel, "De la theorie des electrolytes. I. abaissement du point de congelation et phenomenes associes," *Physikalische Zeitschrift*, vol. 24, no. 9, pp. 185–206, 1923.
- [39] J. Sheehan and N. Hershkowitz, "Emissive probes," *Plasma Sources Science and Technology*, vol. 20, no. 6, p. 063001(1-22), Nov. 2011.
- [40] S. J. Langendorf, "Effects of Electron Emission on Plasma Sheaths," Ph.D Dissertation, Daniel Guggenheim School of Aerospace Engineering, Georgia Institute of Technology, Atlanta, GA, 2015.

- [41] R. Franklin, "The plasma–sheath boundary region," *Journal of Physics D: Applied Physics*, vol. 36, no. 22, p. R309, 2003.
- [42] C. Child, "Discharge from hot CaO," *Physical Review (Series I)*, vol. 32, no. 5, p. 492, 1911.
- [43] K.-U. Riemann, "The Bohm criterion and sheath formation," *Journal of Physics D: Applied Physics*, vol. 24, no. 4, p. 493, 1991.
- [44] A. Guthrie and R. K. Wakerling, *The Characteristics of Electrical Discharge in Magnetic Fields*, vol. 5. McGraw-Hill, 1949.
- [45] J. Allen, "A note on the generalized sheath criterion," *Journal of Physics D: Applied Physics*, vol. 9, no. 16, p. 2331, 1976.
- [46] K.-U. Riemann, "Bohm criterion and ion-acoustic sound barrier," *Physics of Fluids B: Plasma Physics (1989-1993)*, vol. 3, no. 12, pp. 3331–3338, 1991.
- [47] M. Benilov, "The Child–Langmuir law and analytical theory of collisionless to collision-dominated sheaths," *Plasma Sources Science and Technology*, vol. 18, no. 1, p. 14005, 2008.
- [48] M. Goeckner, J. Goree, and T. Sheridan, "Measurements of ion velocity and density in the plasma sheath," *Physics of Fluids B: Plasma Physics (1989-1993)*, vol. 4, no. 6, pp. 1663–1670, 1992.
- [49] G. Bachet, L. Chérigier, and F. Doveil, "Ion velocity distribution function observations in a multipolar argon discharge," *Physics of Plasmas (1994-present)*, vol. 2, no. 5, pp. 1782–1788, 1995.
- [50] D. Lee, G. Severn, L. Oksuz, and N. Hershkowitz, "Laser-induced fluorescence measurements of argon ion velocities near the sheath boundary of an argon–xenon plasma," *Journal of Physics D: Applied Physics*, vol. 39, no. 24, p. 5230, 2006.
- [51] D. Lee, N. Hershkowitz, and G. D. Severn, "Measurements of Ar⁺ and Xe⁺ velocities near the sheath boundary of Ar–Xe plasma using two diode lasers," *Applied Physics Letters*, vol. 91, no. 4, p. 41505, 2007.
- [52] L. Oksuz and N. Hershkowitz, "Plasma, presheath, collisional sheath and collisionless sheath potential profiles in weakly ionized, weakly collisional plasma," *Plasma Sources Science and Technology*, vol. 14, no. 1, pp. 201–208, Feb. 2005.
- [53] L. Oksuz and N. Hershkowitz, "First experimental measurements of the plasma potential throughout the presheath and sheath at a boundary in a weakly collisional plasma," *Physical Review Letters*, vol. 89, no. 14, p. 145001, 2002.

- [54] T. Lundstrom, "Structure, defects and properties of some refractory borides," *Pure and Applied Chemistry*, vol. 57, no. 10, pp. 1383–1390, 1985.
- [55] E. Storms and B. Mueller, "Phase relationship, vaporization, and thermodynamic properties of the lanthanum-boron system," *The Journal of Physical Chemistry*, vol. 82, no. 1, pp. 51–59, 1978.
- [56] M. E. Schlesinger, P. Liao, and K. E. Spear, "The B-La (boron-lanthanum) system," *Journal of Phase Equilibria*, vol. 20, no. 1, pp. 73–78, 1999.
- [57] W. Waldhauser, C. Mitterer, J. Laimer, and H. Störi, "Structure and electron emission characteristics of sputtered lanthanum hexaboride films," *Surface and Coatings Technology*, vol. 74, pp. 890–896, 1995.
- [58] J. Lafferty, "Boride cathodes," *Journal of Applied Physics*, vol. 22, no. 3, pp. 299–309, 1951.
- [59] M. Futamoto, M. Nakazawa, K. Usami, S. Hosoki, and U. Kawabe, "Thermionic emission properties of a single-crystal LaB₆ cathode," *Journal of Applied Physics*, vol. 51, no. 7, pp. 3869–3876, 1980.
- [60] S. Otani and Y. Ishizawa, "Thermionic emission properties of boron-rich LaB₆ and CeB₆ crystal cathodes," *Journal of Alloys and Compounds*, vol. 245, no. 1, pp. L18–L20, 1996.
- [61] R. C. J. Tucker, *ASM Handbook - Thermal Spray Technology*, vol. Volume 5A. ASM International, 2013.

CHAPTER 2

EXPERIMENTAL METHODS

2.1 - MATERIAL ACQUISITIONS AND INTENT

A series of different materials were chosen as subjects to be researched in this dissertation. The primary material systems of interest were hexagonal BN, the composite ceramic containing BN and silica called M26, and LaB_6 . The BN and M26 were sourced from the Saint-Gobain Ceramic Materials Company. The grade designation for the BN is AX05 and was of 99% purity, while “M26” is the grade designation for that material and is composed of 60wt.% of BN and 40wt.% silica. These materials were created by mixing the constituent powders together, then hot pressing this mixture; the manufacturer’s measured properties can be found in Figure 1.4. Hot pressing is a powder processing methodology where the powder mixture is loaded into a compression chamber. The chamber is compressed axially, like a piston, forcing the powder particles together to densify them while the whole bulk is heated through the chamber wall. This combination of heat and pressure sinters the particles into a highly dense monolith, from which smaller parts can be sectioned.

In Chapter 3, a M26 ceramic wall material was utilized in a P5 HET that was operated for 1500 hours by the joint Air Force Research Lab and University of Michigan. The HET was operated at power levels of 1.6 kW, 3 kW, and 5 kW under a number of different discharge voltages. The details of these operational parameters can be found in the following references: [1]–[3].

In Chapter 4, a number of graphite samples were procured from Tokai Carbon where it was isostatically pressed and sintered with a resulting average grain size of approximately 2 μm and a density of 99+/-0.5%. The graphite was of EC-17 grade, an ultra-fine grain electro discharge machining (EDM) grade, this ensured the graphite was as similar to the hBN material as possible that is used in HET. The samples were polished and roughened, as described in section 2.2, to the levels of 120 grit and 1200 grit to simulate the eroded surface found in the HET chamber walls.

In Chapter 5, additional AX05 grade hexagonal BN was procured in the form of 3 inch in diameter disks that were ¼ inch thick. Two of these disks were shipped to a third party machining company who used high speed cutting tools to cut channels into the surface. These channels mimicked the large scale erosion found near the end of life of some HET chamber walls.

In Chapter 6, LaB₆ powder was acquired from Materion Corporation at 99.5% purity and a particle size between 5-10 μm . The powder was separated into three batches which then had amorphous elemental boron powder, acquired from SB Boron at 95% purity, added to it so that the batches contained the following mixtures: 0% (no added boron), 5 vol% added boron, and 10 vol% added boron. The mixtures were then agglomerated using ethanol and polyvinyl butyral resin (PVB). Lastly, the mixtures were sieved to 15 - 45 μm using a 325 mesh screen to enhance flowability.

2.2 - METALLOGRAPHIC PREPARATION AND HANDLING OF MATERIALS

All materials that were described above were purchased or acquired from manufacturers in larger sections or monoliths. These were all sectioned into smaller samples for easier handling or to properly fit inside characterization equipment. These samples were sectioned using a high

speed, precision saw that uses a copper blade with an edge impregnated with a diamond composite. After sectioning, the samples that only required surface microstructure characterization were mounted in conductive phenolic resin using a hot mounting press. In general, if any sample had a surface treatment applied to it, or was referred to as “polished”, it underwent the following grinding and polishing steps:

1. Initial removal of surface protrusions and cutting marks using 120-500 grit silicon carbide (SiC) grinding paper.
2. Removal of grinding markings using 800-1200 grit SiC grinding paper.
3. Initial polishing using 9 μm diamond solution at 300 RPM and 20 N of force in a Buehler AutoMet 250 auto-polishing system.
4. Further polishing using 3 μm diamond solution at 150 RPM and 20 N of force in a Buehler AutoMet 250 auto-polishing system.
5. Final polishing using 0.05 μm silica solution at 150 RPM and 20 N of force in a Buehler AutoMet 250 auto-polishing system.

Note that as there are no times in any of these steps, the samples were visually inspected after each step to determine if the step needed repeating. Any samples that were polished, that were not mounted in phenolic powder, were polished by hand using the same procedure as above.

2.3 - MICROSTRUCTURAL AND CHEMICAL CHARACTERIZATION

The phase identification was characterized by **X-Ray Diffraction** (XRD) using a Bruker Discovery D8 diffractometer operated with Cobalt- $\text{k}\alpha$ radiation at 45 keV and 20 mA. A scan speed of 0.1 degrees/second, scanning between 10 – 130 degrees 2Θ was used. The ICDD databases were used to match the characteristic peaks with their representative indexing cards.

Scanning electron microscopy (SEM) imaging of the sample surfaces was captured using a JEOL 7000F operated between 10 keV and 30 keV, typically at a working distance of 10mm. The SEM was operated in Secondary Electron (SE) and Back-Scattered Electron (BSE) modes, with the SE mode providing high resolution topography sensitive micrographs while the BSE mode providing micrographs with atomic number contrast. **Energy Dispersive x-ray Spectroscopy (EDS)** was used in tandem with SEM to collect chemical maps in any micrographs, allowing for the highlighting of specific features with differing chemistry. Approximately 10 nm to 15 nm graphite coating was applied over the surface of any sample lacking in electrical conductivity, using a Cressington 208C Turbo Carbon Coater evaporator.

The chemical spectrums from the sample surface were quantified by **X-ray Photoelectron Spectroscopy** (XPS) in a Kratos Axis 165 operating at 12KeV and 12mA with a monochromatic Al source, scanning from 0 to 1000 eV binding energy.

Transmission electron microscopy (TEM) was done in a FEI Tecnai F20 Supertwin (Scanning) TEM operated at 200 keV. The TEM foils were prepared by a focus ion beam in-situ lift out procedure using a FEI Quanta 3D Dual Beam, the details of which can be found in reference [4]. Particular care was done in the final FIB milling steps to reduce potential Ga⁺ ion implantation artifacts through low keV ion polishing [5].

2.4 - PLASMA SHEATH MEASUREMENTS

The sheath measurements were done in collaboration with the Georgia Institute of Technology's High-Power Electric Propulsion Laboratory and was built and qualified by Dr. Samuel Langendorf [6]. For this experiment, a multi-dipole plasma device that consisted of a cylindrical aluminum cage lined with permanent magnets was used, shown in Figure 2.1. The cage confines ionizing electrons generated by emissive filaments within the device. The device is

operated under a vacuum that has a base pressure of 1.9×10^{-9} Torr and the sheath potential profile is measured using an emissive probe and the bulk plasma parameters are measured using Langmuir probe. This setup is designed to measure the sheath potential drop as it approaches the specimen surface while at different energy levels.

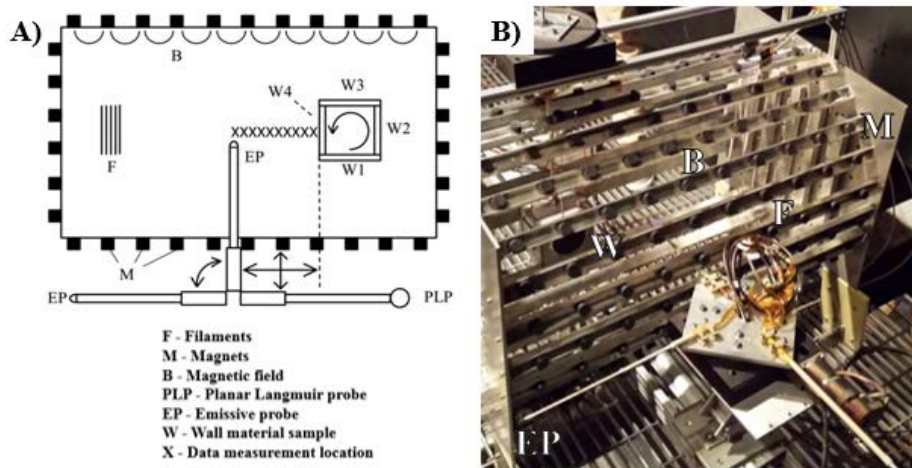


Figure 2.1 - A) Diagram of the important components of the plasma sheath measurement tool, and B) a photograph of the setup with the components labeled. The designated letters in (A) corresponds to the features shown in the image (B).

2.5 - SECONDARY ELECTRON EMISSION MEASUREMENTS

The secondary electron emission coefficient was collected in a custom constructed stainless steel vacuum chamber at the Air Force Research Lab, shown in Figure 2.2. The chamber had a base pressure of approximately 3×10^{-10} Torr pumped by mechanical and turbomolecular pumps, with the electron current being measured using a Keithley 6517A electrometer. A primary electron beam, provided by an SEM column, was rastered across the sample at the experimental accelerating voltages. The electron current was first measured while the samples were under only primary electron beam irradiation. Then each measurement was repeated while the sample was charged to +100 Volts, to recollect all escaping secondary and

backscattered electrons. The net current of re-collected electrons (i_n) and the current from the primary electron beam (i_p) was then used to calculate the SEY coefficient (δ) from:

$$\delta = 1 - \left(\frac{i_p}{i_n}\right) \quad (\text{Eq. 2.1})$$

The value for (i_n), (i_p), and δ was collected once every 5 s for 600 s, and the value for δ , at the particular accelerating voltage, was the average of the last twenty values. The error for this energy level was also calculated from this same set of values.

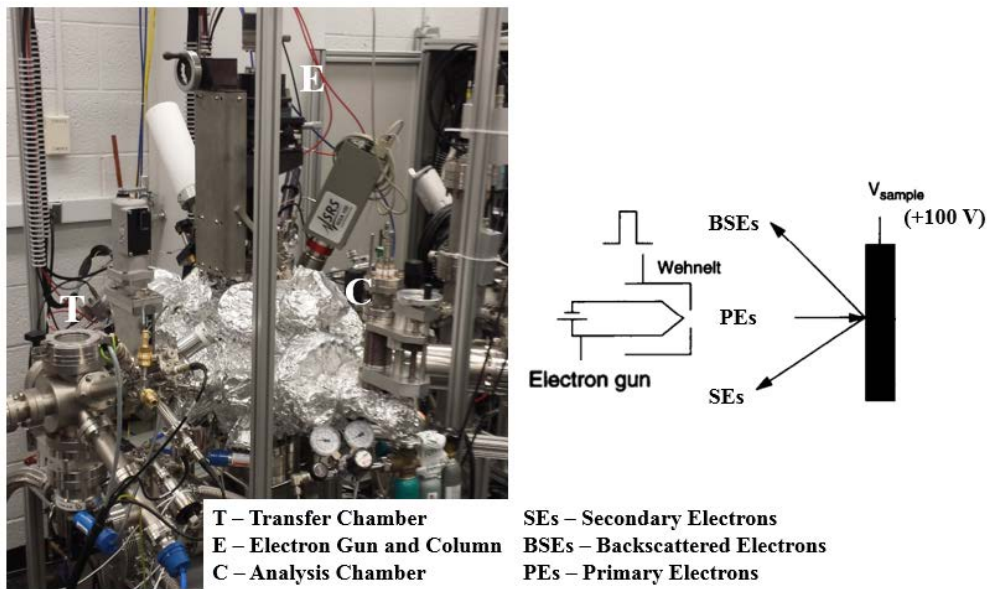


Figure 2.2 - Secondary electron emission yield measurement tool.

2.6 - ULTRAVIOLET PHOTOELECTRON SPECTROSCOPY

The work function of each sample was measured using Ultraviolet Photoelectron Spectroscopy (UPS). The UPS chamber was evacuated to a base pressure of $\sim 10^{-8}$ Pa, while the samples were pre-heated to 1000 °C (measured by a pyrometer) using an e-beam heating stage. This was intended to evaporate off any residual contaminants, surface oxides, or binder material. After which a helium photon lamp source (21.2 eV) scanned the surface up to a kinetic energy level of 30 eV. The value for the work function, Φ , was calculated from the difference in Fermi

energy level, E_F , and onset of secondary emission, E_{SE} , with the photon energy of the lamp source, E_L , removed using:

$$\Phi = E_L - (E_{SE} - E_F) \quad (\text{Eq. 2.2})$$

these values are determined graphically from the scans collected.

2.7 - VACUUM PLASMA SPRAYING PARAMETERS

Vacuum Plasma Spraying (VPS) is a thermal spraying technique which utilizes a plasma flow that has a powderized material fed into the stream, as shown in Figure 2.4. This melts the material and imparts a large force which drives the material droplets onto a substrate. These molten droplets then solidify on the substrate's surface, continued application then allows for complex coatings or monolithic parts to be built [7]. The combination of an inert atmosphere, high temperatures, and high energies makes VPS a unique processing method for materials. Many materials that have too high a melting temperature or are too sensitive to atmosphere to be fabricated through other means, but that have incredibly useful properties, can be processed using VPS. Vacuum plasma spraying is a highly tunable technique capable of generating many different material or structural features and is able to create either coatings or near net shape parts with complex geometry [8]. By changing spraying parameters or by including additives during spraying, it is possible to develop samples with a variety of microstructures and surface chemistries.

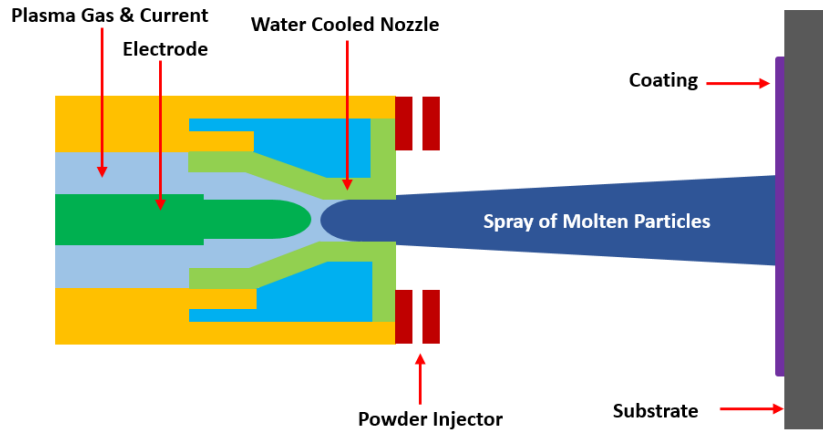


Figure 2.3 - Schematic of generalized vacuum plasma spray process

2.8 - OPTICAL PROFILOMETRY

Optical profilometry was performed to quantify the roughness of the samples, both graphite and ceramic, in Chapter 4. The samples were sent to an outside company, Evan's Analytical Group, who used a Bruker Contour GT-X8 with a 50X optical lens. Three 1.3 mm x 0.95 mm areas were scanned from each sample, each scan had a vertical resolution of 6 nm and a lateral resolution of 6 μm . Roughness statistics were then collected across the entire scanned surfaces with root mean square (RMS) roughness (S_q), given below, as the primary statistic considered:

$$S_q = \sqrt{\frac{\sum(Z_i - Z_{avg})^2}{N}} \quad (\text{Eq. 2.3})$$

where Z_i is the height of the feature, Z_{avg} is the average Z value within the scanned image, and N is the number of points in the image. For comparison to other roughness analytical methods, the geometric mean or average surface roughness (S_a) has also been calculated and is given as

$$S_a = \frac{\sum Z_i}{N} \quad (\text{Eq. 2.4})$$

2.9 - REFERENCES

- [1] J. M. Haas, "Low-perturbation interrogation of the internal and near-field plasma structure of a Hall thruster using a high-speed probe positioning system," Air Force Research Laboratory, 2001.
- [2] F. S. Gulczinski III, "Examination of the structure and evolution of ion energy properties of a 5 kw class laboratory Hall effect thruster at various operational conditions," US Air Force Research Laboratory, 1999.
- [3] T. B. Smith, "Deconvolution of ion velocity distributions from laser-induced fluorescence spectra of xenon electrostatic thruster plumes," NASA Glenn Research Center, 2003.
- [4] J. Mayer, L. A. Giannuzzi, T. Kamino, and J. Michael, "TEM sample preparation and FIB-induced damage," *MRS Bulletin*, vol. 32, no. 5, pp. 400–407, 2007.
- [5] L. Giannuzzi, "Reducing FIB Damage Using Low Energy Ions," *Microscopy and Microanalysis*, vol. 12, no. S02, pp. 1260–1261, Aug. 2006.
- [6] S. Langendorf and M. Walker, "Effect of secondary electron emission on the plasma sheath," *Physics of Plasmas (1994-present)*, vol. 22, no. 3, p. 033515(1-8), Mar. 2015.
- [7] R. A. Morris, B. Wang, D. Butts, and G. B. Thompson, "Variations in tantalum carbide microstructures with changing carbon content," *International Journal of Applied Ceramic Technology*, vol. 10, no. 3, pp. 540–551, 2013.
- [8] B. C. Schulz, B. Wang, R. A. Morris, D. Butts, and G. B. Thompson, "Influence of hafnium carbide on vacuum plasma spray processed tantalum carbide microstructures," *Journal of the European Ceramic Society*, vol. 33, no. 6, pp. 1219–1224, 2013.

CHAPTER 3

PLASMA INDUCED EROSION ON CERAMIC WALL STRUCTURES IN HALL EFFECT THRUSTERS

3.1 - ABSTRACT

A 60 wt% boron nitride (BN) - 40 wt% silica (SiO₂) hot-pressed composite, denoted as M26, was used as the insulating chamber wall for a xenon plasma Hall effect thruster operated for approximately 2000 hours at power levels between 1.5-5 kW. The chamber wall showed a range of erosion microstructures. In the heavily eroded regions, striations in the surface topology were evident with surface protrusions in the generic shape of conical tips consisting of stratified BN and silica phases. Micro-cracking along the long axis of the BN basal plane was prevalent. Through a two-dimensional finite element model, the micro-cracking has been determined to occur because of the anisotropic thermal expansion of BN in the amorphous silica matrix. Exfoliation accompanied the micro-cracking in BN and resulted in the preferential loss of BN as compared to silica in these heavily eroded regions.

3.2 - INTRODUCTION

Hall effect thrusters (HETs) are attractive candidates for geosynchronous station-keeping and similar low-thrust space-based propulsion applications [1], [2]. They are capable of much greater ion current density than gridded ion thrusters because of the quasineutrality of the plasma used as the propulsion source [3]. They also operate in a lower specific impulse regime of approximately 1500 seconds at constant power, which yields a greater thrust-to-power ratio [4]. Recent qualification life testing of the Aerojet 4.5-kW BPT-4000 HET has shown that HETs can

achieve operational lifetimes comparable to the lifespan of ion engines such as the NASA NSTAR engine [5], [6].

One of the limiting factors for HET service life and propulsion performance is the ability of the chamber wall to withstand plasma driven erosion in the discharge channels [4], [6], [7]. With the erosion of the chamber walls, the surface topology is altered. The formation of ledges, kinks and other similar microstructural features are sites which can concentrate electric fields thereby locally influencing the secondary electron emission (SEE) [8]; consequently, the plasma equilibrium boundary conditions change [4], [9]. Additionally, Gascaon et al. [9] noted that the discharge current is a function of material type. If the wall is a composite microstructure, with each phase eroding at a different rate, the relative surface emission behavior will vary depending on the surface composition as well as the surface morphology. Moreover, after the walls are fully eroded, the plasma itself can affect the magnetic field geometry by sputtering the magnetic material that was previously behind the protective wall material. Understanding the erosion mechanisms and their effect on the microstructure of the chamber wall will shed light on the physical processes that govern erosion. Based on the erosion features of the BPT-4000, observed during its 10400 hour life test, it is clear that current erosion models do not capture the physics of the lifetime limiting mechanisms. Recent research by the Jet Propulsion Laboratory has shown that there may be alternatives to avoiding these erosion mechanisms [10].

There have been many studies on ion-based erosion in ceramic materials [5]–[7], [9]–[17]. The mechanisms of erosion include sputtering by the plasma ions bombarding the surface, thermal stresses, and ion implantations into the substrate. These processes can initiate crack failures in the materials from localized strain from implanted species and possibly weaken intergranular bonding by the segregation of these implanted ions diffusing to the grain

boundaries. Specific to HETs, a detailed microstructural characterization of the surface can reveal the dominate mechanisms of erosion which lead to failure. By identifying these features, means to engineer the material for improved sustainability or performance can then be developed [18]. To date, quasi-empirical models are used to predict HET service lifetimes and performance [11], [13]–[15] with little information on the dominating mechanisms that contribute to erosion. Some features of the erosion which are not reproduced by present models include the microstructure driven surface features which are produced during erosion, variation in the composition of the surface [15], [19], and large-length scale features such as the anomalous saw tooth erosion ridges seen during the BPT-4000 qualification life test [5].

The AFRL/UM P5 HET uses a boron nitride (BN)-silica (SiO_2) composite designated as grade M (40% BN, 60% SiO_2 by weight) or M26 (60% BN, 40% SiO_2 by weight) material for the chamber wall [20]. This composite material has a good combination of machinability for fabrication, secondary electron emission for HET operation, and ion erosion characteristic properties that enable sufficient HET lifetime [21]. In particular, the high secondary electron emission is desirable to help to reduce the electron temperature in a stationary plasma thruster [20]. The reduction in electron temperature has been shown to increase HET efficiency [9]. A consequence of a heterogeneous phase composite is that each phase has a different sputtering yield, thermal expansion, and mechanical properties. These differences could contribute to non-uniform microstructural instabilities resulting from preferential erosion. This paper aims at quantifying how the composite phases within such a microstructure evolve along different regions within the HET chamber wall.

3.3 - EXPERIMENTAL SETUP

A M26 grade Combat© 60 wt% boron nitride (BN) - 40 wt% silica (SiO₂) hot-pressed composite, manufactured by Saint Gobain Ceramic Materials Company, was used as the thruster channel wall material in the HET. The M26 material was part of a P5 HET operated for approximately 2000 hours at power levels between 1.5-5 kW in xenon plasma. Please consult reference [22] for details on the service performance of the thruster. Post-plasma operation, a piece of the annular M26 wall's channel ring was mechanically removed, sectioned, and mounted onto appropriate fixture for microstructural characterization, as shown in Figure 3.1.

The phase identification of the sub-sectioned ring was determined by X-ray diffraction (XRD) using a Bruker Discovery D8 diffractometer operated with cobalt k α radiation at 45 keV and 20 mA. Scanning electron microscopy (SEM) imaging of the surface was performed using a JEOL 7000F operated at 10 keV. Since the composite material is known to have low electrical conductivity [23], the samples were either gold coated or carbon coated to reduce surface charging which leads to image degradation. Most of the micrographs were images of the direct, eroded surface; when polishing was required, the sample was auto-mechanically polished using a 9 and 3 μm diamond suspensions with a final vibromet polish with a 0.05 μm silica slurry suspension. The chemical signature from the surface was quantified by X-ray photoelectron spectroscopy (XPS) in a Kratos Axis 165 operating at 12 KeV and 12 mA with a monochrome Al source, scanning from 0 to 1000 eV binding energy. Transmission electron microscopy (TEM) was done in a FEI Tecnai F20 Supertwin (Scanning) TEM operated at 200 keV. The (S)TEM foils were prepared by a focus ion beam *in-situ* lift out procedure, the details of which can be found in reference [24]. Particular care was taken in the final focused ion beam (FIB)

milling steps to reduce potential Ga⁺ ion implantation artifacts through low keV ion polishing [25].

3.4 - RESULTS

The sectioned M26 thruster revealed three distinct regions relative to their position in the HET. These have been designated as (i) low erosion (LE) (ii) moderate erosion (ME) and (iii) high erosion (HE) regions, shown in Figure 3.1. The distinction of these regions was determined by the discoloration, shown in Figure 3.1(b), and eroded microstructures, Figure 3.1(c)-(e). The dark discoloration on the chamber wall, Figure 3.1(b), is caused by carbon re-deposition from the downstream graphite beam dump in the vacuum facility. XRD in Figure 3.2 revealed amorphous silica, evident by the broad hump between 20 and 30 degrees 2Θ , and the narrow, intense crystalline peaks identified as the crystalline hexagonal close packed (hcp) BN phase (hBN). No crystallographic phase transformations for the BN or silica phases were noted between each of the three erosion regions.

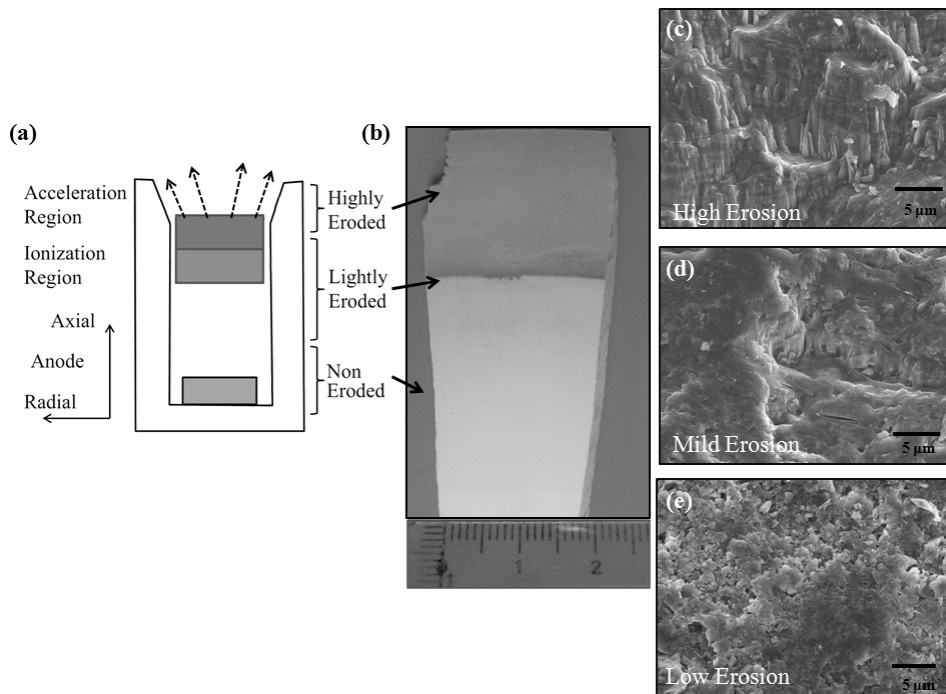


Figure 3.1 - (a) Schematic of the HET thruster and categorized regions of erosion. The different shades of grey at the top of the image represent the ionization regions of the plasma with the dashed arrows representing the discharge of the plasma out of the HET. (b) Optical image of sub-sectioned M26 composite HET wall. The bottom bar scale is in inches. The darker discoloration is from carbon re-deposition onto the wall material from the vacuum facility graphite beam dump located downstream of the HET. (c) SEM micrograph of the highly eroded region (d) SEM micrograph in the moderately eroded region. (e) SEM micrograph of the low or non-eroded region.

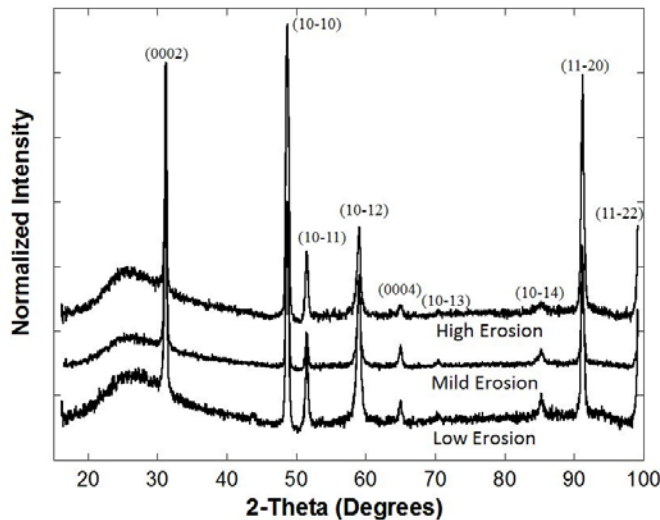


Figure 3.2 - XRD spectra for the three eroded regions in the M26 composite. The broad peak at approximately 25° 2 θ is from the amorphous silica phase; the remaining, sharp peaks in the diffractogram are indexed to BN.

The SEM micrographs of Figure 3.1(c)-(e) revealed a significantly altered surface structure between the LE, ME, and HE regions, as previously reported by Pellerin *et al.* [11]. The LE region, Figure 3.1(e), revealed a granular microstructure commonly observed in hot pressed powder mixtures. The ME region, Figure 3.1(d), revealed a polished-like surface appearance with striations of the grains and micro-cracking within the material. The HE region revealed three distinct surface features, shown in the magnified image in Figure 3.3(a). There were regions where it appeared that the BN phase exfoliated or flaked off from the matrix leaving a smooth, silica surface (denoted as “i” in Figure 3.3(a) and magnified in Figure 3.3(b)). In other regions, the surface was modified into jagged, surface protrusions (denoted as “ii” in Figure 3.3(a)). These striated and jagged surface protrusions consisted of a stratified morphology of BN and silica evident from the contrast in the SEM backscattered image of Figure 3.3(c). As previously observed in the ME region, micro-cracking, denoted as “iii” in Figure 3.3(a), was also evident in the HE region. The backscattered SEM micrograph, Figure 3(d), of a polished surface from within the HE region revealed that the micro-cracks were predominantly in the BN phases with some smaller cracks in the silica matrix.

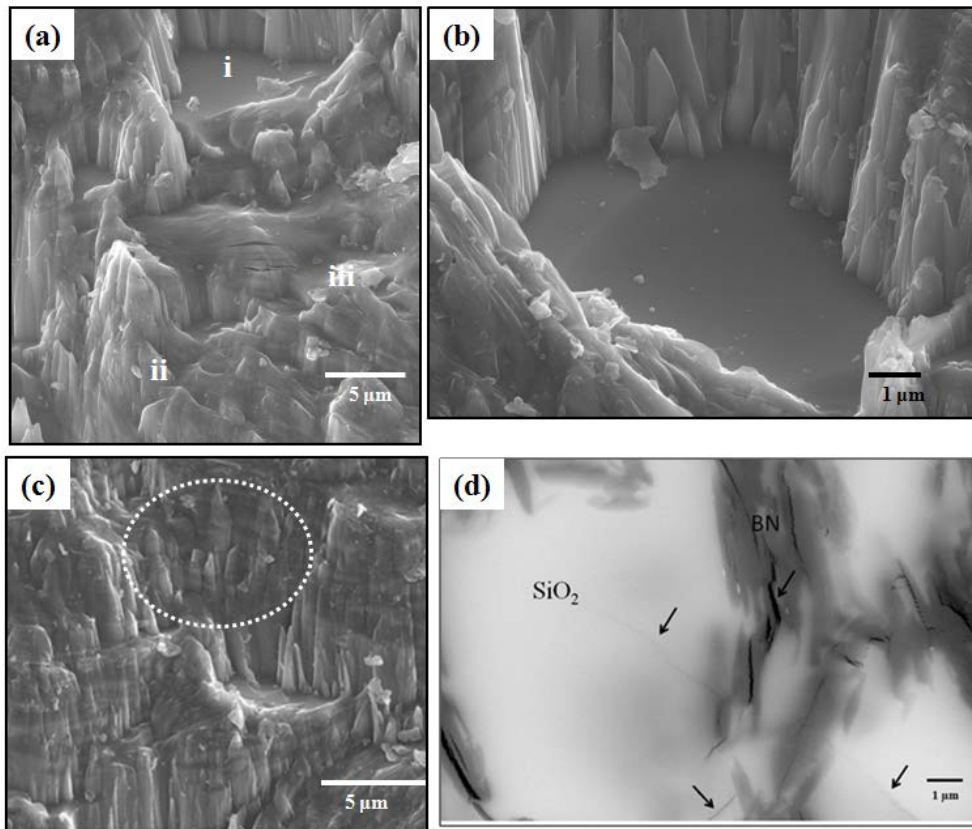


Figure 3.3 - (a) SEM secondary electron micrograph showing three distinct regions of erosion: “i” being a smooth, planar surface of silica, “ii” surface protrusions, and “iii” micro-cracking. **(b)** High magnification SEM micrograph revealing the planar surface of silica. **(c)** Backscattered SEM micrograph revealing a stratified morphology, see region in dashed circle, of BN and silica within the surface protrusions. **(d)** Polished surface showing significant micro-cracking in the BN phase (darker region) with some minor cracking in the silica (lighter region), denoted with the arrows.

The inset electron diffraction patterns in Figure 4 confirmed the crystalline hcp phase of BN and the amorphous structure of the silica. Similar to the backscattered SEM images, the high angle annular dark field micrograph of Figure 4 provides semi-quantitative atomic phase imaging with brighter contrast indicative of the higher atomic number containing species [26]. This micrograph reveals that the micro-cracks are prevalent in the BN phase, with splitting widths that are a few nanometers and several cracks present in the same fiber. These cracks did not appear to bifurcate but ran parallel along the basal plane of BN, as determined by the edge-on zone axis diffraction pattern in the inset image of Figure 3.4.

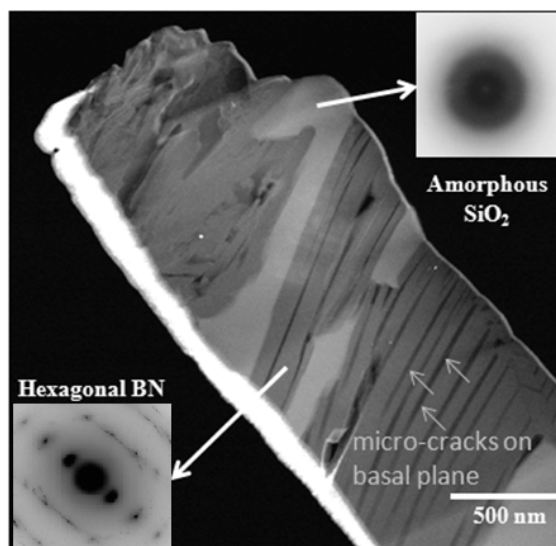


Figure 3.4 - Scanning TEM micrograph of a foil extracted from the moderate erosion region. Electron Diffraction image insets confirm the crystallography of the phases. BN zone axis [02 $\bar{2}$ 0]. The bright contrast at the bottom of foil is re-deposited material from the thinning process.

XPS revealed a relative compositional change, shown in the histogram of Figure 3.5, between each of the elements in the three eroded regions. The relative carbon content increased into the HE region which attributed to the discoloration on the sample shown in Figure 3.1(b). As the wall material became more eroded, an increase in the relative amounts of silicon and oxygen signals and a corresponding decrease in the boron and nitrogen signals were noted.

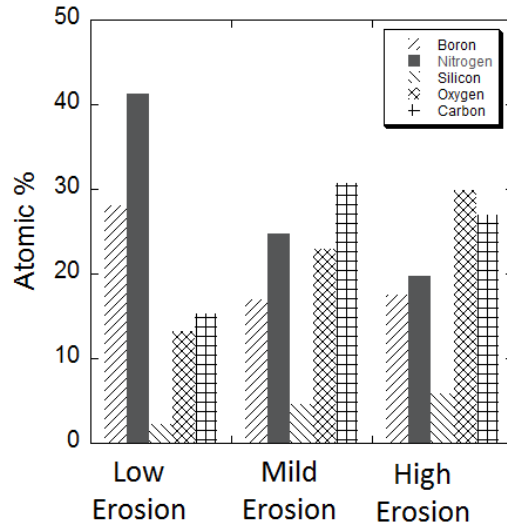


Figure 3.5 - X-ray photoelectron spectroscopy (XPS) data of each constituent element from each of the three regions.

3.5 - DISCUSSION

After 2000 operational hours, specific regions of the chamber wall surface topology showed evidence of significant variation in erosion characteristics. The variation in erosion characteristics along the axial direction of the discharge chamber material is attributed to the spatial variation in the energy of ions that impact the discharge chamber wall. Between the anode exit plane and the ionization region, Figure 3.1(a), the HE portion of the wall is exposed to neutral gas temperatures of approximately 850 to 1000 K [27]. Once the plasma ionizes and accelerates across this region, a sharp potential drop near the exit plane of the thruster occurs and the ion impact energies of the ions, within the plasma, rise from <10 eV to between 100 and 300 eV. In addition to the plasma potential profile in the axial direction, the electron temperature peak near the exit plane also causes large sheath potentials which can drive large additional changes in bombarding ion energy [28]. The increase in impact energy in this region is distinct and has a marked impact on the surface topology evident in the upstream chamber wall's microstructure shown between the micrographs in Figure 3.1(c)-(e).

The preferential retention of silica as compared to BN in the highly eroded region, Figure 3.5, roughens the surface topology by the variation in removal rates between the two phases. With longer exposures, this roughening is enhanced as the modulated surface topology would cause shadowing effects for line-of-sight ion implantation [29]. This would facilitate surface striations as seen the eroded microstructures [6]. In addition, the difference in sputtering rate between the two materials would cause shaping of the features. This is evident in the needle-like surface protrusions that formed. Upon closer evaluations, the backscattered SEM micrograph of Figure 3.3(c) revealed a stratified silica-BN structure within these protrusions. The combined effects of line-of-site impingement and subsequent sputtering behavior intrinsic to each phase contributed to the surface protrusion development.

The retention of silica, evident by the XPS measurement, is surprising considering that silica's binding energy is approximately one-half of that of BN [30] and could be expected to be more resistant to sputtering. The relative change in matrix phase composition observed in this work is in agreement with the previous report by Garnier *et al.* [15], [16] and Pellerin *et al.* [11], but is in contradiction to Zidar and Rovey [19], who reported the retention of BN. Upon closer inspection of the backscattered images in the HE region, some sections appear to have a smooth silica surfaces. The prevalent micro-cracking in the BN is suggestive of structural instability within this phase caused by mechanical stress around the grain. Consequently, the smooth features represent regions where the BN fibers exfoliated from the matrix and are no longer contained in the material. The detachment of the BN phase leaves the remnant interphase boundary between the silica and BN exposed. This suggests that the interface bonding between the species is structurally insufficient to withstand the plasma eroding environment. The lack of significant roughening on this planar region is indicative that either (a) the detachment occurred

after the plasma was turned off and the ions did not impact the surface to roughen it, and/or (b) the surrounding, higher surface features provided shielding from the majority of line-of-site ion bombardment from the plasma. For the former, the thermal cycling of the chamber walls between operational and non-operational periods would result in thermal expansion and contraction differences between the phases which could lead to detachment of certain surface phases, as will be discussed below.

The presence of the micro-cracks within the BN fiber is a result of localized stress. The sources of this stress could be from ion implantation and sputtering of the phase and/or anisotropic thermal expansion coefficients within the phases. The hcp BN phase is then strained by the impingement and implantation of the xenon ions within its close packed matrix. In HETs, accelerated ions have a range of energies between about 100 and 300 eV for a discharge voltage of 300 V [31]. In this work we assume average ion impact energy of 110 eV to account for the fact that only the radial component of the ion velocity vector is perpendicular to the material surface. Furthermore, the plume plasma potential and the cathode coupling voltage reduce the effective potential drop experienced by the ions for acceleration for a given HET discharge voltage. Based on the Monte Carlo simulation “Stopping Range of Ions in Materials (SRIM)” [32], the average implantation depth at 110 eV into BN at normal incidence is approximately 2.0 nm with a straggle distance of 1.4 nm. In contrast, silica, being amorphous, would not have any crystallographic sputtering dependent behavior and would also have more free volume because of its amorphous structure. This open structure could more easily accommodate localized strain created by the implantation of the ions. SRIM calculations show that the average implantation depth is 3.0 nm with a straggle distance of 2.2 nm for 110 eV xenon ions at normal incidence in silica. In either case, the implantation is a very near surface effect.

Though sputtering and implantation effects are possible mechanisms of creating cracks, the dominant mechanism is believed to be the anisotropic thermal expansion, of BN within the silica matrix. Because it is amorphous, silica will not have any anisotropic crystallographic thermal expansion behavior. Table 3.1 contains the elastic constants and Table 3.2 the thermal expansion coefficients for hBN. The thermal expansion coefficients were obtained from experiments conducted by Pease [33], which are in agreement with other values found in the literature [34], [35]. Since the thermal expansion coefficient in the close-packed basal plane direction is not constant, a mean value was used in the models. That is $\alpha_2 = \left(\int_0^{T_{max}} \alpha_2^{ref}(t) dt \right) / T_{max}$, where $\alpha_2^{ref}(t)$ is the temperature-dependent thermal expansion coefficient, and T_{max} is the final temperature of the model, which in this case is 800K. This guarantees the correct thermal expansion at T_{max} .

Table 3.1 - Elastic constants for BN [33]. For the indices, direction 1 corresponds to the direction perpendicular to the basal plane, whereas directions 2 and 3 are within the basal plane.

Elastic Constants [GPa]	
C₃₃₃₃	900
C₂₂₃₃	200
C₂₃₂₃	700
C₁₁₃₃	2
C₁₁₁₁	27
C₁₃₁₃	5

Table 3.2 - Thermal expansion coefficients for BN [36]. Direction 1 corresponds to the direction perpendicular to the basal plane. Values in basal plane (directions 2 and 3) are mean values over the range of temperatures.

Thermal Expansion [$10^{-6}/K$]	
α_1	40.5
α_2	-1.43
α_3	-1.43

The silica phase was assumed to be isotropic with elastic constant $E = 70 \text{ GPa}$ [33] and thermal expansion coefficient $\alpha = 0.75 \times 10^{-6}/\text{K}$ [36]. Using these values, the thermo-mechanical response within material was computed through a direct numerical simulation of the microstructure. The geometry of the microstructure was reconstructed using a finite element mesh created from a representative micrograph of the material, Figure 3.6(a)-(b). More specifically, the boundaries between the dark (BN) and light (SiO_2) phases were drawn on top of the micrograph as shown in Figure 3.6(a). Subsequently, a seed mesh size of 0.13 micrometers was specified along those boundaries. The entire region was then meshed using the prescribed boundary and seed constraints. The resulting mesh for the entire analysis domain is depicted in Figure 3.6(b). For the thermal expansion notation, the subscript for direction 1 denotes the normal to the basal plane whereas directions 2 and 3 are within the basal plane and mutually orthogonal. From the previous TEM micrograph, Figure 3.4, the basal plane was found to run parallel to the long axis of the hBN's fiber morphology. This crystallography-morphology relationship was used to estimate the approximate orientation of the hBN phase with this microstructure.

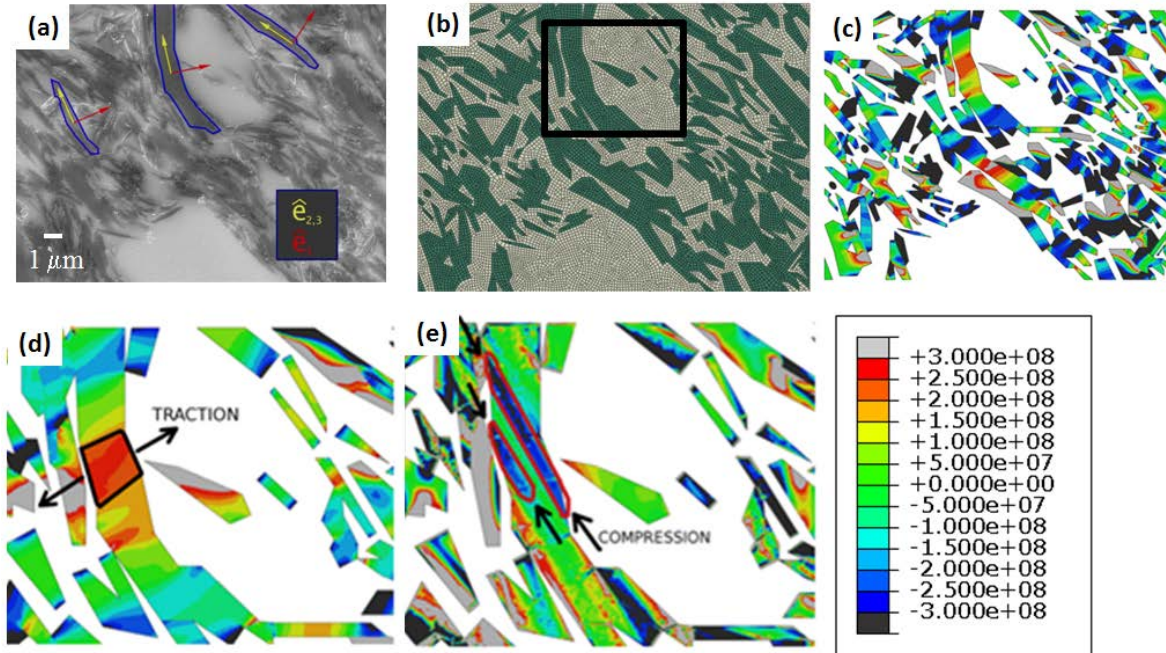


Figure 3.6 - (a) SEM micrograph of BN-silica composite microstructure. The red arrows represent vectors normal to the basal plane, the yellow arrows represent vectors within the basal plane. (b) Finite element simulated microstructure based on (a). (c) Stress component map perpendicular to the basal plane. (d) Stress component map perpendicular to the basal plane from the boxed region in (b). (e) Stress component map parallel to the basal plane from the boxed region in (b). Color coordinated stress values in Pascals.

A uniform change in temperature of 500 K was applied and the thermal stresses determined for the free thermal expansion of the sample under plane strain conditions. The BN anisotropy leads to high stresses within the microstructure evident by the stress gradients seen in Figure 3.6(c)-(d). Figure 3.6(d) shows the detail for a specific grain, taken from the box in Figure 3.6(b), in which the stress component perpendicular to the basal plane is purely tensile with values reaching 200 MPa. For the same grain, Figure 3.6(e), compressive stresses are present in the in-plane direction. This particular stress state, *i.e.* tensile perpendicular to the basal plane and compressive within the plane, could initiate micro-cracking. hBN has been previously shown to prevalently crack along the basal plane [37], which was also shown in this work. The thermal cycling values and conditions are significant and could lead to delamination cracking during the thermal loading. This cracking is evidence of the reaction of the material to anisotropic stress

states while fixed within the microstructure. The detachment of surface BN grains is in response to these states upon thermal unloading, when the overall homogenized compressive stress is relieved. This is believed to be a dominant mechanism for the exfoliation of the hBN in the post-analyzed HE region.

In summary, we believe that the observed level of thermal stresses could lead to the formation of the observed microcracks. The formation of microcracks could favor a grain detachment process leading to ejection of hBN grains on the surface of the material. This process would, in turn, expose large silica areas to the sputtering effects of the plasma. Since silica has a higher sputtering rate than hBN, this mechanism could imply higher overall erosion rates for the compound, thus limiting the lifetime of HETs.

3.6 - CONCLUSIONS

A HET wall, subjected to a xenon plasma at power levels of 1.5-5 kW for approximately 2000 hours, was characterized to determine the major features of erosion. Depending upon location in the chamber wall, the following three distinct regions were identified: (i) low erosion, LE (ii) moderate erosion, ME and (iii) high erosion, HE. The LE region did not show any distinct erosion features. The ME region showed the onset of surface roughening in the form of surface striations and protrusions from line-of-sight sputter erosion. The onset of micro-cracking in the hBN was also observed. The HE region exhibited significant surface roughening, exfoliation of hBN from the surface and micro-cracking within the hBN. In addition, a darker discoloration was present on the surface of the HE region and believed to be the result of carbon re-deposition from the vacuum facility downstream graphite beam dump onto the HET. The major source of mechanical stress that contributed to the micro-cracking is the anisotropic thermal expansion of hBN in the silica matrix. As hBN thermally expanded in the more rigid silica matrix, in response

to the high temperature plasma, stress concentrations develop resulting in micro-cracking parallel to the basal plane. In some instances, the surface hBN was liberated from the matrix material to accommodate this expansion revealing a smooth silica surface. The prevalent micro-cracking in hBN is suggestive of weak structural integrity during plasma exposure for this particular heterogeneous ceramic composite. This work highlights the need for understanding how microstructure affects thermal stresses, micro-cracking and sputtering, and how these factors may interact with each other to increase or decrease the effective erosion rate of a given material. Further knowledge in this area could prove useful for the selection of discharge channel materials in future HETs.

AUTHORS AND ACKNOWLEDGEMENTS

Thomas Burton^[1], Aaron M. Schinder^[2], German Capuano^[2], Julian Rimoli^[2], Mitchell Walker^[2], Gregory B. Thompson^{[1],#}

[1] Department of Metallurgical and Materials Engineering, University of Alabama, Tuscaloosa, AL 35487

[2] School of Aerospace Engineering, Georgia Institute of Technology, Atlanta, GA 30332 USA

contact author: gthompson@eng.ua.edu

Accepted to Journal of Propulsion and Power on October 4th 2013

DOI: 10.2514/1.B34882

The authors gratefully acknowledge FA9550-11-1-0160, Program Managers Dr. Mitat Birkan,

Dr. John Luginsland, and Dr. Ali Sayir, for support of this research.

3.7 – REFERENCES

- [1] D. C. Byers and J. W. Dankanich, “Geosynchronous-earth-orbit communication satellite deliveries with integrated electric propulsion,” *Journal of Propulsion and Power*, vol. 24, no. 6, pp. 1369–1375, 2008.
- [2] D. L. Brown, B. E. Beal, and J. M. Haas, “Air force research laboratory high power electric propulsion technology development,” DTIC Document, 2009.
- [3] V. V. Zhurin, H. R. Kaufman, and R. S. Robinson, “Physics of closed drift thrusters,” *Plasma Sources Science and Technology*, vol. 8, no. 1, p. R1, 1999.
- [4] D. Y. Oh, T. Randolph, S. Kimbrel, and M. Martinez-Sanchez, “End-to-End Optimization of Chemical-Electric Orbit-Raising Missions,” *Journal of Spacecraft and Rockets*, vol. 41, no. 5, pp. 831–839, Sep. 2004.
- [5] R. R. Hofer, I. G. Mikellides, I. Katz, and D. M. Goebel, “BPT-4000 Hall thruster discharge chamber erosion model comparison with qualification life test data,” in *30th International Electric Propulsion Conference, 2007*, pp. 17–20.
- [6] K. De Grys, A. Mathers, B. Welander, and V. Khayms, “Demonstration of 10,400 Hours of Operation on 4.5 kW Qualification Model Hall Thruster,” presented at the *46th AIAA/ASME/SAE/ASEE Joint Propulsion Conference & Exhibit*, Nashville, TN, 2010, vol. 6698, pp. 1–10.
- [7] S. Barral, K. Makowski, Z. Peradzyński, N. Gascon, and M. Dudeck, “Wall material effects in stationary plasma thrusters. II. Near-wall and in-wall conductivity,” *Physics of Plasmas*, vol. 10, no. 10, p. 4137, 2003.
- [8] H. Seiler, “Secondary electron emission in the scanning electron microscope,” *Journal of Applied Physics*, vol. 54, no. 11, p. R1, 1983.
- [9] N. Gascon, M. Dudeck, and S. Barral, “Wall material effects in stationary plasma thrusters. I. Parametric studies of an SPT-100,” *Physics of Plasmas*, vol. 10, no. 10, p. 4123, 2003.
- [10] I. Mikellides, I. Katz, R. Hofer, and D. Goebel, “Design of a laboratory Hall thruster with magnetically shielded channel walls, phase III: Comparison of theory with experiment,” *AIAA Paper*, vol. 3789, 2012.
- [11] N. Pellerin, L. Balika, S. Pellerin, C. Focsa, E. Véron, D. Pagnon, and M. Dudeck, “Ageing of ceramics in a Hall Effect Plasma thruster,” in *20th International Symposium on Plasma Chemistry (ISPC)*, 2011.
- [12] A. P. Yalin, B. Rubin, S. R. Domingue, Z. Glueckert, and J. D. Williams, “Differential sputter yields of boron nitride, quartz, and kapton due to low energy Xe bombardment,” *AIAA paper*, vol. 5314, p. 2007, 2007.

- [13] M. Gamero-Castano and I. Katz, *Estimation of Hall Thruster Erosion Using HPHall*. Pasadena, CA: Jet Propulsion Laboratory, National Aeronautics and Space Administration, 2005.
- [14] V. Kim, V. Kozlov, A. Semenov, and I. Shkarban, "Investigation of the Boron Nitride based Ceramics Sputtering Yield Under it's Bombardment by Xe and Kr ions," in *International Electric Propulsion Conference*, IEPC-01-073, Pasadena, Ca, 2001.
- [15] Y. Garnier, V. Viel, J. Roussel, D. Pagnon, L. Mange, and M. Touzeau, "Investigation of xenon ion sputtering of one ceramic material used in SPT discharge chamber," in *26th International Electric Propulsion Conference*, 1999, pp. 512–517.
- [16] Y. Garnier, V. Viel, J.-F. Roussel, and J. Bernard, "Low-energy xenon ion sputtering of ceramics investigated for stationary plasma thrusters," *Journal of Vacuum Science & Technology A: Vacuum, Surfaces, and Films*, vol. 17, no. 6, p. 3246, 1999.
- [17] J. Zhang, "Sputtering investigation of boron nitride with secondary ion and secondary neutral mass spectrometry," *Journal of Vacuum Science & Technology A: Vacuum, Surfaces, and Films*, vol. 15, no. 2, p. 243, Mar. 1997.
- [18] P. H. Mayrhofer, C. Mitterer, L. Hultman, and H. Clemens, "Microstructural design of hard coatings," *Progress in Materials Science*, vol. 51, no. 8, pp. 1032–1114, Nov. 2006.
- [19] D. G. Zidar and J. L. Rovey, "Boron Nitride hall-effect thruster channel surface properties investigation," in *AIAA Joint Propulsion Conference*, 2011.
- [20] J. M. Haas, "Low-perturbation interrogation of the internal and near-field plasma structure of a Hall thruster using a high-speed probe positioning system," Air Force Research Laboratory, 2001.
- [21] D. M. Goebel and I. Katz, *Fundamentals of Electric Propulsion: Ion and Hall Thrusters*, vol. 1. John Wiley & Sons, 2008.
- [22] J. M. Haas and A. D. Gallimore, "Internal plasma potential profiles in a laboratory-model Hall thruster," *Physics of Plasmas (1994-present)*, vol. 8, no. 2, pp. 652–660, 2001.
- [23] A. Lipp, K. A. Schwetz, and K. Hunold, "Hexagonal boron nitride: fabrication, properties and applications," *Journal of the European Ceramic Society*, vol. 5, no. 1, pp. 3–9, 1989.
- [24] J. Mayer, L. A. Giannuzzi, T. Kamino, and J. Michael, "TEM sample preparation and FIB-induced damage," *MRS Bulletin*, vol. 32, no. 5, pp. 400–407, 2007.
- [25] L. Giannuzzi, "Reducing FIB Damage Using Low Energy Ions," *Microscopy and Microanalysis*, vol. 12, no. S02, pp. 1260–1261, Aug. 2006.
- [26] Z. L. Wang, "New Developments in Transmission Electron Microscopy for Nanotechnology," *Advanced Materials*, vol. 15, no. 18, pp. 1497–1514, Sep. 2003.

- [27] S. Mazouffre, P. Echegut, and M. Dudeck, "An infrared thermography study on the thermal load experienced by a high power Hall thruster," in *International Electric Propulsion Conference*, 2005, pp. 2005–63.
- [28] R. Shastry, "Experimental characterization of the near-wall region in Hall thrusters and its implications on performance and lifetime," Jet Propulsion Laboratory, 2011.
- [29] J. T. Drotar, Y.-P. Zhao, T.-M. Lu, and G.-C. Wang, "Surface roughening in shadowing growth and etching in 2+ 1 dimensions," *Physical Review B*, vol. 62, no. 3, p. 2118, 2000.
- [30] M. Chen, C. Rohrbach, A. Neuffer, K.-L. Barth, and A. Lunk, "Simulation of boron nitride sputtering process and its comparison with experimental data," *IEEE Transactions on Plasma Science*, vol. 26, no. 6, pp. 1713–1717, 1998.
- [31] F. S. Gulczinski III, "Examination of the structure and evolution of ion energy properties of a 5 kw class laboratory Hall effect thruster at various operational conditions," US Air Force Research Laboratory, 1999.
- [32] J. F. Ziegler, M. Ziegler, and J. Biersack, "SRIM—The stopping and range of ions in matter (2010)," *Nuclear Instruments and Methods in Physics Research Section B: Beam Interactions with Materials and Atoms*, vol. 268, no. 11, pp. 1818–1823, 2010.
- [33] R. S. Pease, "An X-ray study of boron nitride," *Acta Crystallographica*, vol. 5, no. 3, pp. 356–361, 1952.
- [34] I. Hamdi and N. Meskini, "Ab initio study of the structural, elastic, vibrational and thermodynamic properties of the hexagonal boron nitride: Performance of LDA and GGA," *Physica B: Condensed Matter*, vol. 405, no. 13, pp. 2785–2794, Jul. 2010.
- [35] W. Paszkowicz, J. Pelka, M. Knapp, T. Szyszko, and S. Podsiadlo, "Lattice parameters and anisotropic thermal expansion of hexagonal boron nitride in the 10–297.5 K temperature range," *Applied Physics A*, vol. 75, no. 3, pp. 431–435, 2002.
- [36] M. Baucio, *ASM Engineered Materials Reference Book*. Materials Park, OH: ASM International, 1994.
- [37] R. W. Trice and J. W. Halloran, "Investigation of the Physical and Mechanical Properties of Hot-Pressed Boron Nitride/Oxide Ceramic Composites," *Journal of the American Ceramic Society*, vol. 82, no. 9, pp. 2563–2565, 1999.

CHAPTER 4

INFLUENCE OF SURFACE ROUGHNESS ON ELECTRON EMISSION FROM GRAPHITE AND A GRAPHITE-COATED HALL EFFECT THRUSTER CHAMBER WALL

4.1 - ABSTRACT

Destabilization of the near wall plasma sheath caused by secondary electron emission (SEE) from material surfaces is a key factor in determining the lifetimes of plasma-based devices. In this study, we address how surface roughness alters SEE using graphite and a graphite coated Hall effect thruster (HET) chamber wall that was eroded in a plasma environment as case studies. The graphite provided a reasonably high electrical conductivity surface from which secondary electron yield (SEY) measurements could be taken from as a function of various roughened surfaces produced by metallographic polishing. As expected, the smoothest surface (root mean square roughness $0.110 \pm 0.022 \mu\text{m}$) produced the highest SEY; however, a moderate rough surface ($0.990 \pm 0.019 \mu\text{m}$) had a lower yield than a rougher ($7.10 \pm 1.23 \mu\text{m}$) surface. This trend was also observed in the eroded chamber wall where the roughest surface did not result in the lowest SEY. It was also noted that the reduction effect was more pronounced in these samples than the mechanically attrition graphite; however, the difference in emission as a function of roughness in the coated samples was larger than that observed in the graphite block sample. Altogether, these results suggested a characteristic roughness length scale associated with emission which has been rationalized by differences between large and small scale variations in the roughness found on the surface.

4.2 - INTRODUCTION

Hall effect thrusters (HETs) have emerged as means for geo-synchronous station-keeping and similar space-based propulsion applications [1]–[4]. HET, and similar ion thrust based propulsion units, use quasi-neutral plasmas as a propulsion source [5]. One of the major lifetime limiting factors for these thrusters are the erosion of the ceramic chamber wall that protects the magnets, which provide fields that encase that plasma within the thruster [6]. If these walls become fully eroded, the plasma is exposed to the magnetic casings and causes failure of the propulsion device.

These chamber walls tend to be ceramics because of their high resistance to erosion, low density, and high electrical resistivity which prevents electrical grounding. Examples of these materials include hexagonal boron nitride (hBN), silica (SiO_2), and alumina (Al_2O_3) [7]. Though these materials are resistant to erosion, over extended time, the surface is modulated from the plasma exposure. This type of erosion is created by a number of factors including sputtering and the loss of material from mechanical stress produced by anisotropic thermal expansion within the ceramic material [2]. For example, Burton *et al.* reported how various surface features in a M26 (60wt.% hBN – 40wt.% amorphous- SiO_2) wall yielded both needle-like protrusions, micro-cracking, and smooth planar silica surfaces after extended plasma exposure [8].

While the properties of the bulk plasma are determined primarily by the design of the HET, the properties of the plasma sheath are controlled, in part, by the surface features of the channel wall [9], [10]. These determine the wall's response to the surface's electrical fields or affect its ability to re-emit electrons that escape the plasma and impact the wall surface. Hence, the variation of surface features dramatically changes the electron emission characteristics from the chamber wall with the plasma sheath and how the plasma sheath would then erode the

chamber wall. These re-emitted secondary electrons (SE) and back scattered electrons (BSE) have a destabilizing effect on the plasma sheath, reducing the overall energy of the sheath, though the mechanisms are not fully identified and the subject of ongoing research [11], [12]. Thus understanding the ways in which surface topological variations modify electron emission will allow for a more comprehensive understanding of the plasma sheath and thus the factors that cause erosion as well as plasma stability in HETs.

Though several studies have been conducted in the measurement of Secondary Electron Emission (SEE) from various material types [7], [13], to date, there has been little work in quantifying how surface topology of such materials influences electron emission relative to the erosion features seen in HET chamber wall systems. Langendorf and Walker [14] have recently reported how the plasma sheath potential became altered between a ‘rough’ and ‘smooth’ hBN surface, though the extent of the topology change was not reported. Regardless, this result provides experimental indications that surface topology will influence the SEE that stabilizes the plasma sheath. Such emission alterations would be paramount in controlling the stability of the plasma and how the plasma interacts with the surface in terms of erosion mechanisms. The dynamical interaction of an eroding wall, which forms various surface features, and the plasma sheath that facilitates the erosion of the surface is an area rich for research investigation.

One of the major challenges to electron emission measurements from HET materials is their low electrical conductivity. In a typical electron emission study, a primary electron beam is focused onto the surface whereupon the emitted surface electrons are captured [15]. If the sample is a dielectric, the surface will charge and repel the primary electron beam and such measurements cannot be acquired. Means to overcome this challenge have included pulsing of the primary electron beam to allow the surface to dissipate the charge build up [7]. Depending

on the experimental set up, this can be an arduous experiment to ensure all the surface charge is dissipated prior to the next beam exposure. In contrast, a high electrical conductive sample does not suffer from these issues and can readily provide emission data.

In this paper, we use graphite as an analog test case system to the commonly used hBN chamber wall [7], [16]–[18] to study how surface topology structures on the micron length scale affect emission behavior. The general emission trends between graphite and hBN as a function of increasing primary electron energy are similar, with hBN having a higher values [13], [18]. One of the key advantages of graphite for these topology studies, where the primary electron energy used for the measurements cannot be pulsed, is its high electrical conductivity, $15.5 \mu\Omega\text{-m}^{-1}$ [19]. This mitigates the prior charging issues discussed above in SEE measurements for hBN, which has an electrical conductivity of $>10^{14} \mu\Omega\text{-m}^{-1}$ [20], albeit at the expense of not providing the intrinsic SEY values of hBN.

Graphite provides this analogous test material to hBN because both materials have the primitive hexagonal based structure ($P6_3/mmc$) with strong in-plane basal bonds and weak out-of-plane van der Waal bonds. This weak out-of-plane bonding leads to anisotropic cracking between the basal planes for both materials indicative of their comparable deformation under a load. Hexagonal boron nitride is often referred to as ‘white graphite’ because of its similar flaking and lubricating properties for which graphite is known [21]. The crystallography, elastic constants, and related physical constants of graphite and BN are tabulated in Table 4.1.

Table 4.1 – Selected physical constants of hexagonal BN and the composite M26 ceramic material as indicated from the manufacturer’s technical documentation [20], along with the related properties of isostatic graphite [22]. Elastic constants of hBN [23] and graphite [24] are also provided.

Typical Property	Units	AX05		M26		Isostatic Graphite	
Grade Name		AX05		M26		Isostatic Graphite	
Constituents		Boron Nitride(BN)		60wt.% BN	40wt.% SiO2	Graphite	
Phase		Hexagonal		Hexagonal	Amorphous	Hexagonal	
Unit Cell Volume	Å ³	35.9				35.3	
Lattice Parameters	Å	a = 2.50	c = 6.64			a = 2.46	c = 6.71
Elastic Constants	GPa						
C ₁₁		750				920	
C ₁₂		150				33	
C ₃₃		33.5				30	
C ₄₄		3				2.3	
Property Directionality		Parallel	Perpendicular	Parallel	Perpendicular	Parallel	Perpendicular
Flexural Strength	MPa	22	21	62	34	38	33
Thermal Conductivity	W/mK	78	130	11	29	160	
Coeff. of Thermal Expansion							
@25-400°C'		-2.3	-0.7	3	0.4	3.2 - 5.7	
@400-800°C'		-2.5	1.1	2.5	0.1		
@800-1200°C'		1.6	0.4	3	0.1		
RT Resistivity	Ωcm	>10 ¹³	>10 ¹⁴	>10 ¹³	>10 ¹⁴	3*10 ⁻⁵	

Though graphite is not a typical HET chamber wall material, like hBN, it has been used to understand the basic behavior of electron emission [25]. For example, graphite has been the used in other plasma field studies where the electron temperatures are similar to HETs (10-50 eV) [3], [4] but the plasma densities being much higher, e.g. travelling wave tubes [26]–[28] and fusion reaction plasmas [29]–[31]. Graphite has also been considered as part of a magnetic

containment system for a HET plasma, and if developed, would potentially bypass the chamber wall erosion [32]. In these examples, the focus of the research has been on erosion rates under a variety of radiation and plasma conditions [29], [33]–[35] with not specific attention to the electron emission as a function of its roughened topology created by the erosion. In this research we aim to add to these studies by specifically addressing topology-electron emission links using a systemically attrition graphite sample as well as a graphite coated HET whose surface has been explicitly roughened by plasma bombardment.

Since HET plasma based erosion can take thousands to tens of thousands of hours of exposure [2], the simulated modulated surface topologies through mechanical attrition (using various grades of metallographic grinding and polishing pads) enables us to be able to provide a range of roughness conditions in a reasonable period of time. From these roughness values, the general trends between roughness and electron emission can then be obtained. We will then compare these trends to the roughened surfaces of a plasma exposed hBN-based composite. These features will be coated with graphite to reduce, if not eliminate, the charging issues mentioned above. Though coating the surface will again give the emission characteristics of graphite, it provides a coverage of the topology allowing us to reasonably provide a conducting surface that mimics the underlying roughness of the chamber wall that was created from plasma exposure. By eliminating the charging issue under direct primary electron beam exposure, one can deduce how the relative electron emission changes based on the various roughness features created by the plasma-eroded chamber wall.

4.3 - EXPERIMENTAL SETUP

EC-17 grade, ultra-fine grain Electro Discharge Machining (EDM) graphite was chosen as the case study material. This was done to ensure that the graphite was as similar to the hBN material as possible that is used in HET. This graphite was acquired from Tokai Carbon where it was isostatically pressed and sintered with a resulting average grain size of approximately 2 μm with a density of 99+/-0.5 %. The hBN used in the plasma chamber wall was composed of 60 wt.% hBN- 40 wt.% amorphous silica, denoted as M26 Combat© manufactured by Saint-Gobain. The silica was used as a binder to help improve the structural strength of the composite. The hBN grains were of similar size to the graphite. The M26 HET chamber wall was sectioned from a P5 Xenon plasma thruster that was operated at 1.5-5.0 kW for approximately 2000 hrs [6]. Two different regions of erosion – denoted as high and mild erosion – were secured. The details of the characterization of the erosion patterns in this wall material can be found in reference [8]. Both sets of samples – graphite and M26 - were sectioned into approximately 1cm x 1cm squares with thicknesses of approximately 5 mm.

All of the samples were mounted into 3.175 cm cold mount pucks using a Buehler SamplKwik acrylic cold mounting system which were then cut out of the mount post grinding or polishing. For the samples denoted as *polished*, they were all polished to 0.05 μm using an alumina-based solution. The two *roughened* graphite samples had their surfaces mechanically attrition with either a 120 grit (~125 μm particulate diameter) or 1200 grit (~15.3 μm particulate diameter) SiC metallographic grade paper. Post grinding/polishing, all of the samples were cleaned of any surface contaminates by ultrasonic vibration in acetone followed by rinsing in isopropanol and deionized water and finally dried under compressed air. X-ray Photo-spectroscopy (XPS) performed in a Kratos Axis 165 XPS/Auger confirmed the removal of any

polishing containments prior to SEY measurements. The M26 chamber wall materials exposed to the plasma were not mounted and polished in any manner but left in their as-eroded condition. To prevent surface charging, they were mounted onto a 15 mm x 15 mm piece of tantalum foil with carbon tape on the backside of the sample after which an approximately 10 nm to 15 nm graphite coating, measured using a quartz crystal balance, was applied over the surface using a Cressington 208C Turbo Carbon Coater evaporator. Though the roughness of these features would likely prevent complete conformal coverage over all the surface because shadowing created by the roughness itself for line-of-sight sputtering, the coating was found to be sufficient to eliminate charging.

The samples surfaces were imaged by scanning electron microscopy (SEM) using a JEOL 7000 at 1000 x magnification at a working distance of 10.0 mm and acceleration voltage of 10 keV while imaging in secondary electron (SE) mode. Optical profilometry, to quantify the roughness, was performed by Evan's Analytical Group using a Bruker Contour GT-X8 with a 50X optical lens. Three 1.3 mm x 0.95 mm areas were scanned from each sample where each scan had a vertical resolution of 6 nm and a lateral resolution of 6 μ m. Roughness statistics were then collected across the entire scanned surfaces with root mean square (RMS) roughness (S_q), given below, as the primary statistic considered:

$$S_q = \sqrt{\frac{\sum(Z_i - Z_{avg})^2}{N}} \quad (\text{Eq. 4.1})$$

where Z_i is the height of the feature, Z_{avg} is the average Z value within the scanned image, and N is the number of points in the image. For comparison to other roughness analytical methods, the geometric mean or average surface roughness (S_a) has also been calculated and is given as

$$S_a = \frac{\sum Z_i}{N} \quad (\text{Eq. 4.2})$$

The secondary electron emission coefficient was collected in a custom constructed stainless steel vacuum chamber at a base pressure of approximately 3×10^{-10} Torr pumped by mechanical and turbomolecular pumps, with the electron current being measured using a Keithley 6517A electrometer. A primary electron beam was rastered across each sample at accelerating voltages between 50 eV to 100 eV and then 100 eV to 400 eV at 100 eV step sizes. The electron current was first measured while the samples were under only primary electron beam irradiation. Then each measurement was repeated while the sample was charged to +100 volts, to recollect all escaping secondary and backscattered electrons. The net current of re-collected electrons (i_n) and the current from the primary electron beam (i_p) are then used to calculate the SEY coefficient (δ) from:

$$\delta = 1 - \left(\frac{i_p}{i_n} \right) \quad (\text{Eq. 4.3})$$

The value for (i_n), (i_p), and δ was collected once every 5 s for 600 s, and the value for δ , at the particular accelerating voltage, was the average of the last twenty values. The error for this energy level was also calculated from this same set of values.

4.4 – RESULTS AND DISCUSSION

4.4.1 - GRAPHITE SAMPLES AND TOPOLOGY DRIVEN REDUCTION IN EMISSION

The SEM micrographs and optical profilometry height maps of the graphite samples can be seen in Figure 4.1. From these images, one can easily discern the ever increasing level of surface roughness. At the highest roughness, the clear and coarse polishing lines are evident within the surface. At all levels of polishing, the graphite revealed jagged features which has been termed flaking. The RMS roughness (S_q) and the average roughness (S_a) for the polished graphite was $0.110 \pm 0.022 \mu\text{m}$ and $0.070 \pm 0.004 \mu\text{m}$, for the 1200 grit graphite was $0.990 \pm$

0.019 μm and $0.780 \pm 0.022 \mu\text{m}$, and for the 120 grit graphite was $7.10 \pm 1.23 \mu\text{m}$ and $5.60 \pm 0.842 \mu\text{m}$ respectively.

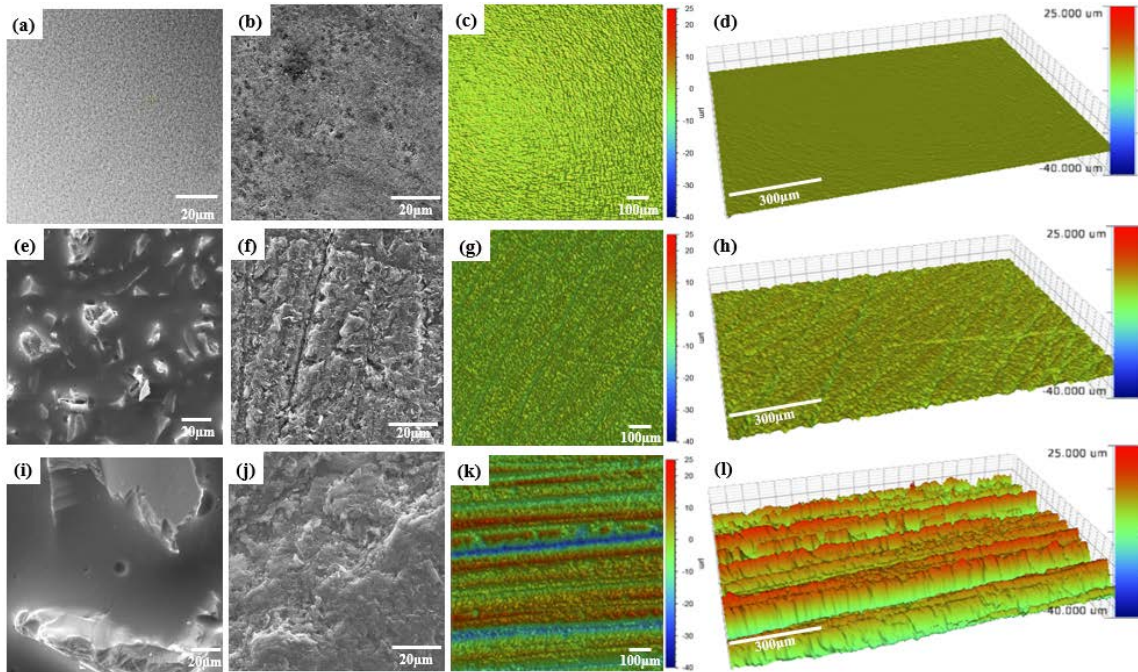


Figure 4.1 - (a) JEOL 7000 secondary electron micrograph of the 0.050 μm silica spheres used to polish the smooth graphite surface, (b) secondary electron micrograph of the polished graphite surface, and the (c) optical profilometry plan view and (d) 3D map of the polished graphite surface ($S_q = 0.110 \mu\text{m}$). (e) Secondary electron micrograph of the 1200 grit SiC polishing pad and (f) micrograph of the 1200 grit graphite surface, and optical profilometry (g) plan view and (h) 3D map of the 1200 grit graphite surface ($S_q = 0.990 \mu\text{m}$). (i) Secondary electron micrograph of the 120 grit SiC polishing pad and (j) micrograph of the 120 grit graphite surface, and Optical profilometry (k) plan view and (l) 3D Map of the 120 grit graphite surface ($S_q = 7.10 \mu\text{m}$).

The SEY coefficient as a function of primary electron beam energy and surface roughness is plotted in Figure 4.2(a). As to be expected, the polished graphite surface ($S_q = 0.110 \mu\text{m}$) had the highest SEY coefficient, with a maximum value near 300 eV. The smooth and planar surface provided the conditions where the vast majority of electrons were able to emit from the surface and contribute to the measurement. The two roughened surfaces exhibited a decrease in emission from the smooth surface with equivalent emission values at primary beam energies greater than 300 eV. However, upon decreasing the primary beam energy, a deviation

in emission was noted, with the roughest surface – graphite 120 grit ($S_q = 7.10 \mu\text{m}$) – having a slightly higher emission than the graphite 1200 grit ($S_q = 0.990 \mu\text{m}$) sample. In Figure 4.2(b), the standard deviation error at the 200 eV primary beam energy are shown confirming that this difference is statistically significant. As all the graphite material used here was from the same source and tested in the same unit, with the only difference being the surface preparation, the variance in emission is inked to the character of the surface features.

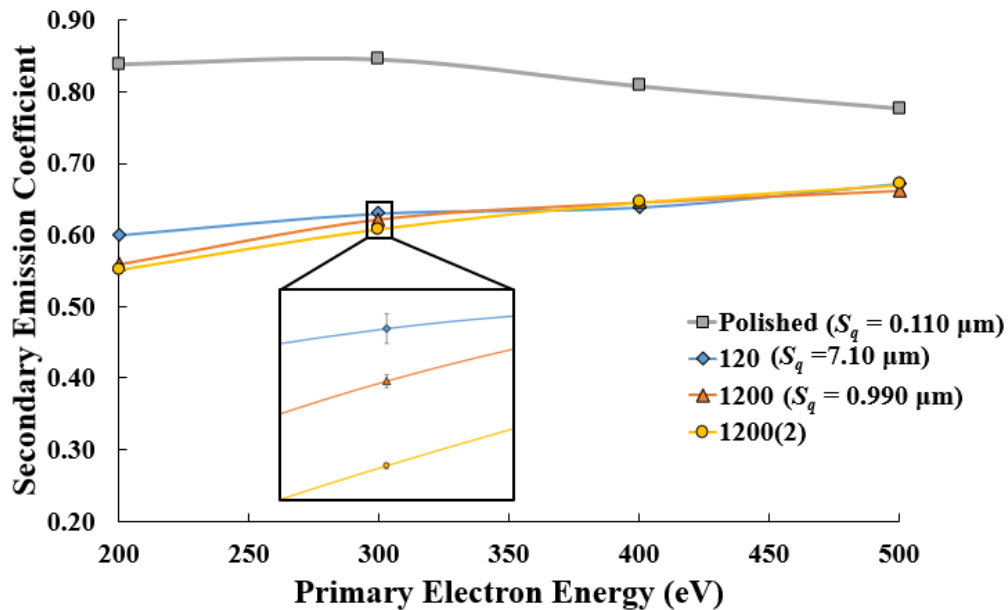


Figure 4.2 – A plot of the measured secondary electron yield coefficient for the graphite samples at each energy level. Note that the roughest sample, 120 grit, does not correspond to the lowest emission response. The insert shows the low level of error found in the measurement technique.

From these scans, it appears that a critical length scale influences the SEY coefficient when the primary beam energy is low. One could assume that the rougher the surface, the lower the SEY as more of the surface could obstruct emission. However, this is not the case. The graphite 120 grit roughest surface ($S_q = 7.10 \mu\text{m}$) has a SEY coefficient value that is lower than the graphite 1200 grit surface ($S_q = 0.990 \mu\text{m}$) when the primary electron energy is lower than 300 eV. At the lowest energies, SEE would be the most sensitive because the electrons would need sufficient energy to escape. Langendorf [37] reported a ray trace model for electron

trapping as a function of modulated topologies to investigate this type of behavior. In his model, as the depth of a groove increased, the probability of an emitted electron to escape the groove decreased because it had a greater opportunity to collide and be absorbed by the side walls within the groove. Similarly, if the spacing between grooves decreased, then the emission would decrease, for a fixed groove depth, because less surface area above the groove would be present. This is in agreement with Ye *et al.*'s finding that a reduction of SEY will occur for an increasing aspect ratio, as shown in their experimental and modeling of silver and copper surfaces arranged as cylindrical wells [38].

To illustrate the effect of roughness as a function of length scale, the average roughness values have been re-plotted as a function of partition area in Figure 4.3 with the error being the deviation of such averages. Hence for the largest partitioned area, this is taken as the entire surface roughness, with the subsequent partitioning of that area in ever reducing half-values of the preceding size. By reducing the scanned area and reporting the average and standard deviation of the roughness between different areas, one can glean how at smaller viewed length scales, the measured roughness changes and varies between ever smaller and smaller areas.

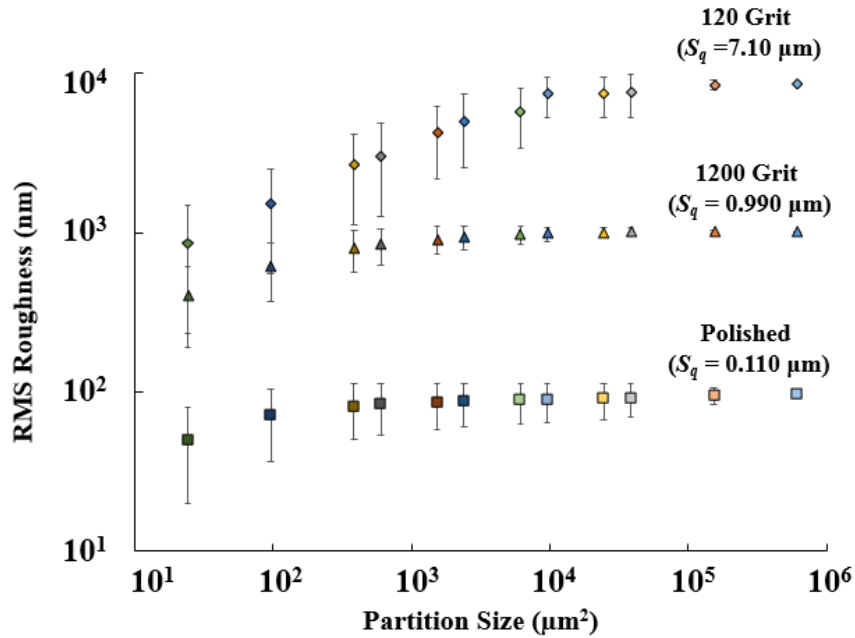


Figure 4.3 - The roughness as a function of reduced binned area for the analyzed graphite samples.

As can be seen in Figure 4.3, for the smoothest surface, as the sampling area or partitioned size decreased, there was very little change in roughness indicating that at both small and larger fields of view, the surface is relatively uniform in its roughness. In contrast, for the 120 and 1200 grit samples, as one reduced the partitioned size, the mean roughness dramatically decreased meaning that at a finer feature size, the mean surface is less rough. However, the large error bars within each partitioned size does indicate dramatic variations from sampled region to sampled region. By considering the mean value for each partitioned size, the onset for notable reduction in mean roughness occurred at approximately $10^3 \mu\text{m}^2$ and $10^4 \mu\text{m}^2$ for the 1200 and 120 grit conditions respectively. At partitioned sizes of $10^2 \mu\text{m}^2$, the RMS roughness between the two surfaces is statistically equivalent and may explain why, at higher primary beam energies, the two surfaces exhibit equivalent emission coefficients.

Considering the extremes in partitioned size, the mean values at $10 \mu\text{m}^2$ and $10^6 \mu\text{m}^2$ are outside each other's standard deviation error indicating that the roughness of the surface does

statistically decrease as one views an ever decreasing field of view. This change is most notable in the graphite 120 grit – or the largest macroscopic roughness. At the finest partition size, it was equivalent to the majority of values quantified for the 1200 grit graphite. Hence, at the finest length scales, the differences in roughness are not as large between each of the surfaces. The inability for these values to converge to the values of the smooth surface for smallest sampling sizes is contributed to the resolution limitations of the optical imaging device.

From Figure 4.3, the influence of the macroscale roughness became less and less pronounced. Hence a surface may have an overall coarser macroscopic roughness but at a finer length scale, the roughness differences are less pronounced and their effect on the trapping electrons less effective. Such an effect can be inferred from the optical profilometry scan of the 120 grit surface in Figure 4.1(i). Large scale scratch lines can be seen in this image. These features are formed from the larger particulates used in the 120 grit paper, shown in Figure 4.1(g). Though these particulates are larger, and yield a rougher surface or one with deeper grooves, their size does leave a smoother surface if the field of view is limited. Moreover, the larger particulates will also produce a surface with the spacing between each polishing line to be further apart. For the 1200 grit paper, the particulates, Figure 4.1 (d), are finer than the 120 grit creating a reduced overall roughness (a less deep groove) as well as a finer spaced variation of topology as the polishing lines are closer. Though the overall surface for the 1200 grit is smoother than the 120 grit, if the surface modulations are sufficiently modulated at a finer scale it can reduce the emission. However, if these finer scale modulations eventually become sufficiently smoothed –i.e. the polished graphite – electron emission can be recovered and increased.

Though the roughness of the 120 grit is still larger than the 1200 grit, which refers to the groove depths, the limited lateral spatial resolution of the optical profilometer prevented the necessary resolution to quantify the roughness between the polished lines. Based on the SEM micrographs of Figure 4.1, one can infer that the spacing between the polished lines created by the particulates from the polishing paper surface would be further apart for the 120 grit sample as compared to the 1200 grit sample. Between such polished lines, the material surfaces would be smooth (no deep grooving) and yield high emission regions. Hence, one must consider both groove depth and spacing for the trapping of electrons as reported by Langendorf [37] and Ye *et al.* [38] Thus how the roughness is imparted or creates the surface topology is equally important.

Comparing our results to a previous study, our SEY values are smaller overall [18]. Unfortunately, in this study, the roughness of the graphite as well as its grade was not provided, and may explain the discrepancy between our results and these results. In addition Balcon *et al.* used a kelvin probe for more careful measurement of the incident and secondary electron populations from graphite, but also did not report the grade nor surface roughness of the graphite. Thus, not only does the feature scale (groove depth and spacing) need to be specified but also the grade and roughness may also need to be considered between studies.

4.4.2 - ANALYSIS OF GRAPHITE COATED HET WALL SAMPLES

To determine if a roughness dependence of SEY existed in the M26 chamber wall, a material whose topology evolved under a plasma erosion environment, the SEY coefficient from the mild and high eroded surfaces topologies was measured (via a graphite surface coating). Figure 4.4 is the SEM micrographs and optical profilometry of each of the relevant HET surfaces. The RMS roughness (S_q) and average roughness (S_a) of the mild erosion HET wall was $4.00 \pm 0.950 \mu\text{m}$ and $3.00 \pm 0.880 \mu\text{m}$, respectively, and highly eroded HET wall was $5.80 \pm$

0.750 μm and $4.70 \pm 0.670 \mu\text{m}$, respectively. As seen in Figure 4.5, the highly eroded ($S_q = 4.00 \mu\text{m}$) surface exhibited a higher emission than the mild eroded ($S_q = 5.80 \mu\text{m}$) surface at primary beam energies lower than 300 eV. As with the graphite, the higher roughness surface does not necessarily result in the lowest emission. At 400 eV the mild eroded surface peaks in emission and slightly exceeds that of the higher eroded surface. Upon further increases in the primary beam energy, the emission for both surfaces decreases.

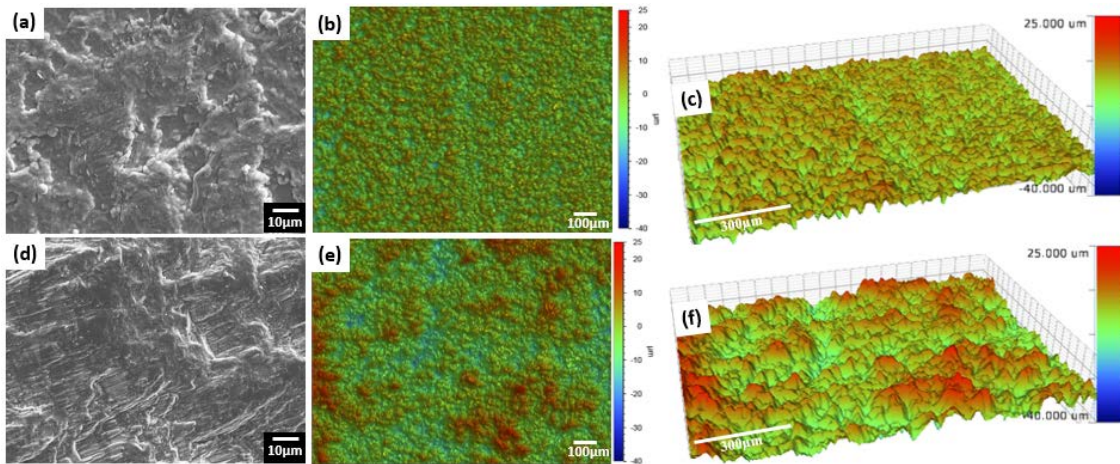


Figure 4.4 – (a) JEOL 7000 secondary electron micrograph and optical profilometry (b) profile view and (c) 3D map of the mild erosion HET surface. (d) The secondary electron micrograph and optical profilometry (e) profile view and (f) 3D map of the high erosion HET surface.

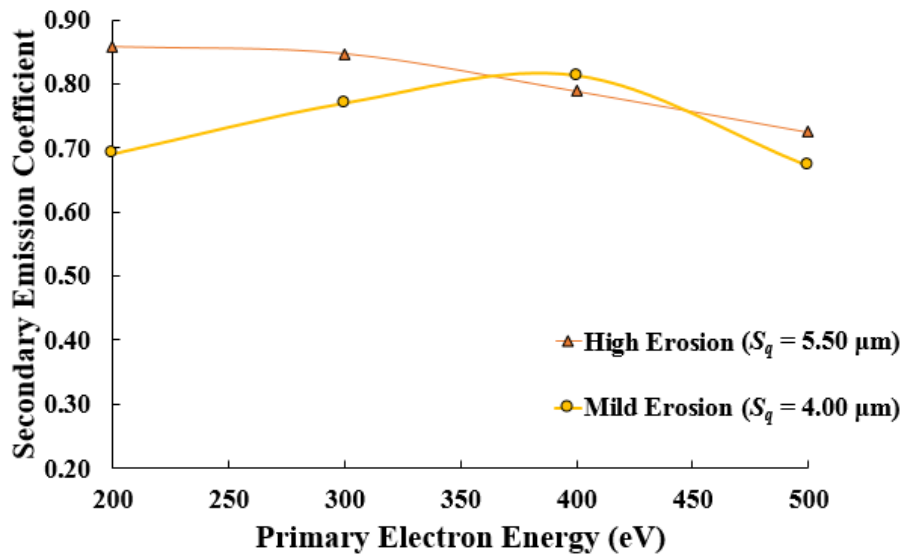


Figure 4.5 - The secondary electron coefficient measured at certain primary electron energy levels of the graphite coated HET chamber wall samples.

While the roughness of the mild and high erosion surfaces are similar, the emission statistics reveal a substantially larger emission differences (~18%) at the lowest primary electron energy studied. In comparison, the graphite 120 and 1200 grit prepared surfaces were almost an order of magnitude different in roughness but revealed much smaller emission differences (~8%). This difference in emission is believed to be a result of the topological differences in roughness. Though the RMS values provide a quantitative measure of roughness, it does not necessarily capture the morphology of that surface roughness. Viewing Fig 4.1 and 4.3, it is readily apparent that the topologies themselves are very different. These feature specific topologies could be used to explain the differences in emission with the roughness, *i.e.* groove and depth. Deciphering a quantifiable means of capturing the types of topological differences is the subject of future work. Regardless of the roughness differences between the graphite and graphite coated chamber wall, both samples reported that the roughest surface does not necessarily result in the lowest SEY at lower primary electron beam energies, or energies more associated with higher secondary emission.

Finally, we note that the differences in the absolute emission coefficient values for the graphite and graphite coated wall materials which shared similar RMS values. This difference is contributed to the HET not providing a complete conformal film coverage over the surface because of line of sight deposition. This could leave original wall surfaces available to emit. Such differences may also explain why the emissions as a function of the extent of roughness varied between the two studies. As was discussed earlier, the complexity of this compound surface of graphite and M26 makes quantitative comparison impossible. Clearly the use of graphite and mechanical attrition provided a much more controlled experiment for measurements.

4.5 – CONCLUSIONS

This study investigated how surface roughness influenced the SEE behavior in both graphite and in a graphite coated HET chamber wall that had a modulated surface roughness. Graphite provided an ideal case study in that it was electrically conductive for ease SEY measurements and shares common crystallography with hBN, a common HET chamber wall. It was found that the smoothest surface yielded the highest SEY. This was expected because such a surface would have very limited obstructions for electron emission. However, the roughest surface did not have the lowest SEY. Rather a surface with moderate roughness yielded the lowest emission. At sufficiently high electron beam energies (> 300 eV), the emission between these two roughened graphite samples became equivalent. The difference in emission for lower energies for the two roughened surfaces was explained in terms of a reduction of the roughness as a function of a finer field of view. Though a surface may have an overall coarse roughness, emission comes from a local surface which, in of itself, could be smoother. How surface roughness is reduced at a finer length scale must also be considered. For the roughest graphite surface (120 grit), a noticeable change in the mean roughness value occurred at a portioned size that was an order of magnitude larger in area than that of the moderate roughness surface (1200 grit). Thus, the roughest surface does not necessary mean the lowest emission. Similarly, a graphite coated plasma eroded chamber wall, which had a coarser and moderate eroded regions showed similar behavior, with the moderate roughness having lower emission at lower primarily electron beam energies. Collectively, this suggest that a critical length scale in terms of roughness existed for the SEY from these materials.

AUTHORS AND ACKNOWLEDGEMENTS

Thomas S. Burton¹, Tyson C. Back², Steven B. Fairchild², and Gregory B. Thompson^{1, a)}

1) *Department of Metallurgical and Materials Engineering, University of Alabama, Tuscaloosa, Alabama, 35401, USA*

2) *Wright-Patterson Air Force Base, 3005 Hobson Way, Dayton, OH, 45433, USA*

The authors would like to gratefully acknowledge the support of grant AFOSR-FA9550-11-1-0160 and Abhishek Kumar for his technical assistance in the partitioning of the roughness data.

4.6 - REFERENCES

- [1] D. Y. Oh, T. Randolph, S. Kimbrel, and M. Martinez-Sanchez, “End-to-End Optimization of Chemical-Electric Orbit-Raising Missions,” *Journal of Spacecraft and Rockets*, vol. 41, no. 5, pp. 831–839, Sep. 2004.
- [2] K. De Grys, A. Mathers, B. Welander, and V. Khayms, “Demonstration of 10,400 Hours of Operation on 4.5 kW Qualification Model Hall Thruster,” presented at the *46th AIAA/ASME/SAE/ASEE Joint Propulsion Conference & Exhibit, Nashville, TN, 2010*, vol. 6698, pp. 1–10.
- [3] N. Gascon, M. Dudeck, and S. Barral, “Wall material effects in stationary plasma thrusters. I. Parametric studies of an SPT-100,” *Physics of Plasmas*, vol. 10, no. 10, p. 4123, 2003.
- [4] S. Barral, K. Makowski, Z. Peradzyński, N. Gascon, and M. Dudeck, “Wall material effects in stationary plasma thrusters. II. Near-wall and in-wall conductivity,” *Physics of Plasmas*, vol. 10, no. 10, p. 4137, 2003.
- [5] A. Aanesland, A. Meige, and P. Chabert, “Electric propulsion using ion-ion plasmas,” *Journal of Physics: Conference Series*, vol. 162, p. 12009, Apr. 2009.
- [6] R. R. Hofer, I. G. Mikellides, I. Katz, and D. M. Goebel, “BPT-4000 Hall thruster discharge chamber erosion model comparison with qualification life test data,” in *30th International Electric Propulsion Conference, 2007*, pp. 17–20.
- [7] V. Viel-Inguibert and others, “Secondary electron emission of ceramics used in the channel of SPT,” in *28th International Electric Propulsion Conference, Toulouse, France, 2003*.
- [8] T. Burton, A. M. Schinder, G. Capuano, J. J. Rimoli, M. L. Walker, and G. B. Thompson, “Plasma-Induced Erosion on Ceramic Wall Structures in Hall-Effect Thrusters,” *Journal of Propulsion and Power*, vol. 30, no. 3, pp. 690–695, Mar. 2014.

- [9] D. M. Goebel and I. Katz, *Fundamentals of Electric Propulsion: Ion and Hall Thrusters*, vol. 1. John Wiley & Sons, 2008.
- [10] R. Franklin, "The plasma–sheath boundary region," *Journal of Physics D: Applied Physics*, vol. 36, no. 22, p. R309, 2003.
- [11] G. Hobbs and J. Wesson, "Heat flow through a Langmuir sheath in the presence of electron emission," *Plasma Physics*, vol. 9, no. 1, pp. 85–87, 1967.
- [12] M. Campanell, A. Khrabrov, and I. Kaganovich, "General cause of sheath instability identified for low collisionality plasmas in devices with secondary electron emission," *Physical Review Letters*, vol. 108, no. 23, p. 235001, 2012.
- [13] P. Dawson, "Secondary electron emission yields of some ceramics," *Journal of Applied Physics*, vol. 37, no. 9, pp. 3644–3645, 1966.
- [14] S. Langendorf and M. Walker, "Effect of secondary electron emission on the plasma sheath," *Physics of Plasmas (1994-present)*, vol. 22, no. 3, p. 033515(1-8), Mar. 2015.
- [15] A. Shih, J. Yater, C. Hor, and R. Abrams, "Secondary electron emission studies," *Applied Surface Science*, vol. 111, pp. 251–258, 1997.
- [16] N. Pellerin *et al.*, "Ageing of ceramics in a Hall Effect Plasma thruster," in *20th International Symposium on Plasma Chemistry (ISPC)*, 2011.
- [17] V. Kim, V. Kozlov, A. Semenov, and I. Shkarban, "Investigation of the Boron Nitride based Ceramics Sputtering Yield Under it's Bombardment by Xe and Kr ions," in *International Electric Propulsion Conference, IEPC-01-073, Pasadena, Ca*, 2001.
- [18] N. Balcon, D. Payan, M. Belhaj, T. Tondu, and V. Inguibert, "Secondary electron emission on space materials: evaluation of the total secondary electron yield from surface potential measurements," *IEEE Transactions on Plasma Science*, vol. 40, no. 2, pp. 282–290, 2012.
- [19] "Isotropic graphite - fine carbon -," in TOKAI CARBON CO., LTD. [Online]. Available: http://www.tokaicarbon.co.jp/en/products/fine_carbon/isotropic.html. Accessed: Oct. 24, 2016.
- [20] "COMBAT Boron Nitride Solids," in Saint-Gobain Ceramic Materials, 2011. [Online]. Available: <http://www.bn.saint-gobain.com/uploadedFiles/SGbn/Documents/Solids/Combat-Solids-DS1.pdf>. Accessed: Oct. 02, 2016
- [21] K. A. Schwetz, "Boron carbide, boron nitride, and metal borides," *Ullmann's Encyclopedia of Industrial Chemistry*, 1985.

- [22] H. O. Pierson, *Handbook of Carbon, Graphite, Diamonds and Fullerenes: Processing, Properties and Applications*. William Andrew, 2012.
- [23] J. Green, T. Bolland, and J. Bolland, "Theoretical elastic behavior for hexagonal boron nitride," *The Journal of Chemical Physics*, vol. 64, no. 2, pp. 656–662, 1976.
- [24] P. P. Gillis, "Calculating the elastic constants of graphite," *Carbon*, vol. 22, no. 4, pp. 387–391, 1984.
- [25] M. Woods, B. Hopkins, G. Matthews, G. McCracken, P. Sewell, and H. Fahrang, "An investigation of the secondary-electron emission of carbon samples exposed to a hydrogen plasma," *Journal of Physics D: Applied Physics*, vol. 20, no. 9, p. 1136, 1987.
- [26] D. Shiffler, J. Nation, L. Schachter, J. Ivers, and G. Kerslick, "A high-power two stage traveling-wave tube amplifier," *Journal of Applied Physics*, vol. 70, no. 1, pp. 106–113, 1991.
- [27] A. Curren and T. Fox, "Traveling-wave tube efficiency improvement with textured pyrolytic graphite multistage depressed collector electrodes," *IEEE Electron Device Letters*, vol. 2, no. 10, pp. 252–254, 1981.
- [28] R. Kompfner, "Travelling-wave tubes," *Reports on Progress in Physics*, vol. 15, no. 1, p. 275, 1952.
- [29] G. Federici *et al.*, "Plasma-material interactions in current tokamaks and their implications for next step fusion reactors," *Nuclear Fusion*, vol. 41, no. 12, p. 1967, 2001.
- [30] T. Yamashina and T. Hino, "Plasma-surface interactions of graphite as nuclear fusion material," *Applied Surface Science*, vol. 48, pp. 483–497, 1991.
- [31] R. Hawryluk *et al.*, "Fusion plasma experiments on TFTR: A 20 year retrospective," *Physics of Plasmas (1994-present)*, vol. 5, no. 5, pp. 1577–1589, 1998.
- [32] D. M. Goebel, R. R. Hofer, I. G. Mikellides, I. Katz, J. E. Polk, and B. N. Dotson, "Conducting wall Hall thrusters," *IEEE Transactions on Plasma Science*, vol. 43, no. 1, pp. 118–126, 2015.
- [33] D. Goebel *et al.*, "Erosion of graphite by high flux hydrogen plasma bombardment," *Nuclear Fusion*, vol. 28, no. 6, p. 1041, 1988.
- [34] F. Meyer, H. Krause, and L. Vergara, "Measurements of chemical erosion of ATJ graphite by low energy impact," *Journal of Nuclear Materials*, vol. 337, pp. 922–926, 2005.
- [35] A. Borisov, W. Eckstein, and E. Mashkova, "Sputtering and ion-induced electron emission of graphite under high-dose nitrogen bombardment," *Journal of Nuclear Materials*, vol. 304, no. 1, pp. 15–20, 2002.

- [36] R. Cimino *et al.*, “Can low-energy electrons affect high-energy physics accelerators?,” *Physical Review Letters*, vol. 93, no. 1, p. 14801, 2004.
- [37] S. J. Langendorf, “Effects of Electron Emission on Plasma Sheaths,” Ph.D Dissertation, Daniel Guggenheim School of Aerospace Engineering, Georgia Institute of Technology, Atlanta, GA, 2015.
- [38] M. Ye *et al.*, “Suppression of secondary electron yield by micro-porous array structure,” *Journal of Applied Physics*, vol. 113, no. 7, p. 74904, 2013.

CHAPTER 5

EFFECT OF DEBYE-SCALE SURFACE FEATURES ON SPACE CHARGE SATURATION OF PLASMA SHEATHS

5.1 - ABSTRACT

Previous experimentation into Hall effect thruster discovered millimeter length scale erosion channels evolving in the ceramic chamber wall near the end of the thruster lifetime. A series of grooved hexagonal boron nitride (hBN) surfaces with different aspect ratios, designed to mimic simplified versions of the erosion channels, were exposed to an argon plasma. The change in the plasma sheath characteristics, particularly the ‘collapse voltage’ which occurs when the discharge voltage is sufficient to produce enough secondary electrons to collapse the sheath, was 44% and 89% higher for a 1 mm and 5 mm grooved depth, respectively as compared to a planar surface. A ray-trace optical model for secondary electron emission reduction with a one-dimensional kinetic model for the plasma was used to simulate the responses. With increased groove depth, this simple model was inadequate to capture the correct collapse voltage, which is attributed to a variation of electron and ion charge densities near the groove entrance. These results provide insights into how larger length scale surface topology features, on the order of the Debye length, influence the dynamic interactions between a surface and plasma sheath.

5.2 - INTRODUCTION

Hall effect thrusters (HETs) are plasma-based electric propulsion devices used in low thrust, high impulse applications such as those for geosynchronous satellite station keeping [1]. In the HET design, a magnetic field is used to trap electrons in a closed azimuthal drift that concentrates the electric field of a direct current (DC) discharge to accelerate propellant ions. The ions accelerate through a quasi-neutral plasma region that contains both ions and electrons. Thus, the thrust density is not influenced by the space charge limit. A representative diagram and in-service photo of a HET is shown in Figure 5.1.

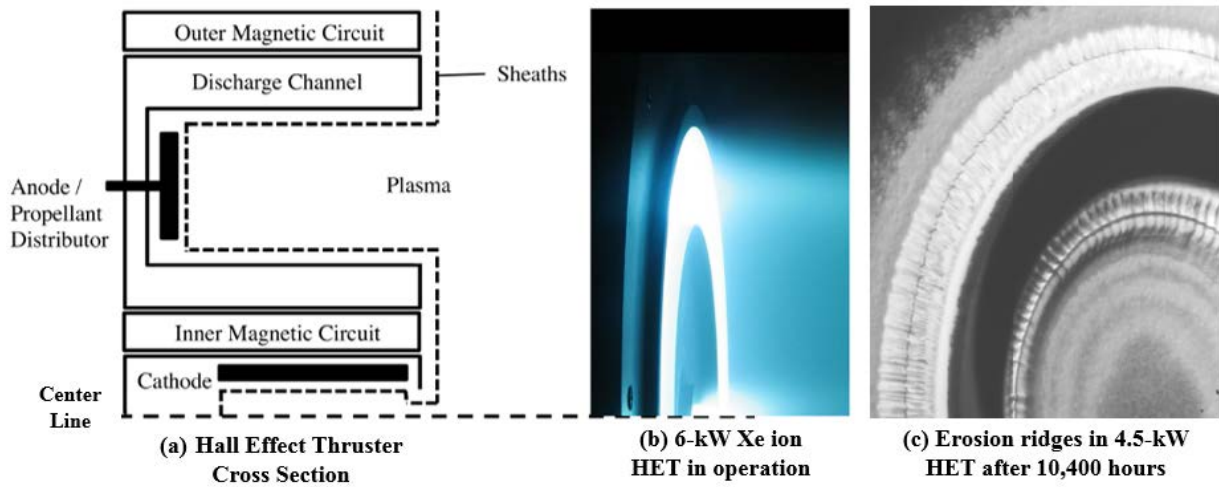


Figure 5.1 - Schematic and photos of Hall Effect Thrusters

In the development of HETs, plasma-wall interactions have been found to play a key role in the thruster operation and performance [2]–[4]. With ion and electron movement in the plasma region, their impact into the thruster wall and electrodes creates heat, material erosion, and a loss of thruster efficiency. In addition, space charge saturation of the plasma sheath can form along the discharge channel wall and contribute to electric field oscillations and anomalously high levels of electron transport to the thruster anode [5]. Since these impacts are continuous and related to the plasma density, the surface wall morphology will evolve during service creating a dynamic

plasma-wall interaction. Burton *et al.* have reported on sub- and near sub-micron erosion patterns in a hexagonal boron nitride (hBN) - amorphous silica (SiO₂) HET wall material exposed to a krypton plasma [6]. A variety of jagged protrusions were noted as well as smooth planar surfaces created from the exfoliation of entire grains from stress created by the anisotropic thermal expansion of hBN. Such surface features, and their accompanying surface area, will modify the secondary electron emission (SEE) yield from the wall and thus influence the plasma sheath stability.

SEE from the discharge channel wall has been found to have a significant effect on power efficiency and bulk plasma electron temperatures in HETs [7]–[9]. It has been reported that significant levels of SEE from the HET channel walls can lead to dramatic drops in the magnitude of the sheath potential as these emitted electrons neutralize the ion-rich sheath. This situation is sometimes referred to as a “space-charge-saturation” of the sheath [10],[11]. These differences are suspected to depend upon the length scale of the surface structure. Langendorf and Walker [7], using different metallographically-polished hBN surface finishes, noted these changes in the plasma sheath potential if the surface was smooth or rough. The length scale of these metallographically-polished surface topologies was on the order of tens of microns dependent on the polishing grit paper. For a HET that has a high plasma density and a thin plasma sheath on the order of tens of microns, even a ‘smooth’ wall can appear ‘rough’ creating dissimilarities in the near surface plasma characteristics [7]. If the chamber wall is exposed to the discharge plasma for an extensive time, radially-symmetric surface modulations, at a larger characteristic length scale than the plasma sheath thickness, have been observed and are shown in Figure 5.1(c) [12]. In the effort here, we have extended the prior work of Langendorf and Walker [7] to address plasma-material interactions that are at larger length scale modulations (orders of millimeters) on the

material surface. Though such large length scale surface topologies in HET thruster walls can take thousands of hours of operation to form (Figure 5.1(c)), quantifying their effect on the plasma sheath is essential for predicting HET efficiency and long term behavior [7],[13],[14].

One of the challenges in investigating plasma-wall interactions and discharge channel plasma sheaths is the need to make measurements *in situ*. For a thruster, this poses a significant challenge because of its high plasma density and tens of microns sheath spacing. However, due to the scalability and dimensionless formulation of sheath theories [15]–[17], it is feasible to examine the physics in a nominal plasma environment with a lower plasma density. By creating surface features at the Debye length of lower density plasma, on the millimeter length scale, we can use a Langmuir probe to measure the sheath behavior between the different topologies. Effects of surface features smaller-than-Debye length scales on SEE were previously investigated [13],[18] and found to be consistent with a trapping of the secondary electrons near the wall surface. How such behavior may be altered at the more macroscopic length scale created by a coarser topology is the subject of this work. By quantifying this length scale behavior, we will be able to elucidate how the plasma sheath behaves near these coarser variations in the discharge channel wall and how current theories are able to capture the physics of this interaction.

5.3 - EXPERIMENTAL SETUP

5.3.1 - PLASMA DEVICE

The plasma used in this study was non-Maxwellian with a significant fraction of energetic primary electrons that intentionally stimulated SEE from our modified surfaces. By varying the energy of the primary electrons, we were able to determine the critical energy at which the emitted electron density is sufficient to neutralize and/or saturate the sheath, creating the collapse voltage transition. This plasma was generated in a low-density multi-dipole plasma cell lined with

permanent magnets that created confining cusp fields, as shown in the diagram of Figure 5.2. These cusp magnetic fields decay rapidly away from the permanent magnet dipoles around the boundary, so the main plasma volume of the device is not magnetized. The cell was cylindrical in shape and had a radius of 30.5 cm and a height of 91 cm with the cell walls being aluminum and grounded. Typical plasma densities used were approximately 10^{13} m^{-3} at an electron temperature of 3 eV with a 1-10% energetic electron population.

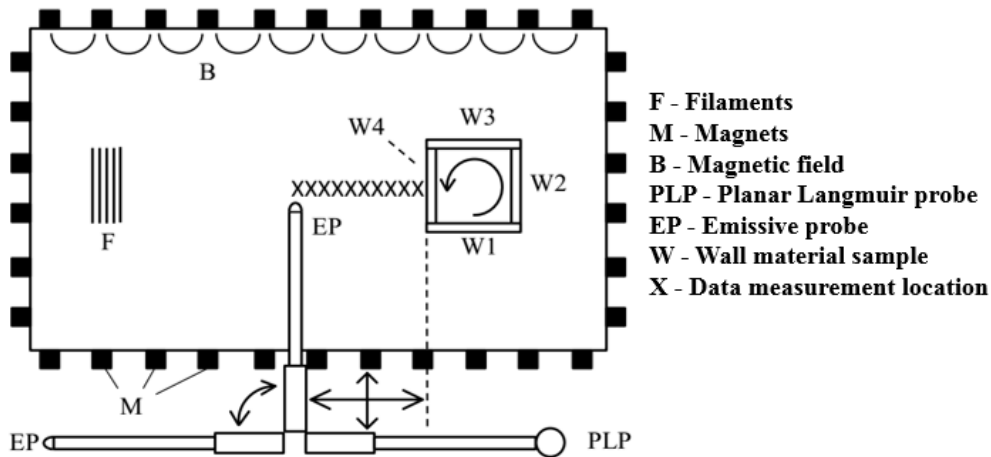


Figure 5.2 - Diagram of plasma cell and diagnostics. Not to scale.

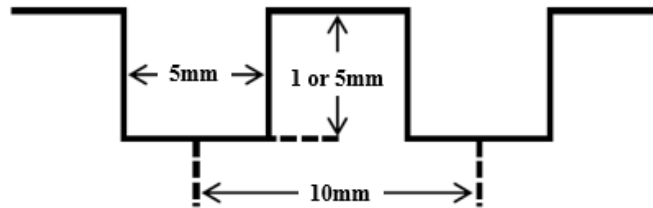
The plasma was generated by collisional ionization of ultra-high purity (UHP) 99.999% argon gas with energetic electrons emitted from thoriated-tungsten filaments positioned inside the cell. The electrons are accelerated into the sample by application of the discharge voltage (between -60 V to -175 V) between the filaments and the device frame. The Debye length for the plasma under these conditions was calculated from probe measurements to be between 3 mm and 5 mm for the lower discharge voltages and higher discharge voltages respectively. The plasma cell is housed in a large vacuum chamber which achieved a base pressure of $\sim 1 \times 10^{-8}$ Torr [19]. During operation, 500 standard cubic centimeter (sccm) of UHP argon was flowed into the chamber using a MKS 1179A01352CS1BV mass flow controller to achieve the experimental pressure of $\sim 1 \times 10^{-4}$ Torr.

5.3.2 - WALL MATERIAL SAMPLES

Disks were made from the dielectric materials of hBN that measured 7.6 cm in diameter and 0.64 cm in thickness. This material has a large SEE coefficient due to the electron bombardment which increases with the energy of incident electrons. It is also a commonly used ceramic chamber wall material in HETs. The purity grade of the hBN was AX05 (99.9%). Five (5) mm wide grooves were machined into the surface of the disks, Fig. 3(a)-(b), which were spaced 10 mm apart with uniform depths of either 1 mm or 5 mm, Fig. 3(c). A control disk with no grooves was also used for comparison. Prior to insertion into the plasma chamber, the disks were cleaned with acetone, deionized water then air dried. The hBN disks were mounted to a box holder made of stainless steel.



(a) hBN disks prior to experiment



(b) Diagram of grooves with important geometries labeled

Figure 5.3 - hBN disks with machined grooves of geometries shown in the diagram

5.3.3 - DIAGNOSTICS

The sheath potential over the wall material samples was measured using an emissive probe constructed of telescoping alumina tubing and a hairpin 0.127 mm diameter thoriated tungsten filament tip. The emissive probe is biased with a Keithley 2410 Sourcemeter. Bulk plasma

parameters were measured using a planar Langmuir probe positioned in the center of the plasma device. The probe was cleaned by ion bombardment at 500 V bias for a period of 15 min before data collection; the probe was re-cleaned at 500 V for 30 s after the collection of each trace. The Langmuir probe body was constructed of alumina tubing. The tip was made from 0.5-mm thick tungsten foil cut into a 7.70 mm diameter circle. Five linear stair sweeps from -200 to 0 V were collected with an average dwell time of 20 ms at each voltage at a step interval of 0.2 V. The probe characteristics were corrected for singly-charged argon ion- and electron-induced SEE using data for tungsten from reference [20].

5.3.4 - COMPUTATIONAL METHODS

Since the grooves will provide a modulated surface topology for SEE, which will impact the plasma sheath, modeling these electron trajectories from such features were undertaken and forward fed to plasma models to simulate the sheath behavior. These simulations were then compared to the experimental characterization of the sheath to gain insights into the potential mechanisms that govern plasma characteristics over such macroscopic topological features.

5.3.5 - OPTICAL MODEL FOR SECONDARY ELECTRON TRAPPING

The optical obstruction model is based on a defined geometry which can result in electron trapping. This model assumed electrons are diffusely emitted from the surface and followed an unperturbed ray trajectory. If these electrons intersect a surface feature, they are unable to ‘emit’ from the material and are considered trapped. Hence this model is independent of material type but dependent on surface topology. The groove height (h) divided by the groove width (w) is referred to as the aspect ratio (AR). The view factor expressions are then defined in terms of AR as the following:

$$F_{\frac{ES}{SE}} = \sqrt{(1 + AR^2)} - AR \quad (\text{Eq. 5.1})$$

$$F_{EB} = \frac{1+AR-\sqrt{(1+AR^2)}}{2} \quad (\text{Eq. 5.2})$$

where $F_{ES/SE}$, is the view factor expression for an infinite strip adjoining another strip at a 90° angle and where F_{EB} is the view factor expression for two strips separated by a given width, these form the geometric construction of the grooves as shown schematically in Figure 5.4(a)

The overall reduction in SEE, which is denoted as the ratio of emission, γ , normalized by the nominal emission from a smooth or non-grooved surface, γ_o , was constructed from the view factor equations above and given as:

$$\frac{\gamma_{groove}}{\gamma_o} = F_{EB}^2 + 2F_{ES} \times F_{ES} \quad (\text{Eq. 5.3})$$

where F_{EB} is the contribution from the bottom of the groove, Eq. (5.2), and F_{ES} and F_{SE} are the emission contributions from the two side walls in the groove, Eq. (5.1). The nominal emission, γ_o , was referenced from a smooth surface (no grooves) and assumed to be a constant. Note that Eq. (5.3) only accounts for the aspect ratio and does not account for the groove ratio. To incorporate the groove ratio (GR), which is the groove spacing (s in Figure 5.4(a)), divided by the groove width, the SEE emission ratio becomes

$$\frac{\gamma}{\gamma_o} = GR \left(\frac{\gamma_{groove}}{\gamma_o} \right) + (1 - GR) \quad (\text{Eq. 5.4})$$

The resulting effective SEE yield (γ/γ_o) curves for a set of grooved ratios are plotted as a function of the aspect ratio in Figure 5.4(b). Using this plot we note that at high aspect ratios (deep grooves), very few straight-line paths are available for the electrons to escape the groove. However, at high groove ratios (bottom curve in Figure 5.4(b)), the density of grooves to trap electrons greatly increases. While at an equal aspect ratio, the effective SEE yield decreased by nearly 70% as compared to a smooth surface, i.e. an aspect ratio of zero. With a decreasing groove

ratio, which means either the groove width increased or the groove spatial wavelength decreased, the effective SEE yield will increase.

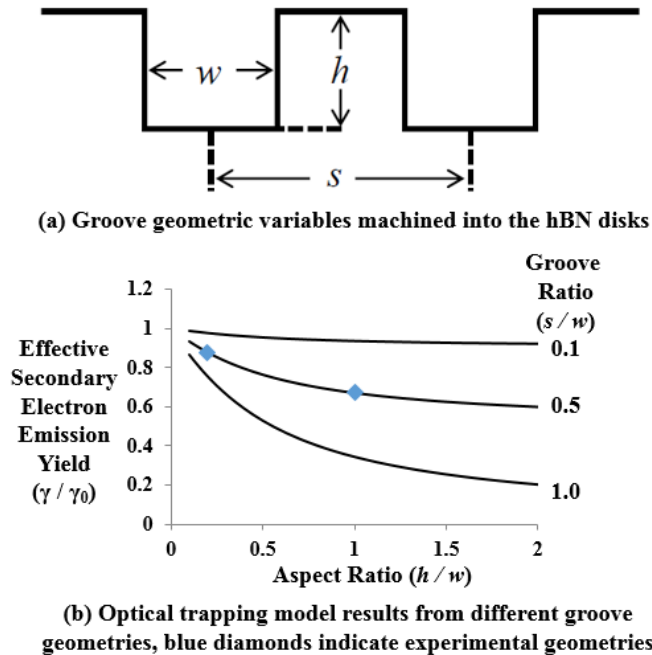


Figure 5.4 - (a) Geometric grooves variables and results of the optical trapping model

The experimental geometries studied are indicated by the diamond markers on Figure 5.4(b). For the $h = 1$ mm groove sample with an aspect ratio = 0.2 and a spacing ratio = 0.5, a SEE reduction factor of ~ 0.87 is expected. While the $h = 5$ mm groove sample with an aspect ratio = 1.0 and groove ratio = 0.5 will result in a SEE reduction factor of ~ 0.67 . Having obtained an estimate of SEE reduction because of surface topology, i.e. the grooved topology, the γ/γ_0 values from Eq. 5.4 were incorporated into an analytical one dimensional plasma kinetic sheath model to obtain predicted SEE which was compared to the experimental results, Figure 5.5(b) described in the results section.

5.3.6 - KINETIC MODEL FOR APPROXIMATION OF REDUCED SEE

In our kinetic models, the plasma was described by the system of equations that included the Boltzmann equations for electron and ion distribution functions, Poisson's equation for electrical potential and the currents balance equation for the floating potential of emissive plate. These generic equations can be found in reference [13],[21]. In the first model, referred to as the 'collapse voltage model,' a simplified 1D construction of the plasma sheath was undertaken for a truncated geometry which was based on the classical model by Hobbs and Wesson [10] with the inclusion of the kinetic considerations as developed by Sheehan [22]. This allowed for the analysis of the sheath collapse at a wide variety of groove geometries and primary electron energy levels without significant computational expense. However, we only considered the 1D directional flow of plasma ions and electrons into the sheath and their impact on the wall as well as secondary electrons emitted from the wall returning back to the plasma. The distribution functions for the bulk plasma electrons (Maxwellian at sheath entrance), secondary electrons (half Maxwellian emitted from wall), and energetic primary electrons emitted from the discharge filament (isotropic mono-energetic at the sheath entrance) were computed. The energy levels of the electrons and ions for this simulation were $T_e = 3$ eV and $T_i = 0$ eV, respectively. The floating wall potential was solved to enforce the current balance condition and the electric field and potential in the sheath which was determined to be self-consistent from the spatial densities of the charged-particle populations. The SEE yield of the wall was calculated from a user-specified curve of total SEE yield versus incident electron energy. This energy-dependent SEE yield was integrated across the incident electron distributions at the wall and was multiplied by the γ/γ_0 value (given above in section III.A) approximating the influence of the grooves on SEE. This enabled the study of the sheath collapse phenomena of interest. . A more detailed description of the 1D sheath model is

given in reference [7] with further information concerning the derivations of the optical and kinetic models found in reference [21].

The second model is a full simulation of the plasma where the sheath is allowed to form simply because of the near surface boundary conditions. From this simulation, distributions of charge and potential changes can be created albeit at the expense for one set of geometries and primary electron energy level. To model these surface interactions, a Particle-In-Cell (PIC) Monte Carlo Collisions (MCC) method was employed. The PIC model was two-dimensional in space (2D) and three-dimensional in terms of electron and ion velocity (3V). The distribution functions for the electrons and ions were found from the Boltzmann equations given as

$$\frac{\partial f_e}{\partial t} + \vec{v}_e \frac{\partial f_e}{\partial \vec{r}} - \frac{e\vec{E}}{m} \frac{\partial f_e}{\partial \vec{v}_e} = J_e, \quad n_e = \int f_e d\vec{v}_e, \quad (\text{Eq. 5.5})$$

$$\frac{\partial f_i}{\partial t} + \vec{v}_i \frac{\partial f_i}{\partial \vec{r}} + \frac{e\vec{E}}{M} \frac{\partial f_i}{\partial \vec{v}_i} = J_i, \quad n_i = \int f_i d\vec{v}_i, \quad (\text{Eq. 5.6})$$

where v_e , v_i , n_e , n_i , m , and M are the electron and ion velocities, concentrations, and masses, respectively; J_e and J_i are the collisional integrals for electrons and ions with background atoms. Knowing the distribution functions for these electrons and ions, the mean energy of charged species was calculated along with their concentrations, and elastic and non-elastic collisional rates and assumed a zero-current balance into the surface of the floating emissive plate. The floating potential of the emissive plate was calculated to be self-consistent from the condition of a zero total current into the hBN plate surface using Poisson's equation describing the electric potential distribution.

Since the discharge operated in argon, the kinetics of electrons included elastic scattering of electrons on background atoms, excitation of metastable states, and ionization. For ions we took

into account the elastic and resonant charge exchange collisions. The SEE coefficient is calculated by accounting for the energy distribution functions of the electrons approaching the plate surface. Since we are most interested in the grooved feature, the PIC simulations for the plasma was only near these features with a calculated domain size of 7 cm x 5 cm with the plate having a diameter of 55 mm with four 5 x 5 mm grooves on its surface.

The grooved boundary conditions were referred to a domain embedded in unlimited quasi-neutral plasma with Maxwellian electrons and ions at the temperatures $T_e = 3$ eV and $T_i = 0.026$ eV, respectively for PIC. Additionally, a mono-energetic electron beam entered the calculation domain from the bottom boundary so that the electron component of the plasma consisted of a Maxwellian part and beam electrons. The electron and ion fluxes at the boundaries were constant with the electrical potential being that of a quasi-neutral plasma. The floating potential was calculated separately inside of the groove for the side walls and the bottom taking into account both the fluxes of electrons and ions from the plasma and the secondary electrons. All of the equations were then self-consistently solved using the PlasmaNov code for the PIC described in full detail in reference [13] for a primary electron beam energy of 70 eV and a plasma density in the quasi-neutral region of 2×10^8 cm⁻³.

5.4 - RESULTS AND DISCUSSION

From the data shown in Figure 5.5(a), the discharge voltage at which the plasma sheath above the sample collapsed is denoted by the arrows and will be referred to as the ‘collapse voltage’ for the remainder of the paper. The hBN samples revealed some reduction in the effective SEE from the wall for both types of grooved surfaces. This can be seen by the increase in the collapsed voltage which resulted in the decrease in the SEE as compared to the planar surface. Specifically, the collapse voltage increased by 44% and 89% for the 1 mm and 5 mm grooved

samples, respectively. The sheath collapses when there is a sufficient number of secondary electrons to neutralize the potential barrier of the wall [10]. From these experimental results, it is clear that macroscopic grooving, on the same size scale or larger than the Debye length of the plasma, will reduce SEE requiring increased plasma energies or temperatures to collapse the sheath.

The γ/γ_0 ratio in Figure 5.5(b) represents the SEE reduction caused by the different grooved features, with $\gamma/\gamma_0 = 1$ being the planar surface, $\gamma/\gamma_0 = 0.87$ being the 1-mm groove and $\gamma/\gamma_0 = 0.67$ being the 5-mm groove, as calculated from Eqs. (5.1 - 5.4).

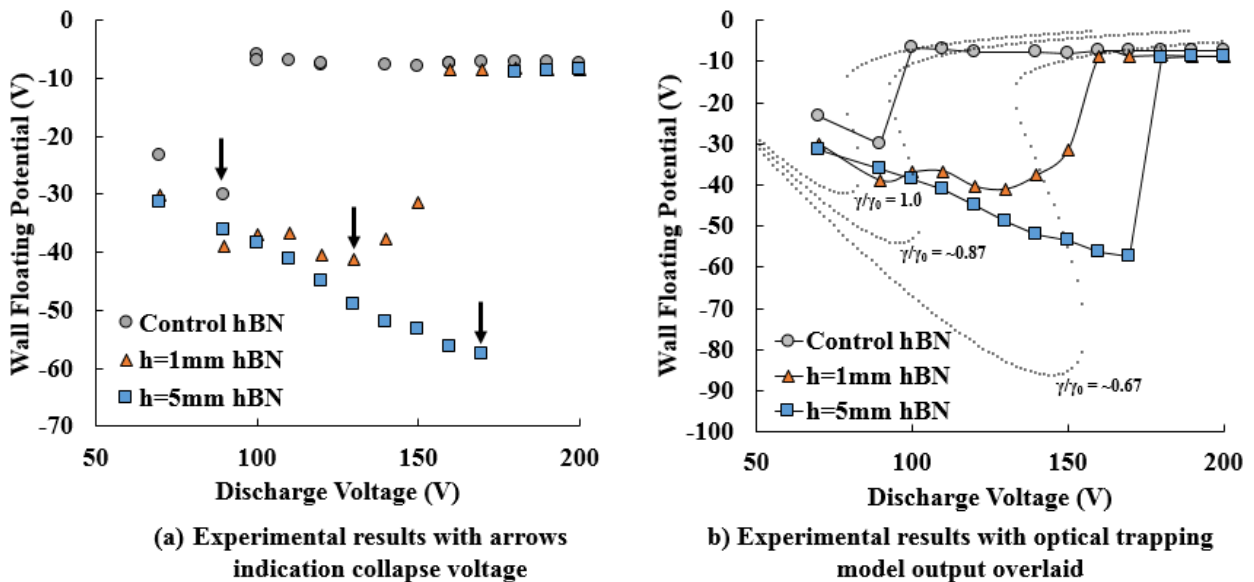


Figure 5.5 - Plots of the floating wall potential vs. discharge voltage

Figure 5.5(b) is a plot of the experimental data from Figure 5.5(a) overlaid with the predicted curves based on both geometry and one dimensional plasma kinetics. The control surface showed relatively good agreement with the simple kinetic model's ideal planar surface ($\gamma/\gamma_0 = 1.0$) as both the prediction and experimental values followed a similar sheath potential curve and had approximately similar collapse voltages near 80 V. The postponement of the increased collapse voltage for the $h = 5$ mm sample was ~ 175 V with the prediction at ~ 150 V. For the $h = 1$ mm

sample, an even higher discrepancy between the experimental collapse voltage of ~ 150 V was found as compared to the predicted ~ 100 V. In addition, for the $h = 1$ mm grooves, the experimental data suggested a more gradual transition between a stable and unstable sheath condition. This is noted by the relatively smooth increase in the experimentally-measured sheath potential versus discharge potential. Upon grooving the samples, the simple one-dimensional kinetic model appeared to be insufficient in capturing the physics of the experimentally measured response.

For the planar surface, the assumptions of linear electron trajectories and constant electron temperature and electron and ion densities appear sufficient to explain the collapse voltage conditions. Similarly, the general trend for collapse voltage increasing with a deeper groove was predicted. This can be rationalized that for a deeply-grooved sample, where one could assume that the electron density will be lower deeper into the groove. For example, electron emission that is not normal to the surface will likely collide and be absorbed by the side walls. This would result in a lower number of emitted electrons from regions deeper in the grooves and hence a higher discharge voltage as shown. For the electrons that do emit from the groove, they are likely to be more normal to the surface as they have had to navigate through a high aspect ratio feature to reach the free surface. This may explain why the deeper groove (similar to the planar surface) showed similar sheath potential curve behavior. In contrast, a shallower groove would be able to have more electrons escape and emit at a distribution of angles from the groove, which could have created the conditions for a gradual collapse.

To quantify the dependence of electron density with grooved feature, Figure 5.6(a) is the electron density distribution over the emissive grooved surface for the $h = 5$ mm or deep groove geometry. The numbers 1, 2, 3, and 4 in Figure 5.6(a) represent separated areas for the floating

potential calculation. From this distribution map, it is seen that an accumulation of secondary electrons exists near the groove entrance, whereas the electron density is much lower within the sheath. The electrons appear to preferentially concentrate at the groove entrance because of the electrostatic forces from the nearby floating walls and their overlapping semi-sheaths. This concentration of electrons, as it related to groove geometry, likely contributes to the deviations from the predicted one-dimensional model noted above. The distribution of potential, measured in volts, over the same grooved hBN surface, Figure 5.6(b), clearly shows that as the groove deepened, a substantially lower potential formed as compared to anywhere else on the surface of the sample.

By drawing electrons into the lower potential grooves, the surrounding sheath potential reduced. Hence, from these findings, it is possible that at geometries that are a specific fraction of the Debye length, large changes in the electron densities will be found. If similar electron densities develop in Debye-scale surface depressions in HET channels, they could focus ions into the depressions and thus contribute to the growth of the anomalous large-scale erosion ridges observed in some HET lifetime tests, though further work is needed to concretely confirm this effect or its contribution to deep groove erosion patterning [14].

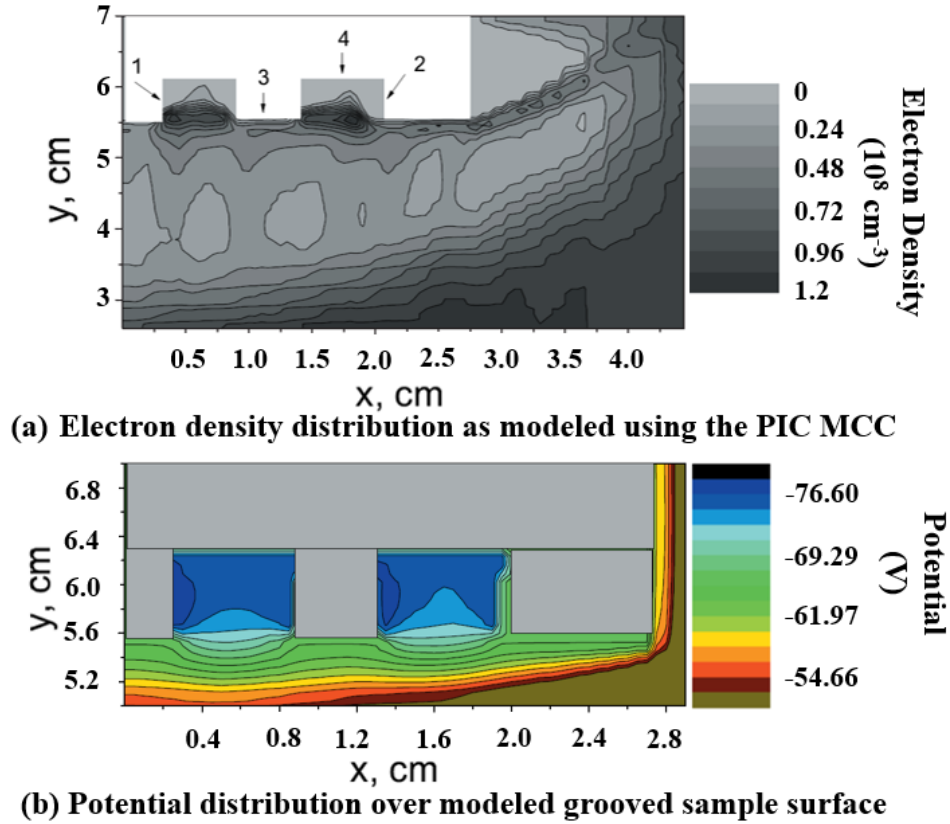


Figure 5.6 - The distributions resulting from the PIC-MCC modeling

5.5 - CONCLUSIONS

In this work we have compared experimental results with a models of electron trapping from hBN surface grooves that were similar to the Debye length of a plasma. The results confirmed that the space-charge saturation of the plasma sheath over a grooved surface was dependent on the size of these geometric grooves. Using a one-dimensional optical model for electron trapping with a plasma kinetic model, reasonably agreement in the prediction of the collapse voltage for a planar surface was found between the experiment and model. When the surface was grooved, some discrepancies between the model predictions and the experimental findings, particularly for the shallowest grooves ($h = 1$ mm), were noted. This breakdown in the one-dimensional model is believed to be a result of the complex interactions of electron densities near the grooved entrances, which was quantified through a PIC-MCC simulation. These findings confirm that changes in

plasma sheath stability will occur for surfaces whose features sizes evolve at these Debye length scales. These results suggest that larger scale features may also need to be considered in HET plasma models where similar surface structures are noted to develop from plasma induced erosion.

AUTHORS AND ACKNOWLEDGEMENTS

Thomas S. Burton^a, Samuel Langendorf^b, Mitchell L. R. Walker^b, Irina Schweigert^c, Michael Keidar^c, and Gregory B. Thompson^{a*}

a. Department of Metallurgical and Materials Engineering, University of Alabama, Tuscaloosa, AL, USA.

b. School of Aerospace Engineering, Georgia Institute of Technology, Atlanta, Georgia, USA.

c. Mechanical and Aerospace Engineering Department, George Washington University, Washington, DC, USA.

**Contact author: gthompson@eng.ua.edu*

The authors gratefully thank grant AFOSR-FA9550-11-1-0160 for supporting this work.

5.6 - REFERENCES

- [1] Oh, D. Y., Randolph, T., Kimbrel, S., and Martinez-Sanchez, M., “End-to-End Optimization of Chemical-Electric Orbit-Raising Missions,” *Journal of Spacecraft and Rockets*, Vol. 41, Sep. 2004, pp. 831–839, doi: 10.2514/1.13096.
- [2] De Grys, K., Mathers, A., Welander, B., and Khayms, V., “Demonstration of 10,400 Hours of Operation on 4.5 kW Qualification Model Hall Thruster,” Nashville, TN: 2010, pp. 1–10.
- [3] Gascon, N., Dudeck, M., and Barral, S., “Wall Material Effects in Stationary Plasma Thrusters. I. Parametric Studies of an SPT-100,” *Physics of Plasmas*, Vol. 10, 2003, p. 4123, doi: 10.1063/1.1611880.
- [4] Barral, S., Makowski, K., Peradzyński, Z., Gascon, N., and Dudeck, M., “Wall Material Effects in Stationary Plasma Thrusters. II. Near-Wall and in-Wall Conductivity,” *Physics of Plasmas*, Vol. 10, 2003, p. 4137, doi: 10.1063/1.1611881.
- [5] Morozov, A., and Savel’Ev, V., “Theory of the near-Wall Conductivity,” *Plasma Physics Reports*, Vol. 27, 2001, pp. 570–575.

- [6] Burton, T., Schinder, A. M., Capuano, G., Rimoli, J. J., Walker, M. L., and Thompson, G. B., “Plasma-Induced Erosion on Ceramic Wall Structures in Hall-Effect Thrusters,” *Journal of Propulsion and Power*, Vol. 30, Mar. 2014, pp. 690–695, doi: 10.2514/1.B34882.
- [7] Langendorf, S., and Walker, M., “Effect of Secondary Electron Emission on the Plasma Sheath,” *Physics of Plasmas (1994-present)*, Vol. 22, Mar. 2015, p. 033515(1-8), doi: 10.1063/1.4914854.
- [8] Barral, S., Jayet, Y., Mazouffre, S., Dudeck, M., Véron, E., and Echegut, P., “Hall Effect Thruster with an AlN Discharge Channel,” Princeton, NJ: 2005, pp. 1–7.
- [9] Lawless, J., and Subramaniam, V., “Theory of Onset in Magnetoplasmadynamic Thrusters,” *Journal of Propulsion and Power*, Vol. 3, Apr. 1987, pp. 121–127, doi: 10.2514/3.22963.
- [10] Hobbs, G., and Wesson, J., “Heat Flow through a Langmuir Sheath in the Presence of Electron Emission,” *Plasma Physics*, Vol. 9, 1967, pp. 85–87.
- [11] Goebel, D. M., and Katz, I., *Fundamentals of Electric Propulsion: Ion and Hall Thrusters*, John Wiley & Sons, 2008.
- [12] Hofer, R. R., Mikellides, I. G., Katz, I., and Goebel, D. M., “BPT-4000 Hall Thruster Discharge Chamber Erosion Model Comparison with Qualification Life Test Data,” *30th International Electric Propulsion Conference*, 2007, pp. 17–20.
- [13] Schweigert, I., Langendorf, S., Walker, M., and Keidar, M., “Plasma-Wall Interaction Controlled by Secondary Electron Emission,” Hyogo-Kobe, Japan: 2015, pp. 1–10.
- [14] Schinder, A. M., Walker, M., and Rimoli, J. J., “Three-Dimensional Model for Erosion of a Hall-Effect Thruster Discharge Channel Wall,” *Journal of Propulsion and Power*, Vol. 30, May 2014, pp. 1373–1382, doi: 10.2514/1.B35098.
- [15] Chodura, R., “Plasma-wall Transition in an Oblique Magnetic Field,” *Physics of Fluids (1958-1988)*, Vol. 25, 1982, pp. 1628–1633, doi: 10.1063/1.863955.
- [16] Oksuz, L., and Hershkowitz, N., “Plasma, Presheath, Collisional Sheath and Collisionless Sheath Potential Profiles in Weakly Ionized, Weakly Collisional Plasma,” *Plasma Sources Science and Technology*, Vol. 14, Feb. 2005, pp. 201–208, doi: 10.1088/0963-0252/14/1/022.
- [17] Kim, G.-H., Hershkowitz, N., Diebold, D., and Cho, M.-H., “Magnetic and Collisional Effects on Presheaths,” *Physics of Plasmas (1994-present)*, Vol. 2, Mar. 1995, pp. 3222–3233, doi: 10.1063/1.871153.

- [18] Raitses, Y., Staack, D., Dunaevsky, A., and Fisch, N., "Operation of a Segmented Hall Thruster with Low-Sputtering Carbon-Velvet Electrodes," *Journal of Applied Physics*, Vol. 99, Dec. 2006, p. 36103(1-3), doi: 10.1063/1.2168023.
- [19] Langendorf, S., and Walker, M., "Hysteresis and Mode Transitions in Plasma Sheath Collapse due to Secondary Electron Emission," *Journal of Applied Physics*, Vol. 119, Mar. 2016, p. 113305(1-5), doi: 10.1063/1.4943778.
- [20] Sheehan, J., and Hershkowitz, N., "Emissive Probes," *Plasma Sources Science and Technology*, Vol. 20, Nov. 2011, p. 063001(1-22), doi: 10.1088/0963-0252/20/6/063001.
- [21] Langendorf, S. J., "Effects of Electron Emission on Plasma Sheaths," Ph.D Dissertation, Daniel Guggenheim School of Aerospace Engineering, Georgia Institute of Technology, 2015.
- [22] Sheehan, J., Kaganovich, I., Wang, H., Sydorenko, D., Raitses, Y., and Hershkowitz, N., "Effects of Emitted Electron Temperature on the Plasma Sheath," *Physics of Plasmas* (1994-present), Vol. 21, Jun. 2014, p. 063502(1-7), doi: 10.1063/1.4882260.

CHAPTER 6

INFLUENCE OF BORON ADDITIONS TO LaB_6 'S WORK FUNCTION AND MICROSTRUCTURE IN VACUUM PLASMA SPRAYED COATINGS

6.1 - ABSTRACT

A series of LaB_6 powder mixtures with excess boron additions of either 0, 5 or 10 vol.% were vacuum plasma sprayed (VPS) as coatings. Typical to VPS, a splat-like microstructure was found in the deposit with the densification significantly enhanced with the 5 and 10 vol.% B additions. All deposited LaB_6 adopted the cubic structure. The improved densification is explained in terms of the excess boron reacting with background contaminants. Though the coating was able to be deposited onto the stainless steel substrate under the first pass, subsequent layering of the LaB_6 proved difficult indicating potential self-adhesion issues under the processing conditions studied. The work function of the coatings were measured and found to range 4.20 eV to 4.45 eV, with the lowest work function for the denser coatings.

6.2 - INTRODUCTION

Vacuum plasma spraying (VPS) is a thermal spraying technique wherein a base material powder is fed into a plasma flow. This melts the powder and imparts a large force which drives the material droplets onto a substrate [1]. These molten droplets then solidify on the substrate's surface from which continued application allows for coatings and/or monolithic parts to be built. The use of the plasma arc enables VPS to deposit high melting temperature materials, such as tungsten [2], tantalum carbides [3], and other types of complex ceramic compositions. Another benefit of VPS is the low-pressure environment which can reduce deleterious interactions of the molten spray with such species like oxygen, nitrogen, or carbon. In addition, VPS is an additive

form of fabrication enabling complex and near net shape features to be constructed which may not be possible through traditional casting or subtractive (machining) methods.

Lanthanum hexaboride (LaB_6) is best known as a thermionic emission material that is capable of producing a large, stable current of electrons when heated to high temperatures. In addition, the material exhibits excellent vacuum stability, resistant to poisoning in a variety of atmospheres, as well as resistance to oxidation and corrosion in acidic environments, exhibits a high hardness with reasonable thermal and electrical conductivity properties [4], [5]. Consequently, it has found diverse applications as an electron cathode for plasma sources, optical coaters, arc melters, ion platers, ion sources, refining additions for intermetallics [6], and electron sources for microscopes [7]–[10]. Of these applications, LaB_6 is most commonly used as an electron emission source (which is a surface dominated effect [11]). Consequently, technologies that pursue LaB_6 as a film or coating are ideal [12].

Prior reports have shown that LaB_6 can be deposited as a film or coating through various physical vapor deposition (PVD) methods [13]. Yet, to the authors' knowledge, there has not been a comparative growth of this ceramic by VPS, even though boron carbide and metal boride coatings have been successfully deposited [14]–[18]. VPS can be advantageous in comparison to other PVD methods in that it can provide much more rapid growth rates on the order of microns per pass of the plasma torch. Nevertheless, the deposited VPS microstructure, often referred to as a splat structure, can compose of recrystallized grains, chemical partitioning from the decomposition of the powder constituents during spraying, and varied porosity and grain sizes [16], all of which can affect the properties of the coating.

In this effort, we aim to determine if LaB_6 can be successfully deposited by VPS as another alternative to other PVD methods. And if successfully deposited as a coating, to what

extent does the as-deposited microstructure influence the work function of LaB₆. As part of this study, various boron amounts were added to the initial LaB₆ powder mixture prior to spraying. These additions were done to potentially offset any loss of boron in the LaB₆ from the high temperature and low pressures of VPS conditions, as previously observed with carbon in carbides [19], [20], silicon in silicides [21], nitrogen in nitrides [22], and so forth. This is particularly important as the LaB₆ stoichiometry has been shown to be very sensitive to the La:B content [11]. Another potential advantage of excess boron in the initial spray deposit is that it could serve as an internal reservoir within the coating to offset boron losses that occur over extended emission. D. Goeble *et al.* has reported that the stoichiometry of LaB₆ does indeed deplete in boron with continuous, long term emission which consequently effects the stability of the material as a stable emission source for a variety of applications [9].

6.3 - EXPERIMENTAL SETUP

Three 304 stainless steel substrates were cut from bar stock into approximately 51 mm x 51 mm x 6 mm plates with each plates' edges beveled and the surface polished using 500 grit SiC. The stainless steel was chosen for its chemical stability, ductility, and low magnetic permeability. Prior to deposition, the plates were cleaned with hot water and dish soap, followed by acetone rinse, with a final water rinse and then baked-out at 350 °C furnace for one hour.

The LaB₆ powder was acquired from Materion Corporation at 99.5% purity and a particle size between 5-10 μm [23]. The LaB₆ powder was separated into three separate batches whereupon amorphous elemental boron powder, acquired from SB Boron at 95% purity [24], was added such that the batches contained the following added boron mixtures: 0% (no added boron), 5 vol.% added boron, and 10 vol.% added boron. The powders were then agglomerated using ethanol and polyvinyl butyral resin (PVB)[25] and subsequently sieved to 15 - 45 μm

using a 325 mesh screen. These steps were done to enhance flow-ability of the powder through the plasma gun's plumbing during the VPS process.

The VPS chamber was evacuated prior to spraying to a pressure of 10 Pa and backfilled with Ar to 26.6 kPa. The powder was then brought into the plasma gun using a 70-to-1 volume mixture of Ar:H₂ as the carrier gas. The powder and carrier gas entered the VPS tungsten cathode plasma gun at an operating powder setting of 40 kW. The substrates were mounted with the 51 mm x 51 mm surface normal to the plasma arc which was directly pointed down at the substrate at a standoff distance of approximately 76 mm. The substrate was then rastered under the plasma arc at a speed of 1 m/min per pass.

Post-deposition, the coating's top and cross-sectional viewing directions were prepared for scanning electron microscopy (SEM) imaging in a JOEL 7000 that was operated at 30 keV at a probe current of 1.7×10^{-10} A. Though the top surface required no specimen preparation, the cross-section was prepared by cutting a smaller section off the substrate with a high-speed diamond blade saw, mounting it in cross-section in a conductive Bake-lite mount, and then polishing the sample down to 1200 grit SiC with a final 0.05 μm silica polish. After each polishing step, the samples were cleaned in an ultrasonic cleaner with acetone, followed by isopropanol and water rinse, and dried under pressurized air flow.

The phase identification of the samples was determined using X-Ray Diffraction (XRD) using a Philips MPD operated at 45 kV and 35 mA with a Cu $k_{\alpha 1}$ as the radiation source (1.541Å).

The work function of each sample was measured using Ultraviolet Photoelectron Spectroscopy (UPS) from sectioned 10 mm x 10 mm x 1 mm plates taken from the original deposit substrate and coating. The UPS chamber was evacuated to a base pressure of 10^{-8} Pa

whereon the samples were pre-heated to 1000 °C (measured by a pyrometer) using an e-beam heating stage to evaporate any residual surface oxides or binder material. After which a helium photon lamp source (21.2 eV) scanned the surface up to a kinetic energy level of 30 eV. The value for the work function, Φ , was calculated from the difference in Fermi energy level, E_F , and onset of secondary emission, E_{SE} , with the photon energy of the lamp source, E_L , removed using:

$$\Phi = E_L - (E_{SE} - E_F) \quad (\text{Eq. 6.1})$$

6.4 - RESULTS AND DISCUSSION

The LaB₆ powder and its post-sprayed coating upon initial inspection had the distinctive purple/violet hue that is commonly observed for this boride [4]. Qualitatively, both the pre-sprayed powder and post-sprayed coatings darkened towards an auburn hue with the addition of the boron. Figure 6.1 is the XRD results from the mixed agglomerated powder which included the LaB₆, the PVB binder, and the added elemental boron. The XRD peaks all indexed to the cubic LaB₆ phase (PDF#: 00-034-0427) with the PVB and boron powders' reflections being absent from the scan. The lack of PVB or boron reflections is contributed to their amorphous-based structure. From the micrographs of the powders in Figure 6.1, it can be seen that the sieving and mechanical mixing were effective, with a relatively even dispersion of the powder sizes that were less than 30 μm. The tabulation of the powder sizes, estimated from these micrographs, is found in Table 6.1. With the phase and starting powder morphology confirmed, the various LaB₆ mixtures were then deposited.

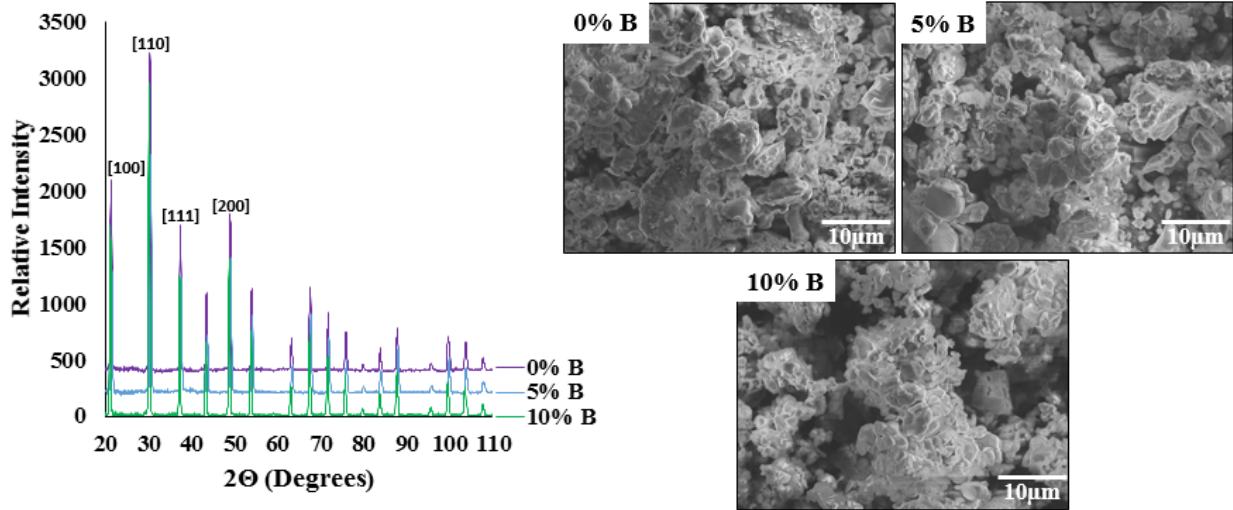


Figure 6.1 - XRD scans and SEM micrographs of the mixed powers prior to VPS. Only the first four strongest cubic reflections are labeled.

Table 6.1. Particle size distribution of the powder mixtures prior to vacuum plasma spraying.

VPS - Powder	Mean Particle Size (µm)	Standard of Deviation (µm)
0 Vol.% Added B	2.39	1.88
5 Vol.% Added B	2.41	1.71
10 Vol.% Added B	2.22	1.42

In the post-sprayed XRD scans, Figure 6.2, all three coatings could be indexed as the cubic structure of the initial powders. If boron had been lost in the deposited coating, this would have facilitated the precipitation of LaB_4 , which was not observed. If the excess boron was captured in the powder upon deposition, it would have resulted in potential multiple phase mixtures of LaB_6 , LaB_9 , and βB . These latter phases again were not indexed in the XRD scan. We also note that LaB_9 exhibits a blue (not purple) hue [26], which was not qualitatively observed in the coating's color. Collectively, this indicates that the LaB_6 powders retained the same phase under the spray, even in the case with no excess boron added.

At higher 2Θ reflections (where peak shifts are more readily observed and less sensitive to diffraction alignment corrections [27]), the peak positions were compared to each other and no significant peak shifts were observed. This too indicates that the excess boron did not play a substantial role in retaining the targeted compositions or effect the final composition between each of the coatings. This lack of peak shifts with stoichiometry is attributed to LaB_6 having a near line compound composition. Finally the added boron was not indexed in the XRD scan for the post-sprayed coatings. This either confirms that it deposited as an amorphous phase within the coating or was lost during the spray.

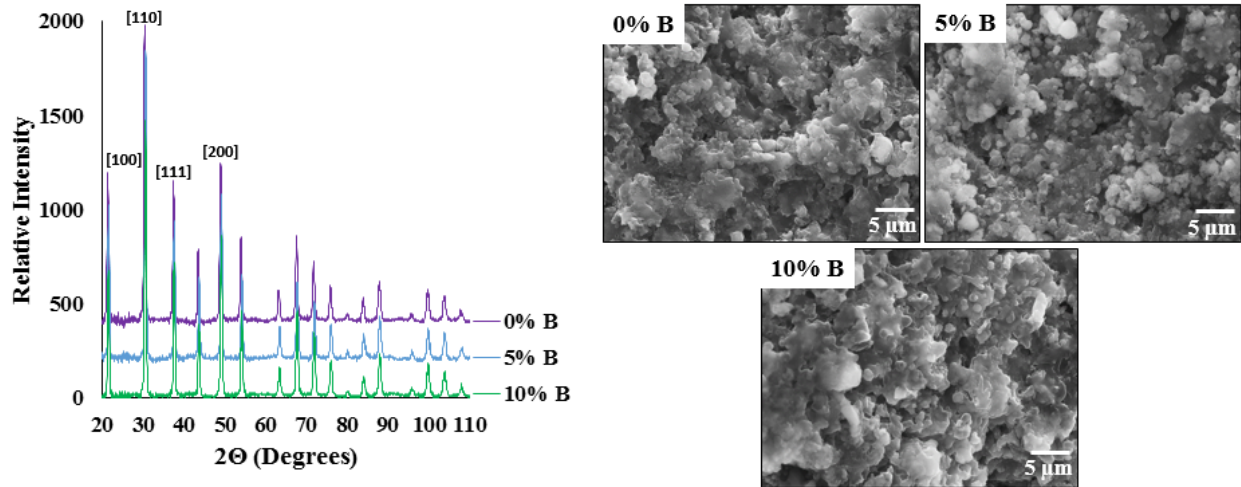


Figure 6.2 - X-Ray Diffraction scans and SEM micrographs of the VPS coatings after spraying.

From the micrographs of Figure 6.2, the surface of the coatings were found to have a granular morphology. The size of the grains/particles on the surface of the coating were similar between each deposit, Table 6.2; however the average size of these surface particles were noticeably smaller than that of the initial powders tabulated in Table 6.1. Proper melting of the particles would have led to a less granular and more splat-like morphology. Clearly, these spray parameters were unable to achieve the necessary thermal energy to the deposit. Adjustments in either a higher plasma arc energy, longer standoff distance to allow for more in flight heating

time of the powders, and/or a slower raster speed could help mitigate the granular type surface morphology. Though one should note that such changes may require a different substrate than stainless steel used here that would be capable of a higher temperature exposure, such as graphite or alumina.

Table 6.2. Particle size distribution of all the as-deposited coatings.

VPS - Coating	Mean Particle Size (μm)	Standard of Deviation (μm)
0 Vol.% Added B	0.79	0.63
5 Vol.% Added B	0.59	0.40
10 Vol.% Added B	0.93	0.71

After the first few initial passes, where the LaB_6 for all mixtures was able to adhere to the substrate, subsequent passes proved to be difficult in building up the coating. This is suggestive that under these VPS processing conditions, the thermal and geometric spray settings require further development if the material is to be built up into a larger more monolithic structure [28]. It is interestingly to note that the subsequent passes would expose the deposited material to additional thermal treatments, but, as evident in the top-down view of the deposit in Figure 6.2, the coating retained a granular morphology and these latter passes likely had little to no effect in further sintering of the granular surface.

Figure 6.3 are representative cross-sectional micrographs of the deposits where striking differences were observed. For the 0 vol.% sample, the coating is very granular and discontinuous. This is in agreement with the topology noted in Figure 6.2 for the same coating. However, for the boron added samples, a more dense coating, particularly for the 5 and 10 vol.% boron additions, can be observed. These cross sections also revealed a microstructure more

consistent with a splat-like morphology with evident layering, albeit very thin and discontinuous. These discontinuous features also trended with a fairly porous coating that is not typical of VPS microstructures but those more akin to the layered structures formed from air or low pressure plasma spray.

Though the top surfaces of all three samples revealed a granular morphology, the cross-sections did indicate that the addition of boron does facilitate a degree of densification of the coating. All three powders were mixed with a low melting temperature and low evaporation temperature PVB binder, which was not annealed prior to flow into the chamber. Consequently, this binder would disassociate into carbon, oxygen, and hydrogen based compounds such as water and carbon dioxide [29] in the high temperature plasma based vacuum environment. The presence of such species could then react with the depositing particles changing the surface chemistry and adhesion properties. In contrast, when excess boron was added, it could readily react with the dissociated PVB binder compounds. In doing so, these deleterious species effects are mitigated from reacting with the lanthanum boride particles, or at least to a lesser extent, and the deposited material is able to become more cohesive between the particulates as evident in the micrographs of Figure 6.3. This would be analogous to a protective shield gas used to prevent oxidation and embrittlement of weld joints [30]. Previous reports in particle suspensions have shown that there is a strong reaction between PVB binders and free boron, which may help explain this behavior[31]. From the prior XRD findings in Figure 6.2, the excess boron was not necessary to retain the phase of the deposit leaving it free to react with other potential species during deposition.

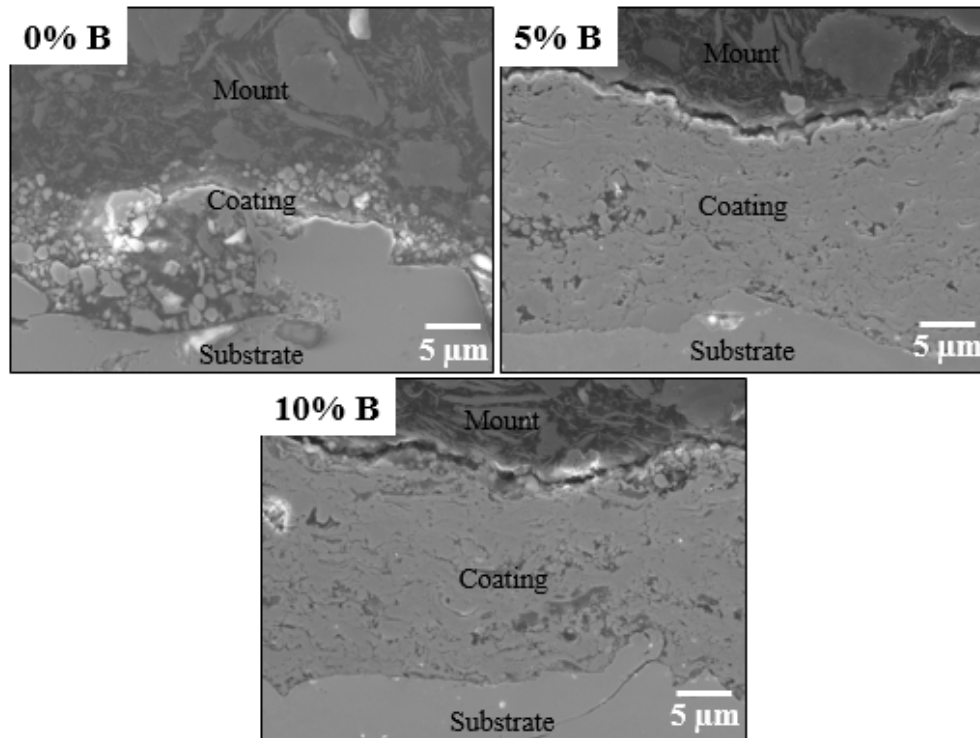


Figure 6.3 - Cross-sectional SEM imagery of each VPS coating, comparing their thickness and morphology. Note that in each image the phenolic mounting powder, the coating, and the stainless steel can be seen and have been labeled.

Figure 6.4 is a plot of the UPS spectrums with the calculated work function for each tabulated in Table 6.3. As one could expect, the values are similar since all three coatings were found to have the same LaB_6 phase. However, a small reduction of the work function is noted for the 5 vol.% and 10 vol.% B coatings. As noted above, these coatings were also found to be denser which was discussed in terms of the reacting with potential deleterious species during deposition. This could have resulted in a slightly more ideal deposition composition which would reduce the work function. Unfortunately all of the work functions are approximately twice as large as other reports for LaB_6 [7], [13], [32]. Previous reports have confirmed that impurities within the LaB_6 will increase the work function [11], [33]. Though VPS was able to produce a coating, it appears from the work function findings, the material is still plagued by contaminated

within the material itself. This increase in work function would require higher set temperatures necessary to achieve high thermionic emission.

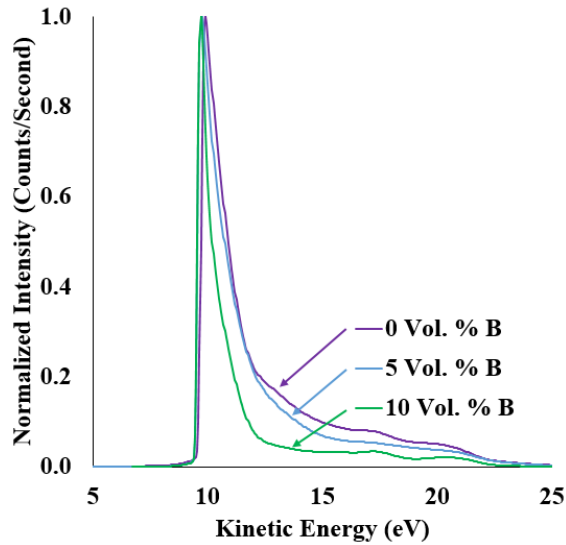


Figure 6.4 - UPS scans of each VPS coating, comparing their ability to emit electrons

Table 6.3 - Values for the work function of each coating as measured using UPS

Coating	Work Function (Φ)
0 Vol.% Added B	4.35 eV
5 Vol.% Added B	4.20 eV
10 Vol.% Added B	4.20 eV

6.5 - CONCLUSIONS

In this work we have successfully vacuum plasma sprayed LaB_6 with premixed 0%, 5%, and 10% boron additions with the LaB_6 powders as a coating onto a stainless steel substrate. After the initial deposition subsequent building of the coating was found to be difficult which suggested poor adhesion of the spray deposit on itself under the processing parameters used. In all three coatings, only the cubic LaB_6 phase was found indicating that the excess boron does not appear to influence the final stoichiometry and phase content. However, the boron was found to help in the densification of the coating. The excess boron is suspected to react with the PVB

binder used to prevent agglomeration of the powder during the spraying process. In doing so, the boron is able to reduce deleterious reactions of the binder species – including carbon, oxygen, and hydrogen – with the LaB₆ powder thereby potentially promoting better cohesive formations of the coating powders during deposition. The work function was also shown to slightly decrease, but is within the uncertainty of the measurement, with the increase of boron starting powder mixtures. However, the work functions are still approximately twice as high (~4.2 eV) as compared to high purity LaB₆ suggesting that impurity incorporation is still problematic in this form of processing of this material.

AUTHORS AND ACKNOWLEDGEMENTS

Thomas S. Burton¹, Daniel Butts², Tyson Back³, Steven Fairchild³, Gregory B. Thompson^{1#}

1) Department of Metallurgical and Materials Engineering, University of Alabama, Tuscaloosa, AL, USA.

2) Plasma Processing LLC; Huntsville, AL USA

3) Materials and Manufacturing Directorate, Air Force Research Laboratory, Dayton, OH, USA.

#Contact author: gthompson@eng.ua.edu

The authors gratefully acknowledge the funding of their research through grant FA9550-11-10160 by the AFOSR.

6.6 - REFERENCES

- [1] J. Zaat, “A quarter of a century of plasma spraying,” *Annual Review of Materials Science*, vol. 13, no. 1, pp. 9–42, 1983.
- [2] H. Greuner *et al.*, “Vacuum plasma-sprayed tungsten on EUROFER and 316L: Results of characterisation and thermal loading tests,” *Fusion Engineering and Design*, vol. 75, pp. 333–338, 2005.
- [3] R. A. Morris, B. Wang, D. Butts, and G. B. Thompson, “Variations in tantalum carbide microstructures with changing carbon content,” *International Journal of Applied Ceramic Technology*, vol. 10, no. 3, pp. 540–551, 2013.

- [4] T. Lundstrom, "Structure, defects and properties of some refractory borides," *Pure and Applied Chemistry*, vol. 57, no. 10, pp. 1383–1390, 1985.
- [5] K. A. Schwetz, "Boron carbide, boron nitride, and metal borides," *Ullmann's Encyclopedia of Industrial Chemistry*, 1985.
- [6] A. Kartavykh, E. Asnis, N. Piskun, I. Statkevich, M. Gorshenkov, and V. Tcherdyntsev, "Lanthanum hexaboride as advanced structural refiner/getter in TiAl-based refractory intermetallics," *Journal of Alloys and Compounds*, vol. 588, pp. 122–126, 2014.
- [7] D. M. Goebel, R. M. Watkins, and K. K. Jameson, "LaB₆ hollow cathodes for ion and hall thrusters," *Journal of Propulsion and Power*, vol. 23, no. 3, pp. 552–558, 2007.
- [8] D. M. Goebel, J. Crow, and A. Forrester, "Lanthanum hexaboride hollow cathode for dense plasma production," *Review of Scientific Instruments*, vol. 49, no. 4, pp. 469–472, 1978.
- [9] D. Goebel, Y. Hirooka, and T. Sketchley, "Large-area lanthanum hexaboride electron emitter," *Review of Scientific Instruments*, vol. 56, no. 9, pp. 1717–1722, 1985.
- [10] D. Schechter and C. Tsai, "Indirectly heated cathodes and duoplasmatron type electron feeds for positive ion sources," Oak Ridge National Lab., TN (USA), 1981.
- [11] E. Storms and B. Mueller, "A study of surface stoichiometry and thermionic emission using LaB₆," *Journal of Applied Physics*, vol. 50, no. 5, pp. 3691–3698, 1979.
- [12] M. Mushiaki, K. Akaishi, T. Mori, Y. Kubota, Y. Funato, and O. Motojima, "LaB₆ coating to reduce the outgassing rate of a vacuum wall," *Materials Science and Engineering: A*, vol. 163, no. 2, pp. 177–179, 1993.
- [13] W. Waldhauser, C. Mitterer, J. Laimer, and H. Störi, "Sputtered thermionic hexaboride coatings," *Surface and Coatings Technology*, vol. 98, no. 1, pp. 1315–1323, 1998.
- [14] E. Galvanetto, F. Borgioli, T. Bacci, and G. Pradelli, "Wear behaviour of iron boride coatings produced by VPS technique on carbon steels," *Wear*, vol. 260, no. 7, pp. 825–831, 2006.
- [15] S. J. Harris, G. Krauss, S. Simko, R. Baird, S. Gebremariam, and G. Doll, "Abrasion and chemical–mechanical polishing between steel and a sputtered boron carbide coating," *Wear*, vol. 252, no. 1, pp. 161–169, 2002.
- [16] R. McPherson, "A review of microstructure and properties of plasma sprayed ceramic coatings," *Surface and Coatings Technology*, vol. 39, pp. 173–181, 1989.
- [17] S. Dallaire and B. Champagne, "Plasma spray synthesis of TiB₂-Fe coatings," *Thin Solid Films*, vol. 118, no. 4, pp. 477–483, 1984.

- [18] C. Martini, G. Palombarini, G. Poli, and D. Prandstraller, "Sliding and abrasive wear behaviour of boride coatings," *Wear*, vol. 256, no. 6, pp. 608–613, 2004.
- [19] S. Wayne and S. Sampath, "Structure/property relationships in sintered and thermally sprayed WC-Co," *Journal of Thermal Spray Technology*, vol. 1, no. 4, pp. 307–315, 1992.
- [20] S. Sampath and S. Wayne, "Microstructure and properties of plasma-sprayed Mo-Mo₂C composites," *Journal of Thermal Spray Technology*, vol. 3, no. 3, pp. 282–288, 1994.
- [21] N. Stoloff, "An overview of powder processing of silicides and their composites," *Materials Science and Engineering: A*, vol. 261, no. 1, pp. 169–180, 1999.
- [22] E. Galvanetto, F. Galliano, F. Borgioli, U. Bardi, and A. Lavacchi, "XRD and XPS study on reactive plasma sprayed titanium–titanium nitride coatings," *Thin Solid Films*, vol. 384, no. 2, pp. 223–229, 2001.
- [23] "Item Number: L-1128, Chemical Name: Lanthanum boride," in Materion Corporation, 2016. [Online]. Available: <https://materion.com/Businesses/AdvancedMaterialsGroup/About/Related/ItemDetail.aspx?item no=L-1128>. Accessed: Oct. 24, 2016.
- [24] "Elemental Amorphous Boron Powder," in SB Boron. [Online]. Available: http://www.sbboron.com/sb_95.html. Accessed: Oct. 24, 2016.
- [25] "Technical Data Sheet Butvar® B-72," in Eastman Chemical Company, 2014. [Online]. Available: http://ws.eastman.com/ProductCatalogApps/PageControllers/ProdDatasheet_PC.aspx?Product=71095423. Accessed: Oct. 27, 2016.
- [26] M. E. Schlesinger, P. Liao, and K. E. Spear, "The B-La (boron-lanthanum) system," *Journal of Phase Equilibria*, vol. 20, no. 1, pp. 73–78, 1999.
- [27] B. D. Cullity, *Elements of X-ray Diffraction*, 2nd ed. Addison-Wesley Publishing Company Inc., 2001.
- [28] R. C. J. Tucker, *ASM Handbook - Thermal Spray Technology*, vol. Volume 5A. ASM International, 2013.
- [29] T. Yang, W. Chang, and D. Viswanath, "Thermal degradation of poly (vinyl butyral) in alumina, mullite and silica composites," *Journal of Thermal Analysis and Calorimetry*, vol. 47, no. 3, pp. 697–713, 1996.
- [30] D. H. (Welding instructor) Phillips, *Welding Engineering: An Introduction*. Hoboken : John Wiley & Sons Inc., 2016., 2016.

- [31] C.-W. Cho, Y.-S. Cho, J.-G. Yeo, J. Kim, and U. Paik, "Effects of PVB on the gelation behavior of BaTiO₃-based dielectric particles and glass suspension," *Journal of the European Ceramic Society*, vol. 23, no. 13, pp. 2315–2322, 2003.
- [32] W. Waldhauser, C. Mitterer, J. Laimer, and H. Störi, "Structure and electron emission characteristics of sputtered lanthanum hexaboride films," *Surface and Coatings Technology*, vol. 74, pp. 890–896, 1995.
- [33] C. Oshima, E. Bannai, T. Tanaka, and S. Kawai, "Thermionic work function of LaB₆ single crystals and their surfaces," *Journal of Applied Physics*, vol. 48, no. 9, pp. 3925–3927, 1977.

CHAPTER 7

CONCLUSIONS AND FUTURE WORK

This dissertation has studied the effect of erosion for a series of different types of ceramic based materials and systems. The results of which revealed underlying erosion mechanisms through the examination of surface features found on an eroded ceramic chamber wall of a Hall effect thruster. The effect that such surface features would have on the secondary electron emission properties, a behavior which is critical to understand near-wall plasma sheath stability, was analyzed using systematically controlled features that mimicked similar morphologies and/or topologies to those found in the eroded surface. Lastly, LaB₆ as a vacuum plasma sprayed cathode coating was fabricated and characterized as a possible replacement for external pressed powder cathodes; the coatings were found to be sensitive to excess boron in its as-deposited densification. Overall, these results have garnered new insights into how material microstructures regulates material-plasma sheath interactions. The specific conclusions are given below.

7.1 - EXTENDED PLASMA EROSION OF A M26 HET CHAMBER WALL

A 60 wt% boron nitride (BN) - 40 wt% silica hot-pressed composite, denoted as M26, was used as the insulating chamber wall for a Xe plasma Hall effect thruster operated for approximately 2000 hours at power levels between 1.5-5 kW. The chamber wall showed a range of erosion microstructures. In the heavily eroded regions, striations in the surface topology were evident with surface protrusions in the generic shape of conical tips consisting of laminate BN and silica phases. Micro-cracking along the long axis of the BN basal plane was prevalent. Through a two-dimensional finite element model, the micro-cracking has been determined to

occur because of the anisotropic thermal expansion of BN in the amorphous silica matrix. Exfoliation accompanied the micro-cracking in BN and resulted in the preferential loss of BN as compared to silica in these heavily eroded regions. While thermal cycling was attempted in polished BN and M26 samples, additional testing with chamber wall samples of differing erosions would aid in understanding the magnitude of the thermal expansion problem. As well it would assist in understanding if this effect is enhanced by the other erosion processes. In addition, examining more plasma eroded surfaces to determine the similarities in their surface features would be advantageous to understanding plasma erosion as an overall process.

7.2 - INFLUENCE OF ROUGHNESS ON SEY FROM GRAPHITE SURFACE TOPOLOGIES

Based upon the varied surface topologies characterized in the plasma eroded surface, a case study material was mechanically attrition to simulate these features. The case material was graphite and was chosen because it has similar crystallography to BN but increased electrical conductivity which allowed a primary electron beam to be incident on the surface with no surface charging to impede electron emission. The smoothest surface (root mean square roughness $0.110 \pm 0.022 \mu\text{m}$) produced the highest SEY; however, a moderate rough surface ($0.990 \pm 0.019 \mu\text{m}$) had a lower yield than a rougher ($7.10 \pm 1.23 \mu\text{m}$) surface. This trend was also observed in the eroded chamber wall where the roughest surface did not result in the lowest SEY. This suggested a characteristic roughness length scale associated with emission which has been rationalized by differences between large and small scale variations in the roughness found on the surface. This length scale dependence was noted in the different erosion surface of a graphite coated M26 surface that was previously characterized.

Additional research using a greater range of sample roughness and with smaller step sizes between roughness levels would provide stronger validation of this characteristic length scale

and a more accurate picture of its specific dimensions. More chamber wall samples as well as comparisons against polished and roughened BN and M26 samples, roughened in the same manner as the graphite, would also further elucidate the accuracy of the comparisons. Additionally, comparing our results with those measured on higher sensitively tools and those with capable of pulsing the electron beam to skirt the issue of charging on resistive materials, would put our results in proper context.

7.3 - INFLUENCE OF MILLIMETER SCALE GROOVES ON PLASMA SHEATH COLLAPSE VOLTAGE

Prior research by others have also shown much coarser length scale topologies in extended eroded materials, like those of the saw tooth ridges seen in Figure 1.2. A series of grooved hexagonal BN disks with different groove aspect ratios, designed to mimic simplified versions of these erosion features, were then exposed to an argon plasma. The change in the plasma sheath characteristics, particularly the ‘collapse voltage’ which occurs when the discharge voltage is sufficient to produce enough secondary electrons to collapse the sheath, was 44% and 89% higher for a 1 mm and 5 mm grooved depth, respectively, as compared to a planar surface. A ray-trace optical model for secondary electron emission reduction with a one-dimensional kinetic model for the plasma was used to simulate the responses. With increased groove depth, this simple model was inadequate to capture the correct collapse voltage, which is attributed to a variation of electron and ion charge densities near the groove entrance. These results provide insights into how larger length scale surface topology features, on the order of the Debye length, influence the dynamic interactions between a surface and plasma sheath. Future work could be done with a greater range of groove dimensions to further explain the range of collapse voltage protection that is capable. Greater modelling efforts, either plasma or electron focused, would also improve the current descriptions of what exactly is occurring. In addition,

other material systems of interest can be used to compare if they differing levels of electron capture that is occurring as a result of the grooving.

7.4 - CHARACTERIZATION OF VACUUM PLASMA SPRAYED LaB_6 COATINGS

Finally, the dissertation research focused on the fabrication of lanthanum hexaboride (LaB_6) as a coating via vacuum plasma spraying (VPS). LaB_6 is a widely used electron cathode material because of its excellent thermionic emission properties, creating a high flux of electrons at high temperatures. The processing of a LaB_6 coating through the use of VPS, which could enable the use of this thermionic material over more complex shapes and geometries. The LaB_6 starting powders were mixed with either 0, 5, or 10 vol.% amorphous boron additions and it was found that the cubic LaB_6 phase was present in all post-sprayed conditions with all deposits revealing the classical ‘splat’ microstructure. However, the densification of the coating was significantly enhanced with the 5 and 10 vol.% B additions, with these coatings having a work function of 4.20 eV, which was slightly lower than the other coatings. Though LaB_6 was successfully coated, the work function was still approximately twice as large as other LaB_6 powder processing routes suggesting that impurity contamination is prevalent during the VPS process. Additional work is needed to continue refining the exact processing potential of this coating system, specifically refinement of the geometric and thermal constraints of the substrate. Using a graphite substrate and a higher arc energy have the potential to greatly improve the self-adhesion of the coating. To potentially reduce the surface contamination, it is suggested to reduce the powder mixture prior to spraying as it will greatly reduce the presence of the binder

APPENDIX

A series of other experiments were conducted through the course of the research. However, the results of these experiments were either inconclusive or unable to be incorporated into the research given. This data is included here for completeness of the study and a data base for any future studies.

A.1 - THERMAL CYCLING OF BORON NITRIDE AND M26

In Chapter 3, micro-cracking was noted and contributed to anisotropic thermal expansion in a composite microstructure. To further those studies, a series of M26 and BN samples were thermally cycled to determine the number density and crack length as a function temperature and cycles. The aim of which was to provide a data base for future cracking prorogation modeling. Samples examining the thermal cycling behavior of the microstructures in BN and M26 were developed in response to the preliminary results.

Four samples were prepared to test the variables: material type and thermal cycles. Each sample - BN and M26 - was sectioned into ~ 10 x 10 x 5 mm blocks and polished down to 0.05 μm silica solution finish. The samples were then coated with 20-30 nm of graphitic carbon to allow the surface to be sufficiently conductive for electron imaging. Each sample was inserted into a tube furnace which is preheated to 500 °C. This is approximately two-thirds of the peak operational temperature of a HET discharge channel wall [4]. The set of samples were heated for one hour increments and allowed to cool to room temperature for fifteen minutes in-between. This was repeated one, three, and seven times. After each cycle, the samples were re-coated with the graphite and imaged for the number density and length of cracks formed. Imaging of the samples was done in the SEM using back-scattered electron (BSE) mode at 10 keV to ensure that

the surface level cracks are visible with the highest amount of detail and not obscured by surface irregularities, which can occur in secondary electron imaging mode. Ten images were taken near the midpoint of each sectioned sample to avoid edge effects. The cracks were manually traced using a Nikon Elements software package, shown in Figure A.1, and approximately 500 cracks were found over approximately 140 images collected.

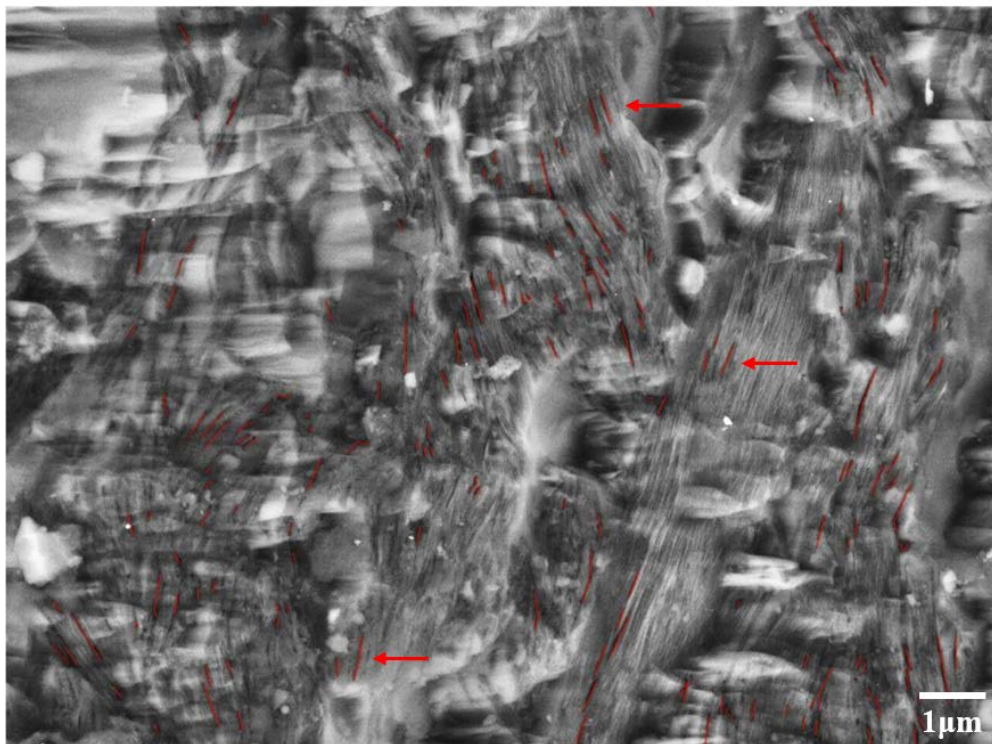


Figure A.1 - Back Scattered Electron micrograph with the red traced lines of measured cracks generated from thermal cycling. Arrows have been added to indicate locations of traced lines.

The histograms for the repeated one-hour thermal cycling experiments are shown in Figure A.2. The starting cracks are those formed either during the machining of the samples, from the vendor source, or polishing prior to heating and this provides a control for the material. For the pure BN sample, one thermal cycle increased the number of cracks but the general distribution of crack lengths remains centered on 0.7 μm. Upon further cycling, the mean crack length increases, with several cracks detected with length longer than 3 microns. This suggests that nucleation of cracks occurs during the first thermal cycle, then these cracks tend to grow

upon further cycling as the total crack length increases. This suggests that crack nucleation, rather than growth, appears dominant in the initial cycle, then it switches to growth once all feasible cracks have nucleated. However the behavior in M26 is very different, with a high starting number of cracks that slowly grow in length. The behavior of the 7 cycles data for M26 however appears totally different as is likely an anomaly.

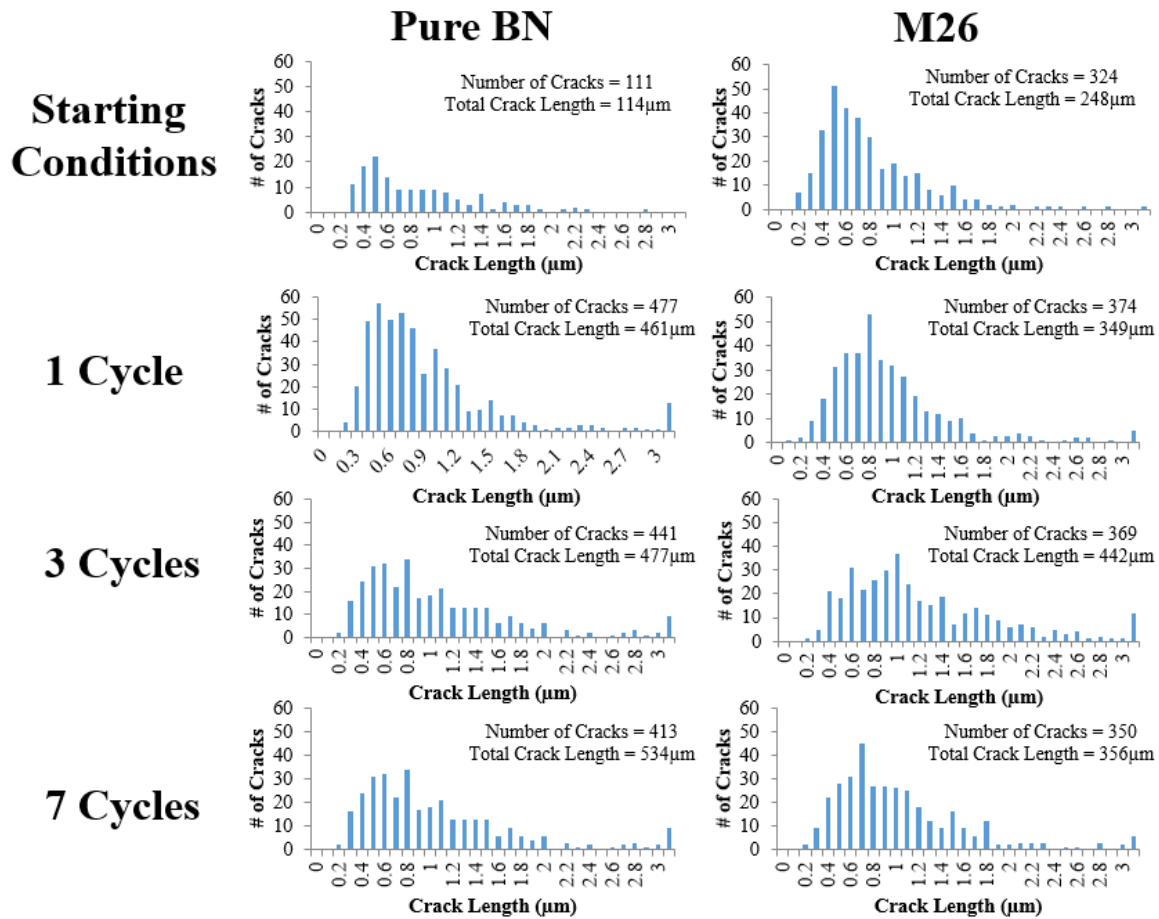


Figure A.2 - Histograms of crack number and length as a function of thermal cycles at 500 °C for one hour.

Given extended time, for one crack, more micro-cracking was observed for the same length evident by the raise in the number of cracks. This behavior is linked to the type of microstructure as in M26 the rigid silica grains confine the BN phase. Hence upon initial heating and cooling, the BN’s anisotropic thermal expansion results in micro-cracking as the grain

attempts to accommodate itself with the silica matrix. Once these cracks have formed within the BN grain, they grow as these grains have already achieved a critical number of cracks within it. In contrast, it appears that the BN microstructure, without the rigid boundaries of another phase does not provide sufficient confinement to cause the BN to nucleate a new crack in response to the thermal stresses. Rather, the pre-existing cracks grow. This may suggest that BN, rather than M26, would erode at a slower rate in a plasma due to the absence of rigid phase boundaries where the BN exfoliates from the microstructure.

A.2 - MATLAB PROGRAM FOR PARTITIONING OF OPTICAL PROFILOMETRY DATA

In Chapter 4, the optical profilometry data was partitioned into increasingly smaller individual regions. This was done to test the hypothesis that the surface roughness was converging to a characteristic length scale. This is the MATLAB code that was used to separate an array of data [A], with dimensions of 640x480, into equally sized “bins”. The value for the RMS roughness, also known as the standard of deviation, was then calculated for each new bin and the process repeated till the smallest equally sized bin was reached.

```
clc
clear all
A=[];
no_rows=640; %% total no. of rows in matrix
no_column=480; %% total no. of columns in matrix
count_Arow=1; %% counter for storing A as a column matrix A_row
for i=1:no_rows
    for j=1:no_column
        A_row(count_Arow)=A(i,j);
        count_Arow=count_Arow+1;
    end
end

block_row=40; %% enter row(m) for mxn partition
block_column=30; %% enter column(n) for mxn partition
check=0;
```

```

v=0; % total no. of partitions counter

check1=no_rows/block_row; %% checks if row partition entered is valid
check2=no_column/block_column; %% checks if column partition entered is valid
if(((rem(no_rows,block_row))==0)&&((rem(no_column,block_column))==0))
    check=1;
end

if(check==1) % enter loop if partition entered is valid
    k=0;
    while (k<=(no_rows*no_column)) %% checks if we reached the end of the matrix entered
        l=k;
        for i=1:block_column
            Anew(1,i)=A_row(l+i); %% 1st row of each partition extract
        end
        for m=2:block_row
            for n=1:block_column
                Anew(m,n)=A_row(l+n+no_column); %% other rows of partition
            end
            l=l+no_column;
        end
        v=v+1;
        Anew;
        counter=1;
        for alpha=1:block_row
            for beta=1:block_column
                Arand(counter)=Anew(alpha,beta); %% creates a column matrix for each partition
                counter=counter+1;
            end
        end
        std_dev(v,1)=std(Arand); %% calculates standard deviation between elements of each
partition
        k=k+block_column;
        if(rem(k,no_column)==0)
            k=l+block_column;
        end
    end
end
end

```